RICE UNIVERSITY

Paramagnetic particle assemblies as colloidal models for atomic and molecular systems

by

Dichuan Li

A THESIS SUBMITTED
IN PARTIAL FULFILLMENT OF THE
REQUIREMENTS FOR THE DEGREE

Doctor of Philosophy

APPROVED, PROPOSAL COMMITTEE:

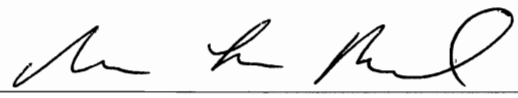

Sibani Lisa Biswal, Assistant Professor
Chemical and Biomolecular Engineering

Matteo Pasquali, Professor
Chemical and Biomolecular Engineering
and Chemistry

Walter G. Chapman, William W. Akers
Professor, Chemical and Biomolecular
Engineering

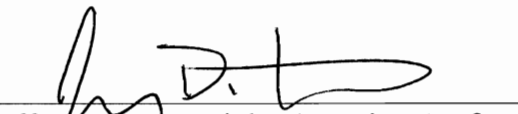

Jeffery D. Hartgerink , Associate Professor
Chemistry and Bioengineering

HOUSTON, TEXAS
MAY 2011

Abstract

Paramagnetic particle assemblies as colloidal models for atomic and molecular system

by

Dichuan Li

Colloidal particles are ideal models for studying the behavior of atomic and molecular systems. They resemble their atomic and molecular analogues in that their dynamics are driven by thermal energy and their equilibrium properties are controlled by inter-particle interactions. Based on this analogy, it is reasonable to construct colloidal chains, where each particle represents a repeat unit, as models for polymers. The advantages of this system over molecular systems are its controllable rigidity, contour length and diameter, as well as the convenience to capture its instantaneous shape and position via video microscopy, which are not trivial to realize in molecular systems. By utilizing the dipolar properties of magnetic colloids, a number of groups have assembled semiflexible and rigid colloidal chains by cross-linking magnetic beads under a magnetic field using polymer linkers. Recently, efforts in constructing colloidal chains led even to anisotropic magnetic colloidal chains that mimic the detailed atomic arrangements of polymers These properties make colloidal chains possible candidates for the classic bead-spring or bead-rod model systems for semiflexible and rigid polymers.

In my thesis, I present a method for generating linear colloidal chain structures by linking surface functionalized paramagnetic particles using DNA. First, I investigate the force interactions between individual magnetic particles under different conditions to

optimize the resulting chain stability. A systematic study the bending and rotational diffusion dynamics of the chains and their relationship with the DNA linking chemistry is presented. I then demonstrate their use as a ideal model system to study polymer dynamics. In addition, a technique to measure short-range repulsive surface forces between these colloids with high precision was developed. Building on these repulsive force studies, a colloidal system to study 2-D phase transitions was created. This thesis provides insights into understanding and engineering the directed-assembly of magnetic colloids with specific surface interactions, as well as using the assemblies as model systems to study molecular level phenomena.

Acknowledgments

First and foremost, I thank my thesis advisor Dr. Sibani Lisa Biswal, for her guidance, support and trust, without which this thesis would not be accomplished. I am one of Dr. Biswal's first students at Rice, and I was fortunate to have a lot of her attention and be taught by her hands-on. Most importantly, she led me by example on how to be a good writer and presenter, a creative, rigorous and responsible researcher.

My thesis committee members have given me support and scientific insights. I thank Professor Matteo Pasquali for his guidance on most of my physics-related projects. The depth and breadth of his knowledge in physics have always been and will continue to be an inspiration for my own research. I thank Professor Walter Chapman, from whom I learned molecular simulation, for his useful suggestions to my projects and encouraging my collaboration with his students. I thank Professor Jeffrey Hartgerink for being on my thesis committee and contributing valuable questions.

I gratefully thank my host family, Bong and Charles Sternling. They were the first people to have me when I first came to Houston. Chuck had been a research engineer with Shell for over 40 years and our after-dinner discussions were full of physics and engineering and full of fun. Bong and Chuck made me feel at home in a foreign country and taught me how to be a good and fun person.

I thank Professor George Hirasaki for teaching me fluid mechanics in ChBE 501 class and during our windsurfing sessions. We share the same passion for surfing and skiing, and fluid mechanics was made fun in those contexts and less intimidating when I work on it in my research. I thank Professor Nicholas Mantzaris for teaching a challenging

Numerical analysis course, which helped me build a solid foundation for the computational works in my PhD research.

I thank all Biswal group members for their kindness, especially Weijia Xie, Gautam Kini, Julie Byrom and Kun Ma for our collaborations. They made the office and lab exciting places to be.

I thank Natnael Behabtu and Nikta Fakhri for their genuine and infectious passion for fundamental science that stimulated my desire to probe deeper into my own research projects. Our conversations in Classic paper club and SMASH (Soft Matter Academic Social Hour) continue to inspire me.

I thank the researchers who collaborated with me or offered me insights in my PhD research projects. They are Dmytro Nykypanchuk from Brookhaven National Labs, Randall Erb previously from Duke University, Professor Andrej Vilfan from Stefan Institute, Ryan Larsen previously from Harvard University, and Jie Yu, Zhengzheng Feng, Ruiqiang Sun, Mariam Nouri, Kai Gong, Amir Amini, Di Du, Daniel J. Stark and Professor Clarence Miller from Rice.

I thank all the graduate students in Chemical and Biomolecular Engineering department at Rice for their support when I was the president of the department Graduate Student Association. They are all nice people and I cared about them.

Last but not the least; I thank my dear parents, Mr. Ning Li and Mrs Daili He, for their unconditional love and support, without which I could not be what I am now and this thesis would not be possible.

Contents

List of Figures

Chapter 1

Introduction

1.1. Self-assembled colloidal systems

Colloids play a role in many aspects of our everyday life and people have found ways to utilize their unique properties to develop new and enhanced functionalities in a wide array of applications such as ceramics, detergency and biomedical applications[1, 2]. Colloids are complex fluids, in which nano- and micron sized objects are suspended in a low molecular weight liquid. At these characteristic length scales, colloidal structures have the potential to self-organize into three dimensional structures with various degrees of orders[3-5]. These structures form the building blocks for functional materials that possess unique physical properties[6-8] (e.g. photonic colloidal crystals).

In addition to their application to form materials for everyday-life, scientists also use colloids as models for atomic systems; for example, physicists have been able to study statistical thermodynamics using a system of micron-sized colloidal spheres. The rationale behind this is that, despite the ~$O(10^3)$ difference in length scale, colloidal

dynamics is also driven by thermal energy (k_BT) as well as long-range and short-range interactions among the particles, as in atomic systems. The advantages of colloidal systems over atomic systems are 1) micron sized colloids can be directly monitored using optical microscopy[9], thus one obtains important information such as position, velocity and orientation, within the field of view in the system, even in three dimensions[10] (confocal microscopy); 2) interactions between colloids can be finely tuned by surface functionalization[11-13], solvent,[14] or external fields[15]. These advantages enable researchers to probe into the behavior and dynamics of individual "atoms" with high precision, and thus uncover new physics that is otherwise not observable for real atomic systems. Examples of this include using colloidal spheres to mimic metallic crystals to study melting[16, 17] or using binary colloids to resemble ionic crystals[18].

To better resemble the more complex structures of naturally occurring systems, researchers have started building anisotropic colloidal particles using self-assembly technology. Self-assembled colloids are sometimes referred to as "colloidal molecules"[19] due to similarity of their structures with that of molecules. They have more complex interactions and lead to more complex phase behavior[20] than spherical colloid systems. Up to date, a variety of self-assembled colloidal structures, including dimers, tetramers, stars, diamonds, and other examples shown in Figure 1.1, have been synthesized by various research groups[21]. These anisotropic colloids serve as building blocks for the construction of macroscopic material with unique properties[22]. In addition, they enable colloidal scientists to develop new model systems for anisotropic molecules[20].

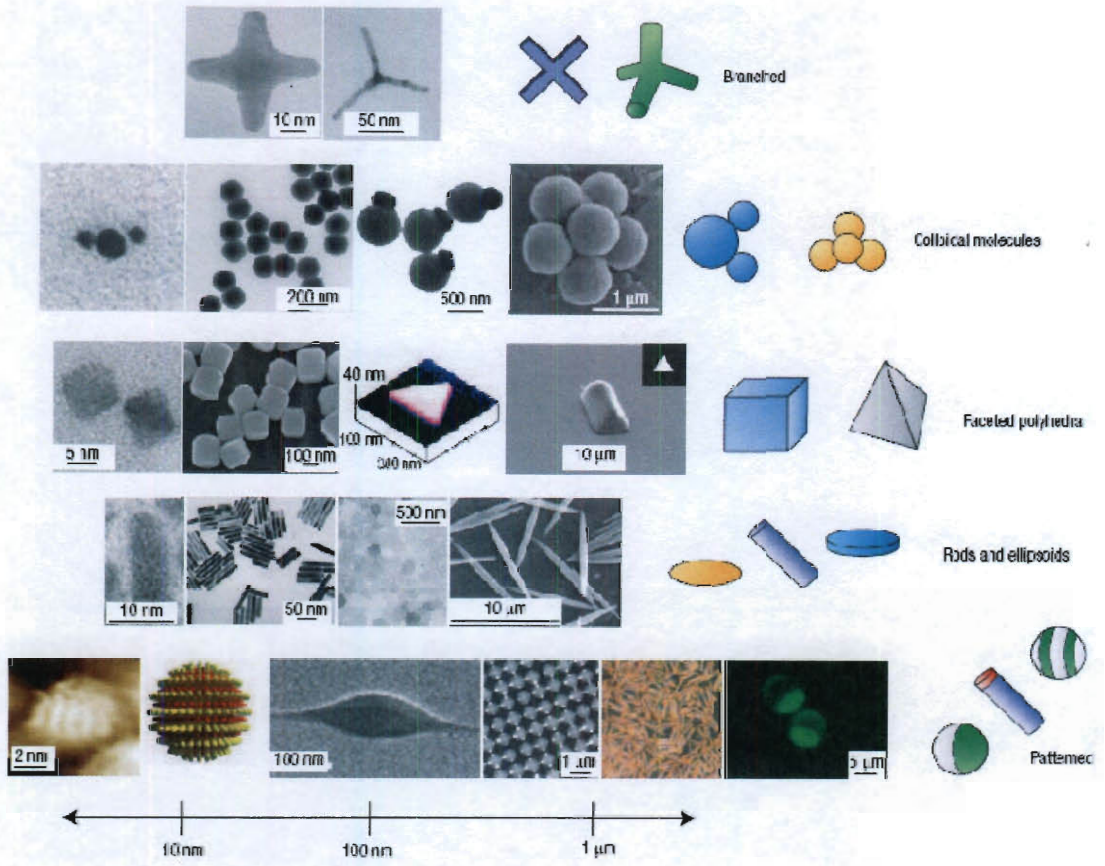

Figure 1.1. (Images adapted from reference 13) Representative examples of recently synthesized anisotropic particle building blocks. The particles are classified in rows by anisotropy type and increase in size from left to right according to the approximate scale at the bottom. From left to right, top to bottom: branched particles include gold and CdTe tetrapods. DNA-linked gold nanocrystals, silica dumb-bells, asymmetric dimers and fused clusters form colloidal molecules. PbSe and silver cubes as well as gold and polymer triangular prisms are examples of faceted particles. Rods and ellipsoids of composition CdSe, gold, gibbsite and polymer latex are shown. Examples of patterned particles include striped spheres, biphasic rods, patchy spheres with 'valence', Au–Pt nanorods and Janus spheres.

Another rational step to introduce anisotropy to the colloids is to assemble colloidal spheres into anisotropic structures (e.g. chains). To realize the symmetry breaking in this step, either the spherical building blocks are required to have intrinsic anisotropy in the inter-particle interactions[23, 24] (e.g. Janus particles) or their response to external field[25, 26] or confinement[27] is anisotropic. It has been known for decades that paramagnetic particles align into linear chain structures under the influence of a uniform magnetic field[28, 29]. Recently, it has been shown that these linear structures can be physically[26] or chemically[25, 30, 31] linked to form permanent chains (Figure 1.2). These chain structures resemble an important category of molecules is ubiquitous: polymers.

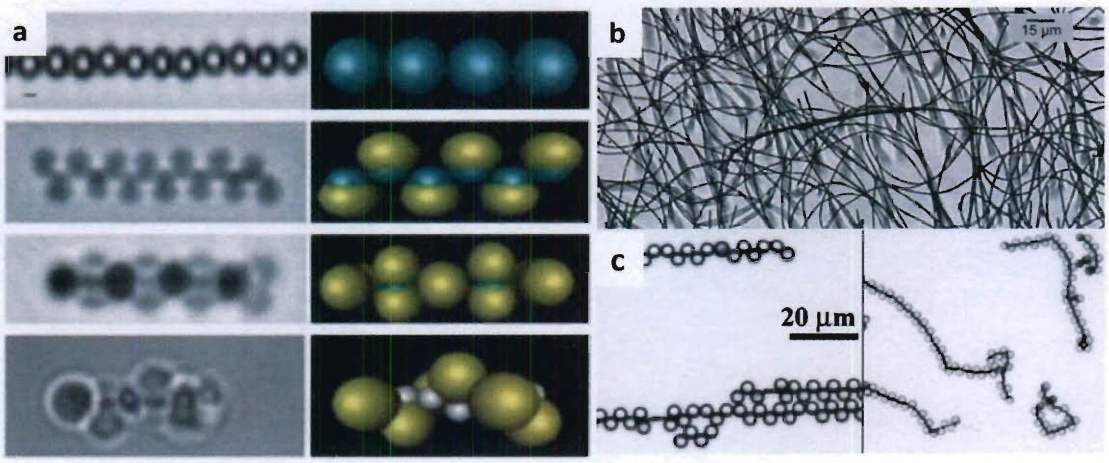

Figure 1.2. A set of microscope images showing the chain structures made by external magnetic field using paramagnetic colloids. (Images a and c from reference 15, image b from reference 26)

Magnetic field directed assembly of paramagnetic particles provides a promising route towards synthesizing "colloidal polymers" for both studies of individual polymer

dynamics[30, 32], polymer phase behavior and other applications[33]. Important physical properties of the resulting chains, such as length and rigidity, are controlled by the inter-particle interactions and particle surface functionalization, which are not systematically studied. In this thesis, I investigate the interactions between paramagnetic colloidal particles as a function of their surface functionalization and external field, and their effects on the properties of the resulting chains.

1.2. Paramagnetic particles

Paramagnetic colloidal particles are typically latex colloids containing randomly oriented ferromagnetic nanoparticles, which have permanent magnetic moments embedded within a polymer matrix. In the field "off" state, the particles are dispersed and randomly distributed due to Brownian motion. When a magnetic field is applied, induced dipoles interact (Figure 1.3) causing the particles to aggregate to form chains aligned in the field direction[34] with an attractive energy of

$$U_{mag} = \frac{4\pi a^6 \mu_0 \chi^2 {H_0}^2}{9r^3} \tag{1.1}$$

where a is the radius of the particles, μ_0 is the permeability of vacuum, χ is the magnetic susceptibility of each particle, H_0 is the external magnetic field strength and r the center-to-center particle distance. Equation 1.1 is true only when two dipoles are aligned in

parallel, otherwise the angle between dipoles must be considered. The size of these particles is in the colloidal range, between 100 and 3000 nm.

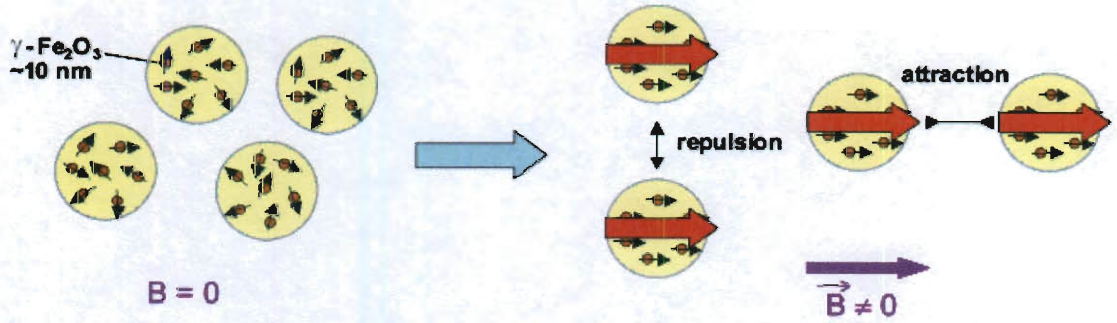

Figure 1.3. Polarization of paramagnetic particles in the absence and in the presence of the external magnetic field. In the absence of the field, the particles in a MR fluid are randomly distributed due to Brownian motion. In the presence of the field, the induced dipoles interact causing the particles to aggregate forming chains aligned in the field direction.[35]

In the absence of an external magnetic field, these fluids have an apparent viscosity of 0.1 to 1 $Pa \cdot s$ at low shear rates[34]. When a magnetic field is applied, high aspect ratio chain structures are formed causing the apparent viscosity of the solution to change significantly (up to six orders of magnitude) within a few milliseconds (Figure 1.4). This process is completely reversible when the magnetic field is removed[34].

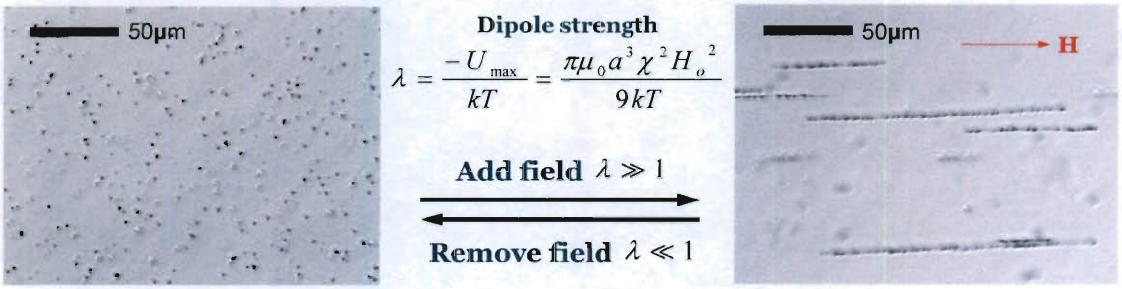

Figure 1.4. Dispersion of $1\mu m$ diameter paramagnetic colloidal particles in the absence and presence of an external magnetic field.

These chains are not permanent due to the reversibility of aggregation mentioned above and these structures need and external field to exist. This is due to the repulsive interactions (electrostatic and/or steric) between the paramagnetic colloidal particles. In order to mimic the dynamic behavior of biological filaments[36] and polymer molecules, as well as for some other potential applications such as micro-mixing[33, 37], a feasible way to maintain the structure in the absence of the external field is essential.

1.3. Linked colloidal chains

In recent publications, many secondary colloidal structures are maintained by weak attractive forces[38, 39] such as depletion and van der Waals forces. Therefore, the resulting structures do not have enough energy (usually a few k_BT's) to withstand large fluctuations, thus are not stable. A convenient method to hold the structure is to "glue" the elements by chemical bonds. Recently, Biswal[40] used biotin-PEG-biotin linker molecules to bond the streptavidin-coated paramagnetic particles and the resulting chains show elastic behavior in the absence of external magnetic field. Crocker et al[41] used

complementary ssDNA (single strand DNA) to bond polystyrene particles to maintain lattice structures. Bibette and coworkers used polyacrylic acid[42] (PAA) and double-stranded DNA[43] to link paramagnetic particles to form semiflexible long particle chains (up to $200\mu m$ in length). The DNA linking chemistry with its large hybridization energy (usually hundreds of k_BT's), provides a promising route toward stable linked particle chain structures.

While these methods have proved versatile, they often leave the mechanism of assembly obscure. Crocker et al[41, 44-46] studied the thermodynamic properties of the DNA-mediated colloidal aggregates such as phase behavior and DNA melting, but did not probe the mechanical properties of these aggregates such as the shear or tensile modulus to measure the strength of the bonding. Biswal et al[33, 34, 37, 40] investigated the elasticity of the linked particle chains as a function of the length of the linker PEG molecules but did not go into details as to how the length and rigidity of the linker molecules affect the overall elasticity of the chain. Bibette and coworkers[26, 35, 42, 43, 47-50] carefully measured the elasticity of their linked flexible magnetic filaments but only created a model using the persistence length as the single parameter to describe the elasticity of the chains; however, it is unclear what the mechanism is in the linking region between the particles.

To engineer these colloidal structures with controlled length, rigidity and surface functionality, we need to acquire a more thorough picture of the physics governing the linking process, and the relationship between particle surface interactions and the properties of the resulting chains. We need to address these questions:

1. How does particle interaction affect the stability of the resulting chains and what is the

energetics of the linking process?

2. How do the properties of the linker molecules affect the rigidity of the resulting chains?

3. How to characterize the rigidity and other parameters of an individual chain?

4. How to resolve the dynamics and degrees of freedom of an individual chain?

The answers to these questions will provide key insights into the nature of the complex motion of these polymer-linked colloidal chains as well as other chemically bonded self-assembly colloidal structures. The goal is to make them more useful models for studies of the molecular systems they resemble.

1.4. Thesis outline

This thesis is arranged in the following order: Chapters 2 and 3 deal with engineering the stability and rigidity of DNA-linked magnetic particle chains; Chapter 4 presents a scientific study of rod-like molecule diffusion using these chains; Chapters 5 and 6 demonstrate novel techniques using magnetic particle dispersion to study repulsive surface forces and phase behavior in two dimensions; and Chapter 7 presents a range of valuable future work that can be pursued from the current research and will add to the many applications of these magnetic colloidal systems.

Particularly, in Chapter 2, I present a theoretical and experimental study of the stability of DNA-linked paramagnetic colloidal chains as a function of external magnetic field strength and particle surface grafted DNA length and density. A total inter-particle free energy potential model is developed to account for all major forces contributing to

chain stability and a phase diagram is obtained from experiments to yield optimized parameters for successful linking and building stable linked chains. In Chapter 3, a Fourier mode analysis is used to analyze the curvature fluctuations of these chains. I show that their persistence lengths can be finely tuned in the range of 5μm~50 mm by changing the particle surface DNA length from 850bp to 15 bases. This provides a convenient and consistent approach to engineer and characterize the rigidity of the DNA-linked particle chains. In Chapter 4, by imaging the motion of beads and small kinks along the backbone of chains of DNA-linked colloids, I produce a direct and systematic measurement of bending relaxation time scales and axial rotational diffusivity of chains both in bulk solution and near a wall. These results again prove that DNA-linked paramagnetic particles are an ideal model system for studying polymer dynamics. In Chapter 5, I present the use of video microscopy of magnetic colloidal particles to measure short range repulsive forces between surfaces with sub-nanometer distance resolution. In Chapter 6, a novel two-dimensional system is demonstrated to study two-dimensional phase transition using magnetic colloids using an AC magnetic field to induce tunable attractive pair potentials. Finally, in Chapter 7, I suggest several studies that would further the application of the system and techniques develped in this thesis.

1.5. Reference

1. Hatton, T. A., Applications of structured interfaces, nanoparticles, and fluids. *Current Opinion in Colloid & Interface Science* **2006,** 11, (4), 191-192.
2. Dinsmore, A. D.; Hsu, M. F.; Nikolaides, M. G.; Marquez, M.; Bausch, A. R.; Weitz, D. A., Colloidosomes: Selectively permeable capsules composed of colloidal particles. *Science* **2002,** 298, (5595), 1006-1009.
3. Cho, Y. S.; Yi, G. R.; Lim, J. M.; Kim, S. H.; Manoharan, V. N.; Pine, D. J.; Yang, S. M., Self-organization of bidisperse colloids in water droplets. *Journal of the American Chemical Society* **2005,** 127, (45), 15968-15975.
4. Lin, Y. S.; Tsai, C. P.; Huang, H. Y.; Kuo, C. T.; Hung, Y.; Huang, D. M.; Chen, Y. C.; Mou, C. Y., Well-ordered mesoporous silica nanoparticles as cell markers. *Chemistry of Materials* **2005,** 17, (18), 4570-4573.
5. Zoldesi, C. I.; Imhof, A., Synthesis of monodisperse colloidal spheres, capsules, and microballoons by emulsion templating. *Advanced Materials* **2005,** 17, (7), 924-+.
6. Jiang, P.; Bertone, J. F.; Hwang, K. S.; Colvin, V. L., Single-crystal colloidal multilayers of controlled thickness. *Chemistry of Materials* **1999,** 11, (8), 2132-2140.
7. vanBlaaderen, A.; Ruel, R.; Wiltzius, P., Template-directed colloidal crystallization. *Nature* **1997,** 385, (6614), 321-324.
8. Velev, O. D.; Kaler, E. W., Structured porous materials via colloidal crystal templating: From inorganic oxides to metals. *Advanced Materials* **2000,** 12, (7), 531-534.
9. Crocker, J. C.; Grier, D. G., Methods of digital video microscopy for colloidal studies. *Journal of Colloid and Interface Science* **1996,** 179, (1), 298-310.
10. Lu, P. J.; Zaccarelli, E.; Ciulla, F.; Schofield, A. B.; Sciortino, F.; Weitz, D. A., Gelation of particles with short-range attraction. *Nature* **2008,** 453, (7194), 499-U4.
11. Li, D. C.; Lam, C. N.; Biswal, S. L., Measuring short-range repulsive forces by imaging directed magnetic-particle assembly title. *Soft Matter* **2010,** 6, (2), 239-242.
12. Mirkin, C. A.; Letsinger, R. L.; Mucic, R. C.; Storhoff, J. J., A DNA-based method for rationally assembling nanoparticles into macroscopic materials. *Nature* **1996,** 382, (6592), 607-609.
13. Nykypanchuk, D.; Maye, M. M.; van der Lelie, D.; Gang, O., DNA-guided crystallization of colloidal nanoparticles. *Nature* **2008,** 451, (7178), 549-552.
14. Bevan, M. A.; Lewis, J. A.; Braun, P. V.; Wiltzius, P., Structural evolution of colloidal crystals with increasing ionic strength. *Langmuir* **2004,** 20, (17), 7045-7052.
15. Zahn, K.; Lenke, R.; Maret, G., Two-stage melting of paramagnetic colloidal crystals in two dimensions. *Physical Review Letters* **1999,** 82, (13), 2721-2724.
16. Alsayed, A. M.; Islam, M. F.; Zhang, J.; Collings, P. J.; Yodh, A. G., Premelting at defects within bulk colloidal crystals. *Science* **2005,** 309, (5738), 1207-1210.
17. Peng, Y.; Wang, Z.; Alsayed, A. M.; Yodh, A. G.; Han, Y., Melting of Colloidal Crystal Films. *Physical Review Letters* **2010,** 104, (20), 205703.
18. Leunissen, M. E.; Christova, C. G.; Hynninen, A. P.; Royall, C. P.; Campbell, A. I.; Imhof, A.; Dijkstra, M.; van Roij, R.; van Blaaderen, A., Ionic colloidal crystals of oppositely charged particles. *Nature* **2005,** 437, (7056), 235-240.
19. van Blaaderen, A., Materials science - Colloids get complex. *Nature* **2006,** 439,

(7076), 545-546.
20. Anderson, V. J.; Lekkerkerker, H. N. W., Insights into phase transition kinetics from colloid science. *Nature* **2002,** 416, 811-815.
21. Glotzer, S. C.; Solomon, M. J., Anisotropy of building blocks and their assembly into complex structures. *Nature Materials* **2007,** 6, 557-562.
22. Hynninen, A. P.; Thijssen, J. H. J.; Vermolen, E. C. M.; Dijkstra, M.; Van Blaaderen, A., Self-assembly route for photonic crystals with a bandgap in the visible region. *Nature Materials* **2007,** 6, (3), 202-205.
23. Smoukov, S. K.; Gangwal, S.; Marquez, M.; Velev, O. D., Reconfigurable responsive structures assembled from magnetic Janus particles. *Soft Matter* **2009,** 5, (6), 1285-1292.
24. Zerrouki, D.; Baudry, J.; Pine, D.; Chaikin, P.; Bibette, J., Chiral colloidal clusters. *Nature* **2008,** 455, (7211), 380-382.
25. Biswal, S. L.; Gast, A. P., Mechanics of semiflexible chains formed by poly(ethylene glycol)-linked paramagnetic particles. *Physical Review E* **2003,** 68, (2), 021402.
26. Goubault, C.; Leal-Calderon, F.; Viovy, J. L.; Bibette, J., Self-assembled magnetic nanowires made irreversible by polymer bridging. *Langmuir* **2005,** 21, (9), 3725-3729.
27. Vanapalli, S. A.; Iacovella, C. R.; Sung, K. E.; Mukhija, D.; Millunchick, J. M.; Burns, M. A.; Glotzer, S. C.; Solomon, M. J., Fluidic assembly and packing of microspheres in confined channels. *Langmuir* **2008,** 24, (7), 3661-3670.
28. Spencer, B. F.; Dyke, S. J.; Sain, M. K.; Carlson, J. D., Phenomenological model for magnetorheological dampers. *Journal of Engineering Mechanics-Asce* **1997,** 123, (3), 230-238.
29. Carlson, J. D.; Jolly, M. R., MR fluid, foam and elastomer devices. *Mechatronics* **2000,** 10, (4-5), 555-569.
30. Li, D. C.; Banon, S.; Biswal, S. L., Bending dynamics of DNA-linked colloidal particle chains. *Soft Matter* **2010,** 6, (17), 4197-4204.
31. Li, D. C.; Rogers, J.; Biswal, S. L., Probing the Stability of Magnetically Assembled DNA-Linked Colloidal Chains. *Langmuir* **2009,** 25, (16), 8944-8950.
32. Li, D. C.; Fakhri, N.; Pasquali, M.; Biswal, S. L., Axial thermal rotation of slender rods. *Physical Review Letters* **2011**, accepted.
33. Biswal, S. L.; Gast, A. P., Micromixing with linked chains of paramagnetic particles. *Analytical Chemistry* **2004,** 76, (21), 6448-6455.
34. Biswal, S. L., PhD thesis. **2004**, 20.
35. Koenig, A. Etude d'un polymère semi-flexible à l'aide de colloïdes magnétiques : exemple de l'ADN. Thèse de l'université Paris VI, Thèse de l'université Paris VI, 2005.
36. Gittes, F.; Mickey, B.; Nettleton, J.; Howard, J., Flexual rigidity of mircortubules and actin-filaments measured from thermal fluctuations in shape. *Journal of Cell Biology* **1993,** 120, (4), 923-934.
37. Biswal, S. L.; Gast, A. P., Rotational dynamics of semiflexible paramagnetic particle chains. *Physical Review E* **2004,** 69, (4), 9.
38. Badaire, S.; Cottin-Bizonne, C.; Woody, J. W.; Yang, A.; Stroock, A. D., Shape selectivity in the assembly of lithographically designed colloidal particles. *Journal of the American Chemical Society* **2007,** 129, (1), 40-41.
39. Zhao, K.; Mason, T. G., Directing colloidal self-assembly through roughness-

controlled depletion attractions. *Physical Review Letters* **2007,** 99, (26).
40. Biswal, S. L.; Gast, A. P., Mechanics of semiflexible chains formed by poly(ethylene glycol)-linked paramagnetic particles. *Physical Review E* **2003,** 68, (2), 9.
41. Biancaniello, P. L.; Kim, A. J.; Crocker, J. C., Colloidal interactions and self-assembly using DNA hybridization. *Physical Review Letters* **2005,** 94, (5).
42. Goubault, C.; Jop, P.; Fermigier, M.; Baudry, J.; Bertrand, E.; Bibette, J., Flexible magnetic filaments as micromechanical sensors. *Physical Review Letters* **2003,** 91, (26), 4.
43. Dreyfus, R.; Baudry, J.; Roper, M. L.; Fermigier, M.; Stone, H. A.; Bibette, J., Microscopic artificial swimmers. *Nature* **2005,** 437, (7060), 862-865.
44. Milam, V. T.; Hiddessen, A. L.; Crocker, J. C.; Graves, D. J.; Hammer, D. A., DNA-driven assembly of bidisperse, micron-sized colloids. *Langmuir* **2003,** 19, (24), 10317-10323.
45. Valignat, M. P.; Theodoly, O.; Crocker, J. C.; Russel, W. B.; Chaikin, P. M., Reversible self-assembly and directed assembly of DNA-linked micrometer-sized colloids. *Proceedings of the National Academy of Sciences of the United States of America* **2005,** 102, (12), 4225-4229.
46. Biancaniello, P. L.; Crocker, J. C.; Hammer, D. A.; Milam, V. T., DNA-mediated phase behavior of microsphere suspensions. *Langmuir* **2007,** 23, (5), 2688-2693.
47. Cebers, A., Flexible magnetic filaments. *Current Opinion in Colloid & Interface Science* **2005,** 10, (3-4), 167-175.
48. Koenig, A.; Hebraud, P.; Gosse, C.; Dreyfus, R.; Baudry, J.; Bertrand, E.; Bibette, J., Magnetic force probe for nanoscale biomolecules. *Physical Review Letters* **2005,** 95, (12).
49. Cebers, A., Flexible magnetic filaments in a shear flow. *Journal of Magnetism and Magnetic Materials* **2006,** 300, (1), 67-70.
50. Cebers, A.; Cirulis, T., Magnetic elastica. *Physical Review E* **2007,** 76, (3).

Chapter 2

Stability control of DNA-linked paramagnetic particle chains

The self-assembly of colloidal particles using DNA linker molecules has led to novel colloidal materials. This chapter describes the development and characterization of a new class of linear colloidal structures based on combining the directed assembly of paramagnetic particles and linking them together with DNA. A key obstacle to assembling these structures is understanding the fundamental chemistry and physics of the assembly processes. The stability of these cross-linked chain structures is the first step towards reliable assembly and thus important for its applications; however, chain stability has yet to be systematically studied. In this chapter, the stability of DNA-linked paramagnetic colloidal chains as a function of externally applied magnetic field strength and particle surface grafted DNA length and density is investigated theoretically and experimentally. A total inter-particle free energy potential model is developed to account for the major forces contributing to chain stability. A pseudo-phase diagram is obtained

from experiments to illustrate regions of stable and unstable particles: unlinked particles, linked chains, and their transition. This phase diagram agrees well with those predicted by the model. From this study, optimized parameters for successful linking and building stable linked chains are obtained.

2.1. Literature review of experimental studies on specific interactions and self-assembly of colloidal particles

Researchers are making rapid progress in the design and synthesis of novel colloidal materials that emulate the properties of natural materials. Self-assembly has been a route many have taken towards the development of bioinspired materials with well-defined chemical and physical properties[1-3]. Understanding the interactions between colloidal particles has long been a key issue in controlling colloidal self- assembly and building novel materials and devices. Non-specific interactions, such as van der Waals and electrostatic forces, are well characterized by existing theories, such as Derjaguin, Landau, Verwey, and Overbeek (DLVO) theory. However, specific interactions, such as interactions between colloidal particles mediated by biological complexes, including proteins and DNA, are not well understood. Self-assembled, field-controllable structures are readily formed from magneto-responsive colloidal particles. At sufficiently high field strengths, the particles align, forming chains or columns, which revert to an isotropic suspension when the field is removed. I have developed a technique to create linear chains of permanently linked particles by cross-linking the particles with DNA under the

influence of an external magnetic field. These linked chains can be thought of as colloidal analogs to polymer chains: "colloidal polymers".

The inter-particle free energy between randomly dispersed particles is the same order of magnitude as thermal energy, $k_B T$, as investigated in several systems[4-9]. Taking advantage of the high specificity of DNA, inter-particle interactions can be regulated to form highly ordered structures[4, 10-13]. DNA-nanoparticle assembly systems were first investigated by Alivisatos[10] and Mirkin[11]. Their approach to form DNA-mediated nanoparticle clusters was to mix two batches of nanoparticles, one batch grafted with single-stranded DNA and the other batch grafted with the complimentary DNA sequence. These nanoparticle clusters have demonstrated potential in nanoengineering[11], sensing[14] and biodetection[15] applications. However, these clusters lack specific order or structure control. In order to build a linked colloidal structure with well-defined properties, it is important to understand the interactions between these surface modified particles. Crocker et al[4-6, 16] was among the first to demonstrate that the reversibility of DNA-functionalized particle aggregation can be tuned using the surface polymer brush length[5]. They also constructed a phase diagram attributing the degree of aggregation to salt concentration and linker DNA packing density on particle surfaces[6]. A similar system was studied by Nykypanchuk et al[7] in which analysis of inter-particle interaction energies was considered.

By chemically crosslinking paramagnetic particles in the presence of an external magnetic field, well- defined linked linear colloidal chains can be created[17-19]. Paramagnetic particles align themselves under an externally applied homogenous magnetic field into linear chain structures with a dipole interaction energy much larger

than the thermal energy, k_BT. Bibette et al. has investigated polymer-mediated magnetic particle chain systems[18, 20-23] and studied the dependence of particle stability on the bridging polymer concentration and particle volume fraction[22]. Unstable chains cannot withstand thermal fluctuations, thus disperse in these systems[20, 22]. The dependence of chain stability on magnetic field and polymer properties has not been systematically characterized in these systems.

In this chapter, I study the stability of micron-sized paramagnetic particle chains linked by short DNA strands, as shown in Figure 2.1(a). In particular, the parameters used to investigate the stability of these chains are the applied magnetic field directing particle assembly and the length and density of surface DNA used to link the particles. The physics of directed DNA-linked particle assembly is very different from the random aggregation that has been both theoretically[24] and experimentally[6-9] studied. Directed magnetic particle assembly is controlled by the attractive magnetic energy between particles. This controllable attractive interaction, where the interaction potential energy can be varied from k_BT to thousands of k_BT's, can be utilized to control DNA-mediated colloidal particle interactions. I have constructed a phase diagram that describes the competition between attractive and repulsive interactions between particles as a function of magnetic field strength and linker DNA length. A total energy landscape is derived from theory to predict the values of inter-particle potentials and determine the conditions for successful linking of particles into stable chains. The predicted transitions between linked and non-linked chains agree well with the experimental results. An interesting result found is that the external magnetic field may actually hinder particle assembly into

stable chains depending on the inter-particle interactions.

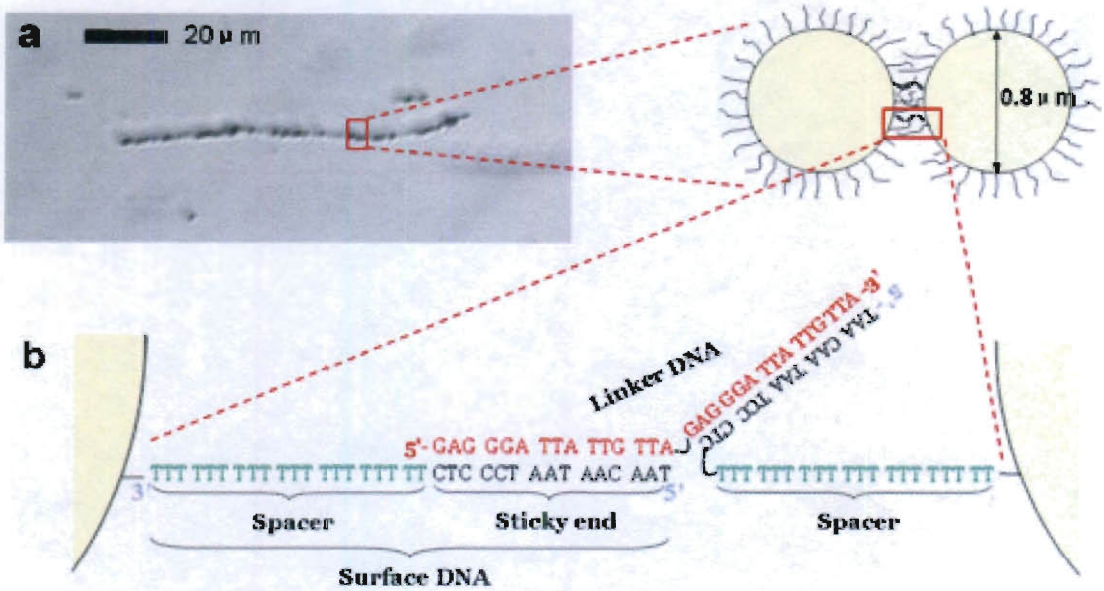

c

	Base sequence
Surface DNA	3' - NH_2-T_x-CTC CCT AAT AAC AAT -5'
Linker DNA	5'- GAG GGA TTA TTG TTA GAG GGA TTA TTG TTA -3'

Spacer T_x represents a sequence of x thymine base pairs, for example,
T_{20} = TTT TTT TTT TTT TTT TTT TT

Figure 2.1. a) An optical microscope image of a DNA-linked paramagnetic particle chain. b) Schematic showing the hybridization of surface grafted ssDNA and the linker ssDNA. c) A table containing the sequences of both surface DNA and linker DNA. Surface DNA is composed of a "sticky end" (3'-CTCCCTAATAACAAT-5') and a"spacer DNA" (3'-T_x-5'), which can vary in length from 0 to 25 bases. The total length of surface DNA varies from 15 to 40 bases.

2.2. Literature review of experimental studies on specific interactions and self-assembly of colloidal particles

2.2.1. Sample preparation

DNA-functionalized paramagnetic particles are prepared by coupling carboxyl-coated paramagnetic particles (Seradyn Inc., Indianapolis, IN) with 3'-primary amine modified DNA oligomers (Integrated DNA Technologies, Coralville, IA). Each of these spherical particles has a polystyrene core, a magnetite encapsulated layer and a polymer surface containing carboxyl groups. The average diameter of these particles is 0.8 micrometers. In this system I use a surface DNA, which is grafted to the particle surface, and a linker DNA, which is used to hybridize adjacent particles together.

The surface DNA is composed of two parts, as shown in Figure 2.1(b). The first is an identical 15-base sequence at the free end that is complementary to half of the linker DNA, which is referred to as the "sticky end". The length and sequence of the sticky end is held constant. The other part of the surface DNA is poly-thymine sequence which acts as a "spacer DNA", extending the sticky end away from the particle surface. The "spacer DNA" is varied from 0 to 25 bases; thus the total length of ssDNA grafted to the particle surface ranges from 15 to 40 bases. The linker DNA, shown in Figure 2.1c, is a symmetric 30-base oligonucleotide designed to hybridize sticky ends from adjacent particle surfaces.

Grafting the surface DNA to particle surfaces is achieved by dispersing carboxyl particles in MES buffer solution (2-(N-morpholino)ethanesulfonic acid, pH 4.7, Thermo Scientific, Rockford, IL) with 3'-primary amine modified surface DNA at a concentration

of $15\mu M$ and EDAC (Pierce Chemicals Inc., Indianapolis, IN) at a concentration of 25mg/mL for 3 hours under room temperature. After incubation, DNA grafted particles are separated from solution DNA by pulling the particles down in a centrifuge tube using magnets and removing the supernatant containing solution DNA. The supernatant is replaced with phosphate buffer solution (PBS, 0.12mM, pH 7.4). Resuspension of particles is achieved by vortexing before the dispersion is ready for the next cycle of washing. This washing procedure is repeated three times to remove the excess surface DNA. The final volume of the dispersion is brought to 0.5mL by adding PBS buffer solution.

2.2.2. Surface grafting density measurement

A fluorescence-based method is used to measure the average number of DNA strands on the particle surfaces that are available to hybridize. I start with a solution of fluorescently labeled DNA (5'-GAGGGATTATTGTTA/TexasRed-XN/-3', Integrated DNA Technologies, Coralville, IA) with a complementary sequence to the surface DNA at a known concentration. To this solution, particles containing surface grafted DNA are added. The suspension is incubated for 2.5 hours to ensure hybridization between the surface DNA and fluorescently labeled DNA. The particles are removed from the suspension using magnets as previously described. The average number of hybridized DNA strands is calculated from the difference in fluorescence intensity of the solution before and after incubation. The average surface DNA grafting density, σ, decreases with the increasing surface DNA length. The measured σ ranges from

3.7×10^4 $strand/\mu m^2$ for particles with 40-base surface DNA to 7.0×10^4 $strand/\mu m^2$ for particles with 15-base surface DNA. The total number of DNA strands grafted on particle surfaces may be larger than the measured values which represent only the strands that are available for hybridization; however, given the average area $16nm^2 \sim 30nm^2$ each strand occupies, which are similar to the corresponding packing area of surface DNA that are specifically bonded, it is reasonable to argue that the non-specific binding ratio of DNA to particle surface is relatively small.

2.2.3. Linking experiments

The particle linking experiments are done in a flow cell of size $2cm\times2cm\times100\mu m$, as shown in Figure 2.2(a). The flow cell is placed between two block magnets, which generates a uniform magnetic field at the center of the flow cell, depicted in Figure 2.2(b), and is measured using a Gaussmeter. The DNA-functionalized particle suspension (1×10^6 $particles/\mu L$) and linker DNA solution ($30\mu M$) are mixed and immediately injected into the flow cell, which is sealed to prevent evaporation. The concentration of particles and DNA linker solution is held constant for all experiments. The system is kept under an inverted microscope at room temperature for 2.5 hours before the magnets are removed and observations of how linked particles made. This time is sufficiently long to ensure that linking behavior is time independent. Experiments taking place at longer incubation times showed no significant deviation on the percentage of particles linked when observed. Therefore, only the thermodynamic stability of the system is considered in this chapter instead of the kinetics of assembly.

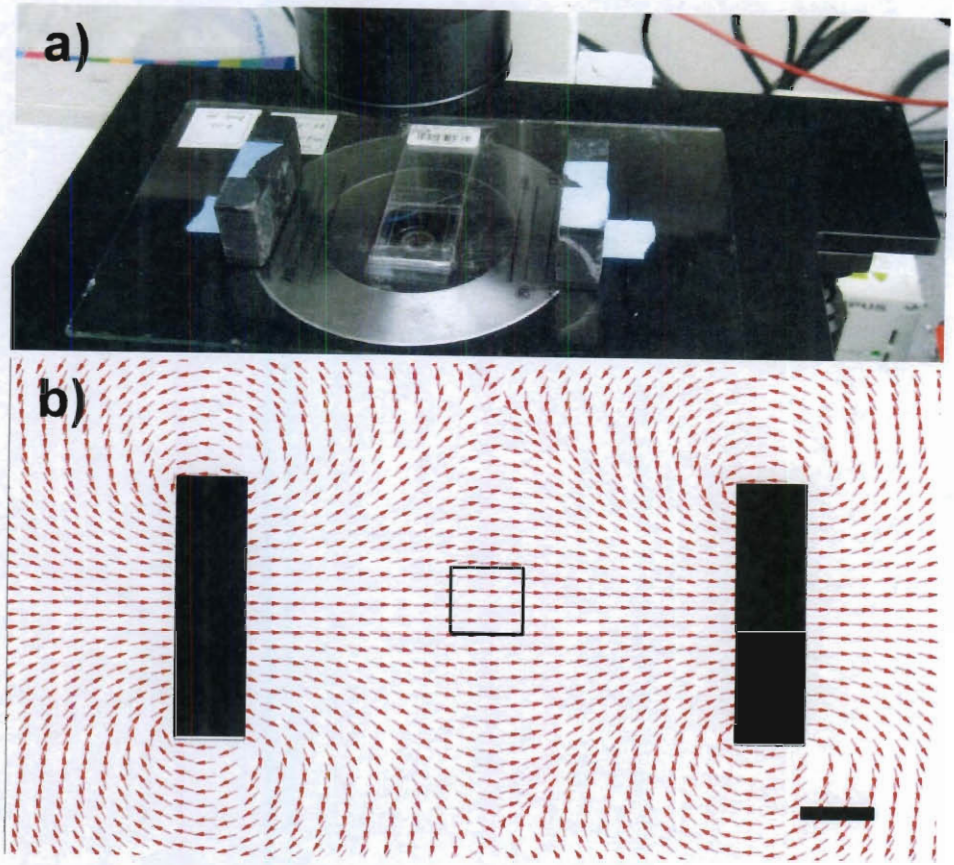

Figure 2.2. a) Experimental setup illustrating flow cell between two block magnets. b) The magnetic field is measured using a gaussmeter probe and plotted. The black rectangles represent the block magnets and the open square is the flow cell. Scale bar: 2cm.

2.2.4. Image processing

The particle aligning and linking process is allowed to proceed for 2.5 hours before the images are recorded at the marked region shown in Figure 2.2 upon field removal. The marked region of the sample is observed using an inverted optical microscope with an 20× objective (Olympus IX71, Olympus America Inc., Melville, NY). Images of the

marked region taken both before and after the magnetic field is removed are captured using a CCD (Orca-HR, Hamamatsu Inc., Sewickley, PA). For each image, the sum of the lengths of all the chains is determined numerically using imaging software (Simple PCI, Hamamatsu Inc., Sewickley, PA). The ratio of total chain length to bead diameter gives the number of particles in a chain. For a given length of spacer DNA, the stability of the linked chains under various magnetic field strengths is determined. For example, as shown in Figure 2.3(a), particles are aligned with a given magnetic field strength. The particles with linker DNA are then incubated for 2.5 hours to allow for duplexes to form between particles. After incubation, the magnetic field is removed and the resulting chains are observed. Percentages of linked particles versus total number of particles are calculated by comparing the pairs of images taken before and after the removal of magnetic field. This percentage is defined to be the linked particle ratio and is a measure of the chain stability. As shown in Figure 3(b-e), for a given spacer DNA length, the linked particle ratio varies as a function of magnetic field strength applied during incubation. Each set of experiment with fixed parameters is repeated 4~6 times. The measured linked particle ratios are averaged over the repetitions with error bars ranging from 0 to ±5%. Figure 2.3 illustrates examples of pairs of images and the numerically determined linked particle ratios.

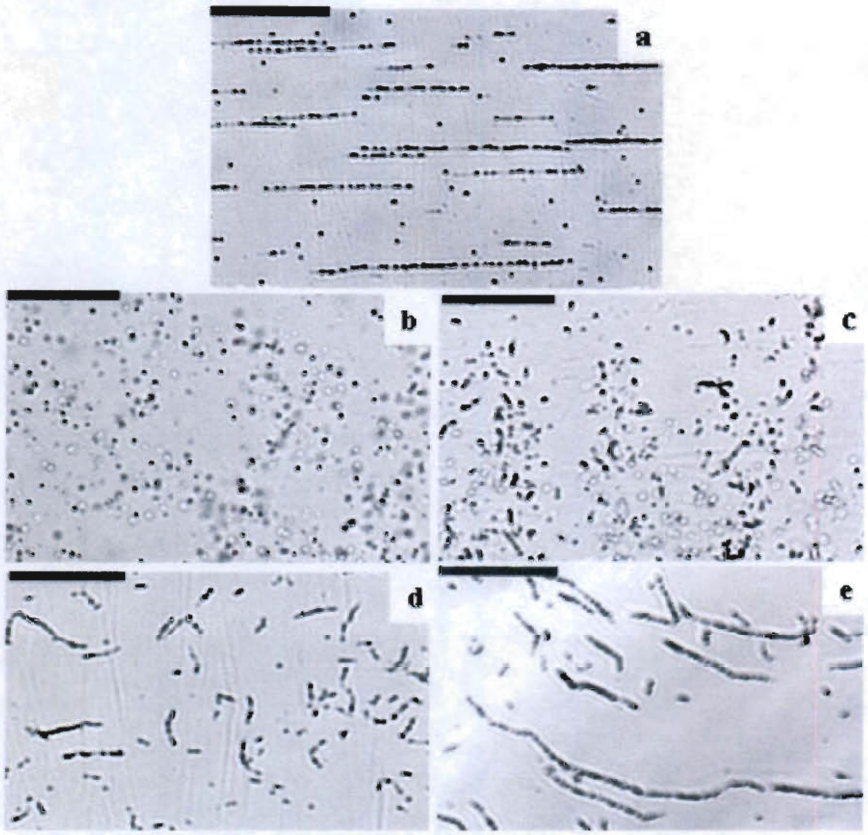

Figure 2.3. Results for 15-spacer surface DNA coated particles taken before and after removal of a magnetic field. Linked particle ratios are included as percentages for each figure. Scale bar: 20μm a) Example of particles aligned using a magnetic field strength of 150 Gauss. b) - e) are images taken 5 minutes after removal of different applied magnetic field strengths, with linked particle ratios followed. b) Unlinked particles (0%) after removal of magnetic field of 20 Gauss. c) Linked chain + unlinked particles (30%) after removal of magnetic field of 40 Gauss. d) Linked chains (95%) after removal of magnetic field of 100 Gauss. e) Linked chains (100%) after removal of magnetic field of 200 Gauss.

2.3. Theory

The inter-particle potential between end-grafted colloidal particles can be divided into attractive and repulsive interactions. The three major contributions to the attractive interaction between particles are magnetic dipole-dipole interactions, van der Waals interactions, and DNA hybridization between particles. There are two major components to the repulsive interaction: steric repulsion between grafted surface DNA and the electrostatic repulsion between neighboring charged particles surfaces. In this section, I consider these interactions and combine them to obtain a total energy landscape.

2.3.1. Magnetic dipole-dipole interaction

The paramagnetic particles used in this study are polystyrene microspheres with iron oxide grains embedded within the polymer matrix. When an external magnetic field of magnitude H_o is applied, the particles acquire an induced dipole moment, $\mu = \frac{4}{3}\pi a^3 \mu_o \chi H_o$, where a and χ are the particle radius and susceptibility, and μ_o is the magnetic permeability of vacuum. Two particles with aligned dipole moments have an attractive interaction with energy given by Equation 2.1,

$$E_{mag}(r,\alpha) = \frac{\mu^2}{4\pi\mu_o}\frac{(1-3\cos^2\alpha)}{r^3} \tag{2.1}$$

where r is the distance between sphere centers and α is the angle between the applied field and the sphere center. The interaction energy between two touching particle is given by Equation 2.2:

$$E_{mag} = -\frac{\pi a^3 \mu_o \chi^2 H_o^2}{9} \tag{2.2}$$

The magnetic susceptibility of our particles, determined experimentally, is $\chi = 2.0 \pm 0.6$. The magnetic interaction energy can be easily plotted against applied magnetic field strength. This attractive energy potential functions as a parameter to control particle spacing during the linking process but disappears upon removal of the magnetic field.

2.3.2. van der Waals and electrostatic interactions

DLVO theory is used to account for both van der Waals attractive interactions and electrostatic repulsive interactions, which can be easily calculated as a function of inter-particle distance. DLVO interactions are very important in most colloidal systems because they are usually the major inter-particle potential contributor and are much larger than thermal energy, $k_B T$. Although the DLVO interaction energies between particles at the inter-particle distance range we are operating are on the order of $100\,k_B T$, they are almost negligible compared to steric repulsion and magnetic attraction energies, which are on the order of $10^4\,k_B T$.

2.3.3. DNA hybridization

DNA hybridization is considered an attractive interaction in this analysis since the hybridized duplexes resist particle separation. The free energy change of DNA hybridization is the amount of energy a duplex provides towards linking particles together. This energy is estimated from a nearest-neighbor (NN) model for a solution of bulk DNA at 25°C, proposed by Santalucia[25]. A potential of $31.7\,k_BT$ for our 15-base linker DNA, which I denote as the sticky end, is calculated. However, due to the entropic penalty caused by end-grafting confinement, I expect that the actual value of the DNA bridging energy is lower than $31.7\,k_BT$. Additionally, this model accounts for the bending free energy difference between the free solution and the confined DNA between the particles and ignores torsional entropy. The energy required to bend an ssDNA strand into a curvature of unity is estimated as $3\,k_BT$, thus the average DNA bridging energy per linkage, ΔG_{DNA}, is approximately $28.7\,k_BT$.

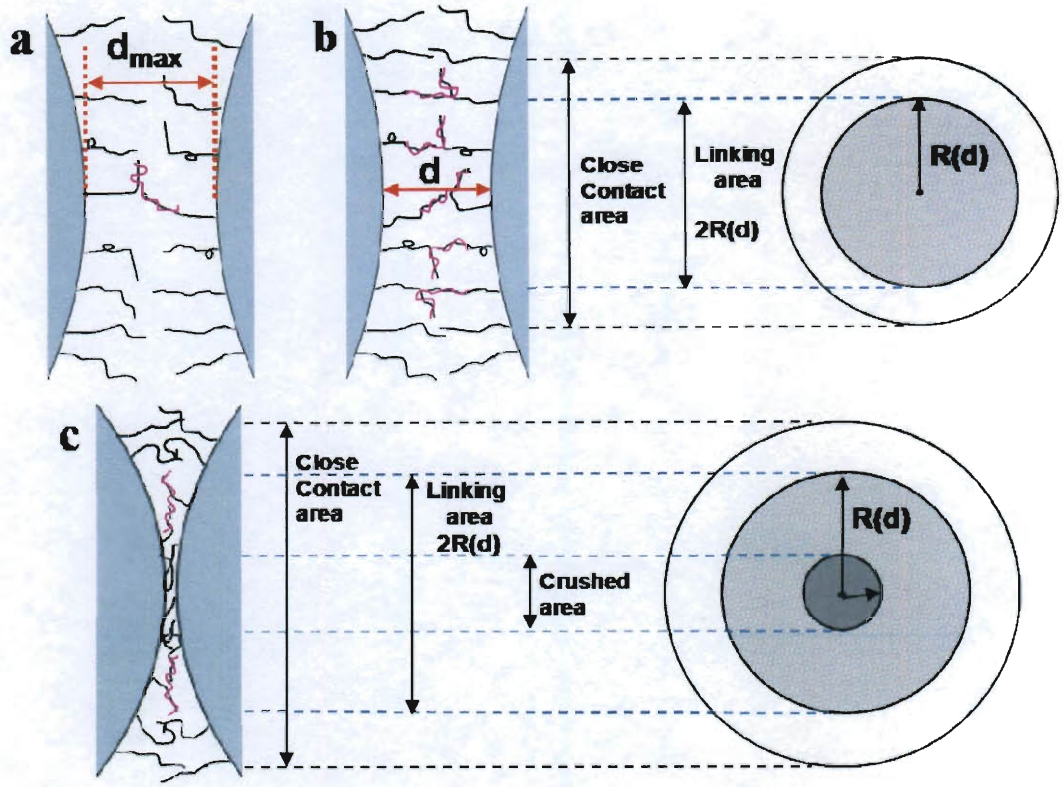

Figure 2.4. Schematic illustrating DNA linking geometry between two adjacent spheres. a) The onset of DNA bridging occurs at the maximum inter-particle distance, d_{max}. b) For the general linking case when $d < d_{max}$, multiple DNA bridges are formed between particles. c) When *d* approaches zero, a "crushed" region at the center of contact emerges where duplexes are unable to form.

The total DNA bridging energy between the spheres is given by Equation 2.3,

$$E_{DNA} = \Delta G_{DNA} \cdot n_{DNA-bridge}(\sigma, d) \qquad (2.3)$$

where $n_{DNA-bridge}$ is the total number of bridges between adjacent spheres and is a function of the surface DNA grafting density, σ, and inter-particle distance, d. The area where DNA hybridization is possible is encompassed by a circle of radius, $R(d)$, calculated in nanometers by Equation 2.4,

$$R(d) = \sqrt{a^2 - \left(a + \frac{d}{2} - \frac{0.34 \times 15 + 0.68 \times 2n}{2}\right)^2} \tag{2.4}$$

where n is the number of thymine bases in the spacer ssDNA sequence.

The largest inter-particle distance, d_{max}, is obtained at the onset of the DNA hybridization, as shown in Figure 2.4(a), when $R(d_{max}) = 0$. This happens when two ssDNA strands are in registry at the close contact point between two particles and are able to form duplex with the linker DNA. As particles move closer together, d decreases and $R(d)$ increases, making it possible to form more linkages between particles, as depicted in Figure 2.4(b). Eventually, as d approaches zero, a crushed region emerges where duplexes are unable to form. However, there exists a concentric region outside this crushed region where DNA duplexes are able to form, as shown in Figure 2.4(c). For example, in the case of a 15-base surface DNA and an inter-particle distance d = *0,* the available linking area has a radius of R(d) = 69.5 nm resulting in a total available linking area of 15,395 nm^2, and a "crushed" area of 3,777 nm^2 (less than one-forth of the total linking area). This suggests that duplex formation occurs even when the interparticle distance is smaller than the DNA brush height.

With this radius and DNA surface grafting density, the total DNA bridging energy can be computed from Equation 3 using $n_{DNA-bridge} = \pi R^2(d) \cdot \sigma$. Note that the above equations used to calculate total DNA energy assume that 100% of the ssDNA strands are hybridized. As suggested above, experimentally this is not the case since surface DNA strands may not be in registry, linker DNA strands may find difficulty diffusing to the center of the linking area, or ΔG_{DNA} not be $28.7\,k_BT$ since some strands in the center are more compressed thus more curved and some outside might be of straighter configurations. However, this energy calculation provides an upper limit for the attractive potential energy due to DNA hybridization.

2.3.4. Steric repulsion

There is a loss of conformational freedom and increase in osmotic pressure as polymer brushes approach one another. Steric repulsion is a repulsive interaction generated by confinement of polymer brushes. Theoretical investigations of steric repulsion include Self-Consistent Field Analysis (SCF) [26, 27], molecular dynamics (MD)[28], Monte Carlo (MC) simulations, and scaling analysis[29, 30]. For this system, I use the analytical Self-Consistent Field Analysis for the free energy per unit area as a function of brush height between polymer brushes on flat surfaces obtained by Milner et al.[31]. The free energy per unit area as a function of height is given as,

$$f(u) = \frac{5}{9} f_0 \left(\frac{1}{u} + u^2 - \frac{u^5}{5} \right) \tag{2.5}$$

where the variable u is defined as $u \equiv h/h_0$ with h and h_0 being compressed and uncompressed polymer brush thickness, respectively, and f_0 is the free energy per unit area of the uncompressed brush. By applying the Derjaguin approximation, the above formula can be used to calculate the repulsive energy between polymer brushes on adjacent spherical particles. While the conventional formula to describe the force versus distance between two surfaces bearing polymer brushes, derived using scaling theory by de Gennes and Alexander[32, 33], has long been used to fit Surface Force Apparatus (SFA) data, it does not provide the specific force values and the prefactor must be determined by fitting. Though the formula introduced by Milner and coworkers was originally derived to describe a polymer brush compressed by an impenetrable surface[34], it agrees reasonably well with SFA force-distance data of two surfaces bearing monodisperse polymer brushes[32, 35] and does not require any fitting parameters. Thus, end-grafted ssDNA on particle surfaces can be treated as polymer brushes and Milner's formula can be applied to compute the steric repulsive energies between adjacent DNA layers. The values for h_0 and f_0 are calculated using[35],

$$h_0 = \left(\frac{12}{\pi^2}\right)^{1/3} N\sigma^{1/3} w^{1/3} v^{-1/3} \tag{2.6}$$

$$f_0 = \frac{9}{10}\left(\frac{\pi^2}{12}\right)^{1/3} N\sigma^{5/3} w^{2/3} v^{1/3} \tag{2.7}$$

where w is the excluded volume parameter; N is the number of Kuhn segments in the chain, and v, with the dimension of length^{-2}, is related to the chain radius of gyration as $v = m\left(2R_g^2\right)^{-1}$. N can be calculated as the length of ssDNA divided by its Kuhn length, *l*, which is estimated to be 2.4 nm[33, 36] in a aqueous environment with salt concentration 0.12 M. Therefore, for a 15 base surface DNA $N \approx 4$ and for a 40 base surface DNA $N \approx 11$. I approximate ssDNA as charged cylinders and calculate its excluded volume parameter[37] as $w = 1.5l^2 d_{eff}$, where $d_{eff} = 2.7nm$ is the effective diameter of the ssDNA backbone calculated by summing half of dsDNA diameter, $1nm$, and twice the Debye length, $1.7nm$, in a 0.12 M solvent. Equations 6 and 7 show that $h_0 \approx 6.6nm$ and $f_0 \approx 0.29 k_B T / nm^2$ for 15 base surface DNA brush while $h_0 \approx 14.6nm$ and $f_0 \approx 0.27 k_B T / nm^2$ for 40 base surface DNA brush with surface grafting densities of $7.0 \times 10^4\ strand/\mu m^2$ and $3.7 \times 10^4\ strand/\mu m^2$, respectively. The steric repulsive energy between brushes on two spherical particles can be calculated using the Derjaguin approximation, shown in Equation 2.8,

$$E_S(d) = \int_0^{R_c} \left[f\left(b(r)\right) - f(2h_0) \right] \cdot 2\pi r dr \qquad (2.8)$$

where R_C is the radius of the contact area between two spheres and is determined using the geometric argument $R_C = \sqrt{\left(a + h_0\right)^2 - (a + d/2)^2}$, r is the radius of ring in the contacting area where the DNA brush height stays constant and b, described by

$b(r) = a - \sqrt{a^2 - r^2} + d/2$, describes the distance between particles as any given r. Integrating the compression free energy for the entire contacting area gives the steric repulsive energy between two particles.

2.3.5. Total energy landscape

With the exception of the magnetic energy, the aforementioned interaction energies are combined to give the total inter-particle free energy, shown in Equation 2.9. This energy landscape can be plotted as a function of inter-particle distance, d. These plots show the total energy at a function of inter-particle distances for magnetic particles with varying surface DNA lengths in the absence of the magnetic field. These plots can be utilized to determine whether particles can form stable linked chains or fall apart upon removal of the magnetic field. The inter-particle distance is obtained by balancing the magnetic with the van der Waals attractive energy, steric, and electrostatic repulsive energy at a given magnetic field strength.

$$E_{tot}(d,\sigma,Z) = E_S(d,\sigma) + E_{DNA}(d,\sigma) + E_{vdW}(d) + E_{el}(Z,d) \qquad (2.9)$$

For an inter-particle distance where the total energy is above zero, theory predicts that particles will have a net repulsive interaction energy upon the removal of magnetic field, which will lead to broken DNA linkages between particles and unstable chains. At a distance where the total energy is below zero, particles will stay linked after the field is removed, ensuring stable chains.

2.4. Results and discussion

To demonstrate that linear DNA-linked magnetic chains can be formed, linking experiments using a variety of magnetic field strengths and surface DNA lengths are conducted. The experiments presented utilize a magnetic field in the range of 20 to 1200 Gauss and surface DNA lengths from 15 to 40 bases. The magnetic field strength is converted into magnetic energy using Equation 2. The percentages of particles that are linked at the different conditions upon removal of magnetic field are shown in Figure 5. I define systems in which the linked particle ratio is larger than 90% as the "linked chain phase", represented by filled squares. In this phase, the linked chains are stable and there are very few dispersed particles. Systems which have linked particle ratios between 20% and 60% are denoted as the "linked chain + unlinked particles" phase, represented by half-filled squares. In this phase, short chains and dispersed particles are observed. Finally, systems which have linked particle ratios below 5% are defined as the "unlinked particle" phase, represented by open squares. In this phase there are mostly dispersed particles. These three distinct phases can be easily identified on this phase diagram.

The transition between phases can also be determined using our model for the total energy landscape. For a given particle system, with an unique surface DNA grafting density, the total energy is calculated using Equation 9. This total energy balance can be used to determine the inter-particle distance, d , for a given surface DNA length. This inter-particle distance corresponds to a magnetic energy, as described in the previous section. The two blue dashed lines in the phase diagram are phase transition predictions

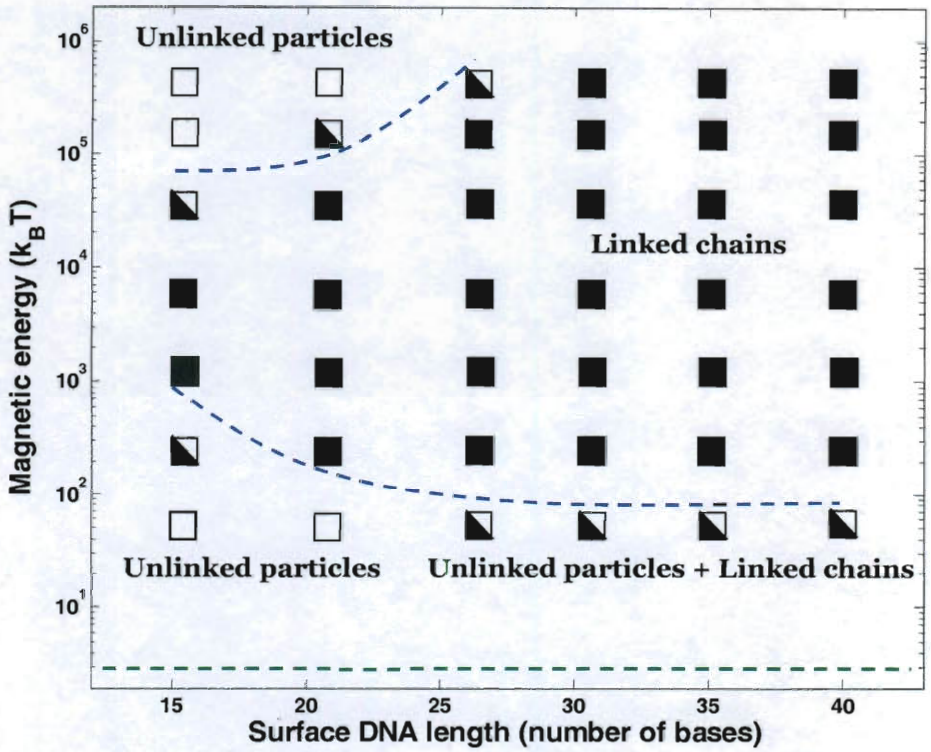

Figure 2.5. Experimental phase diagram for DNA-link chains upon field removal showing unlinked particles (open squares, linked particle ratio < 5%), unlinked particles + linked chains (half-filled squares, linked particle ratio from 20% to 60%), and linked chains (filled squares, linked particle ratio > 90%) regions as a function of magnetic energy applied during chain linking and length of surface DNA. The blue dashed lines are obtained from the total energy calculations to predict the transitions between linked and unlinked particles upon field removal. The green dashed line is the threshold energy needed for particle alignment.

calculated from the total energy landscape where the net total energy curves cross zero. The assumption implicitly made in the total energy calculation assumes that all particles are identical in size, magnetic susceptibility, and shape; however, there are variations in

the size and roughness of the particles. Thus, there are transition regions where linked chains and unlinked particles coexist. Nevertheless, as shown by the phase diagram, the total energy landscape model predicts the transition between linked and unlinked colloidal chains very well. The green dashed line is the minimum magnetic energy needed for particle chaining. In the following section, I discuss the role of the three main parameters determining linked chain stability: magnetic field strength, surface DNA length and DNA surface grafting density.

2.4.1. Effect of magnetic field strength

The first trend in the phase diagram is that at low magnetic field strengths (<100 Gauss or $<10^3\ k_BT$), increasing magnetic field strength results in a larger fraction of linked particle chains. This is not surprising, since stronger magnetic fields cause the distance between particles to decrease during the linking process. This results in a larger linking area and more possible DNA bridges between particles. This trend is captured both theoretically, as the total energy becomes more negative as the inter-particle distance decreases, and experimentally, as the linked particle ratio increases with stronger magnetic field strengths. What is interesting is that at high magnetic field strengths ($>10^4$ k_BT), there are less linked chains for surface DNA length smaller than 31 bases. Counterintuitive as it is, this trend is predicted by the total free energy landscape. Strong magnetic fields cause the particles to jam together, resulting in a larger steric repulsion between particles upon removal of the magnetic field. Though there is an increase in the number of DNA bridges at closer contact, upon field removal the strong repulsion

between particles cause the DNA bridges to break. This trend is confirmed experimentally as shown in the upper left region of the phase diagram.

2.4.2. Effect of surface DNA length and grafting density

Surface DNA length, as both predicted by theory and shown by experiments, plays an important role in determining whether successful linking of stable chains can be achieved. It is apparent from the phase diagram that a longer surface DNA will result in a larger region of stable, linked chains, where more particles are linked into chains over a wider range of applied magnetic field strengths. From the total energy landscape calculations, an increase in the surface DNA length increases the DNA linking area and thus the number of DNA bridges. This results in a larger DNA bridging energy, leading to more stable chain structures. This effect is evident in the shorter surface DNA length regime (from 15 to 27 bases), where an increase in surface DNA length substantially increases the range of magnetic field strengths in which the chains remain stable after field removal. However, at surface DNA lengths longer than 31 bases, there is little change in the stability of the chains with varying magnetic field strengths. This experimental observation can be understood from our model equations. The DNA bridging energy has a linear dependence on DNA grafting density $E_{DNA} \sim \sigma$ while steric repulsive energy varies with σ as $E_{DNA} \sim \sigma^{5/3}$. Additionally, increases in surface DNA length results in decreases in surface DNA grafting density, σ. Due to the competition between DNA bridging and steric repulsion between grafted surface DNA, there is an optimal DNA grafting density in which the total attractive energy can be maximized.

Below this optimal density, there are too few surface DNA available to form bridges. Above this grafting density, strong repulsion between particles due to compressed surface DNA brushes is likely to break the hybridized DNA bridges between particles upon field removal. Finally, longer surface DNA increases the bridging area, which increases the DNA bridging energy. These arguments suggest that particle systems with longer surface DNA have stronger DNA bridging energies to withstand the steric repulsion upon field removal.

2.4.3. Individual comparisons between theory and experiments

Besides the trends observed from the phase diagram, detailed information can be found by comparing the calculated total energy landscape curves with corresponding experimental results. For chains formed using particles grafted with a 15-base surface DNA, the total energy curve, calculated by inputting the experimentally obtained $\sigma = 7.0 \times 10^4 \; strands/\mu m^2$ into Equation 2.9, and experimental data are shown in Figure 2.6. As magnetic field strength increases from 20 Gauss ($E_{mag} \approx 80 k_B T$ based on $\chi = 2.0$) to 1200 Gauss ($E_{mag} \approx 2 \times 10^5 k_B T$), the corresponding inter-particle distance decreases from 8nm to almost zero. Experimentally obtained linked particle ratios are plotted to indicate whether the samples experimentally formed stable linked chains at a given inter-particle distance. As can be clearly seen, data points where the total energy curve is above zero (net repulsive energy) always have less than 30% particles linked; data points at the valley of the total energy curve that are below zero energy (net attractive energy) have close to 100% of the particles linked. For this particular particle

system, the minimum in the total energy relates an optimal linking magnetic strength of 180 Gauss, which corresponds to an inter-particle distance of 2.1 nm. Particles are unable to form stable chains at magnetic field strengths lower than 90 Gauss (inter-particle distance 3.4 nm) or larger than 360 Gauss (inter-particle distance 1.4 nm). Note that the phase containing unlinked particles and linked chains are found when the calculated net total energy is positive, contradicting the prediction by the model of completely unlinked

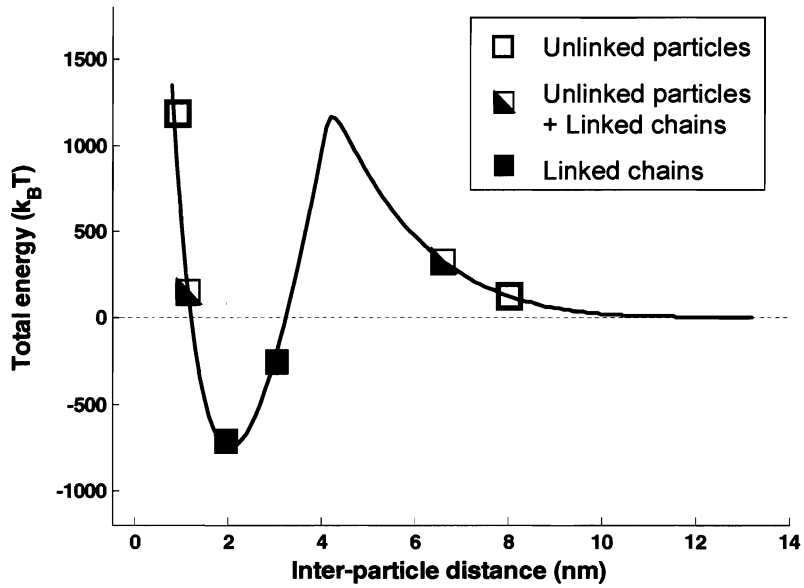

Figure 2.6. a) Total energy landscape for particles grafted with 15-base surface DNA at an average surface DNA grafting density of $\sigma = 70,000\, strands/\mu m^2$. Experimental data points of measured linked particle ratios are placed along the total energy curve at inter-particle distances corresponding to the magnetic field strength applied.

particles. I associate this discrepancy between experimental results and our theoretical model to be due to our inability to accurately describe the bridging energy associated with short surface DNA. I will later show that for surface DNA lengths greater than 21 bases, there is no contradiction between experimental results and model predictions.

As the surface DNA length increases from 15 to 21 bases, the total energy curve changes in magnitude due to the change in flexibility of the surface DNA strands, shown in Figure 2.7. The additional 6 DNA bases in the spacer sequence increases the available linking area, thus increasing the DNA bridging energy. However, transitions between phases are still clearly shown in the total energy curve and linked particle ratios. For particles with a surface DNA length of 21 bases, the total energy curve becomes wider and deeper, indicating a broader range of magnetic field strengths in which stable chains can be formed.

The role played by magnetic field strength is less evident experimentally for particles functionalized with longer (≥ 31 bases) surface DNA, where they form linked chains at all the experimental magnetic field strengths. As shown in Figure 2.8, the total energy curves do not go above zero, even upon close contact. This indicates that stable chains will form after a threshold magnetic field strength, which is confirmed experimentally. As discussed earlier, the advantage of longer surface DNA is that the grafting density decreases with increasing surface DNA length. Thus longer surface DNA results in less strands per unit area on particle surfaces and weaker repulsion (surface grafting density as low as $\sigma = 3.7 \times 10^4 \; strands/nm^2$ for 40 base surface DNA particles). Another advantage of longer surface DNA is the larger linking area between adjacent particles.

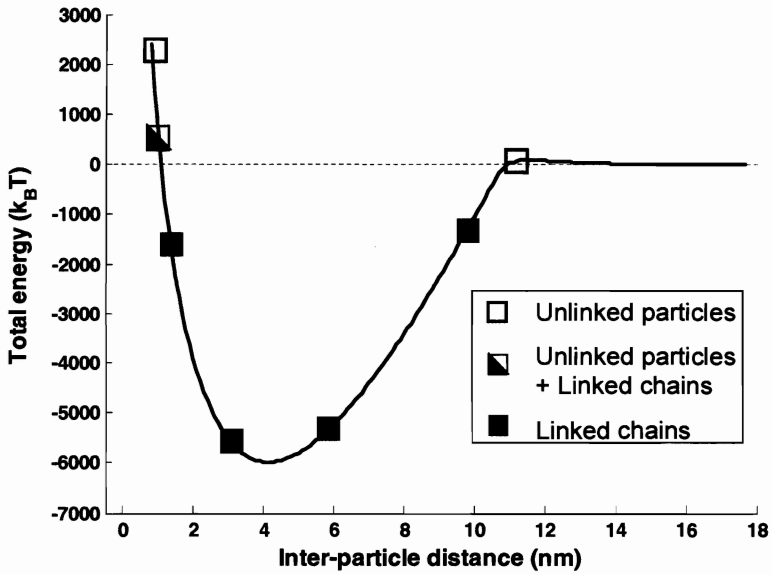

Figure 2.7. a) Total energy landscape for particles grafted with 21-base surface DNA with an average surface DNA grafting density of $\sigma = 64,000\, strands/\mu m^2$. Experimental data points of measured linked particle ratios are placed along the total energy curve at inter-particle distances corresponding to the magnetic field strength applied.

For particles with a surface DNA length greater than 31 bases, the combination of the above factors results in total energy curves to remain negative at all inter-particle distances. Experimentally, when the applied magnetic field strength is larger than 40 Gauss, particles with a surface DNA longer than 31 bases remain linked upon field removal for the surface DNA grafting densities studied. Note that there is an upper limit for spacer DNA length. Beyond this length, the spacer DNA becomes flexible so that the probability of the sticky ends coming into registry is diminished, making DNA bridging difficult.

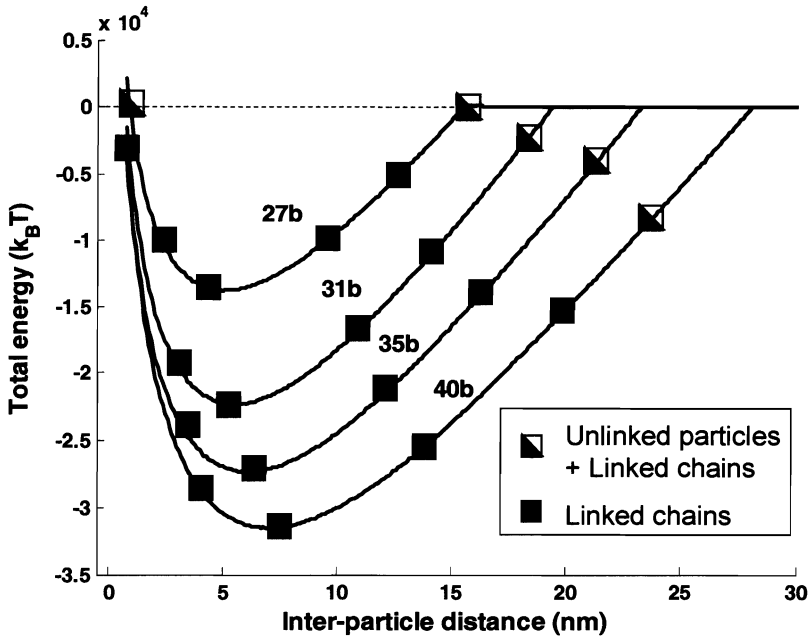

Figure 2.8. Total inter-particle interaction energy plot for systems with 4 different surface DNA lengths with DNA grafting densities of $\sigma = 65,500\ strands/\mu m^2$ for 27 base particles, $\sigma = 60,700\ strands/\mu m^2$ for 31 base particles, $\sigma = 53,500\ strands/\mu m^2$ for 35 base particles, and $\sigma = 36,500\ strands/\mu m^2$ for 40 base particles. Experimental data points of measured linked particle ratios are placed along the total energy curve at inter-particle distances corresponding to the magnetic field strength applied.

2.5. Conclusions

I have investigated the stability of DNA-linked magnetic colloidal chains. Theoretical calculations predict that the total inter-particle free energy curves have a strong dependence on surface DNA length, magnetic field strength applied, and DNA surface

grafting density. A phase diagram generated by experimental results for a variety of field strengths and spacer DNA lengths shows good agreement with the model. This model serves as a useful tool to predict whether one can form stable linked chains under given experimental conditions. By comparing calculated total energy plots with experimental results, maximum stability of DNA-linked paramagnetic chains can be achieved by optimizing the aforementioned parameters. More specifically, it provides a range of magnetic field strengths one can apply to a system for a given surface DNA, surface DNA grafting density σ, and magnetic susceptibility χ of the particles. Our investigation reveals that the particle surface DNA length and coverage as well as the magnetic field strength play key roles on the stability of linked paramagnetic particle chain systems. From here, stable DNA-linked paramagnetic particle chain assemblies can be synthesized and the strength of such assemblies can be tuned. Extending this theory to other cross-linked colloidal systems may prove to be a promising future work, leading to a better understanding of inter-particle interactions between colloids imposed both by external forces and the cross-linking molecule properties. Understanding field directed colloidal assembly can further assist the building of secondary or more sophisticated structures.

2.6. Reference

1. Whitesides, G. M.; Wong, A. P., The intersection of biology and materials science. *Mrs Bulletin* **2006,** 31, (1), 19-27.
2. Ball, P., It all falls into place. *Nature* **2001,** 413, (6857), 667-668.
3. Yin, Y. D.; Lu, Y.; Gates, B.; Xia, Y. N., Template-assisted self-assembly: A practical route to complex aggregates of monodispersed colloids with well-defined sizes, shapes, and structures. *Journal of the American Chemical Society* **2001,** 123, (36), 8718-8729.
4. Biancaniello, P. L.; Kim, A. J.; Crocker, J. C., Colloidal interactions and self-assembly using DNA hybridization. *Physical Review Letters* **2005,** 94, (5).
5. Valignat, M. P.; Theodoly, O.; Crocker, J. C.; Russel, W. B.; Chaikin, P. M., Reversible self-assembly and directed assembly of DNA-linked micrometer-sized colloids. *Proceedings of the National Academy of Sciences of the United States of America* **2005,** 102, (12), 4225-4229.
6. Biancaniello, P. L.; Crocker, J. C.; Hammer, D. A.; Milam, V. T., DNA-mediated phase behavior of microsphere suspensions. *Langmuir* **2007,** 23, (5), 2688-2693.
7. Nykypanchuk, D.; Maye, M. M.; van der Lelie, D.; Gang, O., DNA-based approach for interparticle interaction control. *Langmuir* **2007,** 23, (11), 6305-6314.
8. Nykypanchuk, D.; Maye, M. M.; van der Lelie, D.; Gang, O., DNA-guided crystallization of colloidal nanoparticles. *Nature* **2008,** 451, (7178), 549-552.
9. Xiong, H. M.; van der Lelie, D.; Gang, O., DNA linker-mediated crystallization of nanocolloids. *Journal of the American Chemical Society* **2008,** 130, (8), 2442-2443.
10. Alivisatos, A. P.; Johnsson, K. P.; Peng, X. G.; Wilson, T. E.; Loweth, C. J.; Bruchez, M. P.; Schultz, P. G., Organization of 'nanocrystal molecules' using DNA. *Nature* **1996,** 382, (6592), 609-611.
11. Mirkin, C. A.; Letsinger, R. L.; Mucic, R. C.; Storhoff, J. J., A DNA-based method for rationally assembling nanoparticles into macroscopic materials. *Nature* **1996,** 382, (6592), 607-609.
12. Braun, E.; Eichen, Y.; Sivan, U.; Ben-Yoseph, G., DNA-templated assembly and electrode attachment of a conducting silver wire. *Nature* **1998,** 391, (6669), 775-778.
13. Crocker, J. C., Nanomaterials: Golden handshake. *Nature* **2008,** 451, (7178), 528-529.
14. Jin, R. C.; Wu, G. S.; Li, Z.; Mirkin, C. A.; Schatz, G. C., What controls the melting properties of DNA-linked gold nanoparticle assemblies? *Journal of the American Chemical Society* **2003,** 125, (6), 1643-1654.
15. Cao, Y. W. C.; Jin, R. C.; Mirkin, C. A., Nanoparticles with Raman spectroscopic fingerprints for DNA and RNA detection. *Science* **2002,** 297, (5586), 1536-1540.
16. Milam, V. T.; Hiddessen, A. L.; Crocker, J. C.; Graves, D. J.; Hammer, D. A., DNA-driven assembly of bidisperse, micron-sized colloids. *Langmuir* **2003,** 19, (24), 10317-10323.
17. Biswal, S. L.; Gast, A. P., Mechanics of semiflexible chains formed by poly(ethylene glycol)-linked paramagnetic particles. *Physical Review E* **2003,** 68, (2), 9.
18. Goubault, C.; Jop, P.; Fermigier, M.; Baudry, J.; Bibette, J., Flexible magnetic

filaments as micromechanical sensors. *Physical Review Letters* **2003,** 91, (26), 4.
19. Furst, E. M.; Suzuki, C.; Fermigier, M.; Gast, A. P., Permanently linked monodisperse paramagnetic chains. *Langmuir* **1998,** 14, (26), 7334-7336.
20. Cohen-Tannoudji, L.; Bertrand, E.; Bressy, L.; Goubault, C.; Baudry, J.; Klein, J.; Joanny, J. F.; Bibette, J., Polymer bridging probed by magnetic colloids. *Physical Review Letters* **2005,** 94, (3).
21. Dreyfus, R.; Baudry, J.; Roper, M. L.; Fermigier, M.; Stone, H. A.; Bibette, J., Microscopic artificial swimmers. *Nature* **2005,** 437, (7060), 862-865.
22. Goubault, C.; Leal-Calderon, F.; Viovy, J. L.; Bibette, J., Self-assembled magnetic nanowires made irreversible by polymer bridging. *Langmuir* **2005,** 21, (9), 3725-3729.
23. Koenig, A.; Hebraud, P.; Gosse, C.; Dreyfus, R.; Baudry, J.; Bibette, J., Magnetic force probe for nanoscale biomolecules. *Physical Review Letters* **2005,** 95, (12).
24. Licata, N. A.; Tkachenko, A. V., Statistical mechanics of DNA-mediated colloidal aggregation. *Physical Review E* **2006,** 74, (4).
25. SantaLucia, J., A unified view of polymer, dumbbell, and oligonucleotide DNA nearest-neighbor thermodynamics. *Proceedings of the National Academy of Sciences of the United States of America* **1998,** 95, (4), 1460-1465.
26. Dolan, A. K.; Edwards, S. F., Theory of stabilization of colloids by adsorbed polymer. *Proceedings of the Royal Society of London Series a-Mathematical Physical and Engineering Sciences* **1974,** 337, (1611), 509-516.
27. Whitmore, M. D.; Noolandi, J., Theory of adsorrbed block copolymers.. *Macromolecules* **1990,** 23, (13), 3321-3339.
28. Murat, M.; Grest, G. S., Interaction between grafted polymeric brushes - A molecular dynamics study. *Physical Review Letters* **1989,** 63, (10), 1074-1077.
29. de Gennes, P. G., Conformations of polymers attached to an interface. *Macromolecules* **1980,** 13, (5), 1069-1075.
30. Alexander, S., Adsorption of chain molecules with a polar head A - Scaling description. *Journal De Physique* **1977,** 38, (8), 983-987.
31. Milner S.T., W. T. A. a. C. M. E., The theory of tethered polymer brushes. *Macromolecules* **1988,** 21, 2610.
32. Taunton, H. J.; Toprakcioglu, C.; Fetters, L. J.; Klein, J., Forces between surfaces bearing terminally anchored polymer-chains in good solvents. *Nature* **1988,** 332, (6166), 712-714.
33. de Gennes, P., G., *Scaling Concepts in Polymer Physics*. Cornell University Press: Ithaca, 1979.
34. Milner, S. T., Polymer brushes. *Science* **1991,** 251, (4996), 905-914.
35. Milner, S. T., Compressing polymer brushes - A quantitative comparison of theory and experiment. *Europhysics Letters* **1988,** 7, (8), 695-699.
36. Tinland, B.; Pluen, A.; Sturm, J.; Weill, G., Persistence length of single-stranded DNA. *Macromolecules* **1997,** 30, (19), 5763-5765.
37. Onsager, L., The effects of shape on the interaction of colloidal particles. *Annals of the New York Academy of Sciences* **1949,** 51, (4), 627-659.

Chapter 3

Rigidity control of DNA-linked paramagnetic particle chains

As shown in the previous chapter, I developed a system to create stable linear chains of magnetic colloidal particles linked together using oligonucleotides. These DNA-linked paramagnetic particle chains can be used as "smart" materials for microfluidic applications and as models for studying polymer dynamics. In both cases, the chain rigidity is an important physical parameter. Thus controlling and characterizing rigidity is a crucial parameter for their optimum performance. The bending rigidity, or persistence length, of a chain can be determined by monitoring its thermal fluctuations and performing a Fourier mode analysis of their bending motion. In this chapter, I show that the persistence lengths of the chains can be tuned from 5 μm to 50 mm, which corresponds to a length to persistence length ratio of 0.002 to 10, by changing the length of the DNA used to link adjacent particles from 850 to 15 bases. With this range of persistence lengths, these colloidal chains can be considered to be semiflexible filaments

with worm-like chain (WLC) behavior and are comparable to macro-biopolymers such as microtubules[9,11,12]. Interestingly, from our thermal fluctuation analysis, I observe defects, or kinks, that appear along the chain backbone and undergo axial rotation. I show that, despite the artifacts caused by axial rotation of kinks at short length scales, the bending rigidity of the DNA-linked colloidal particle chains can still be well controlled and characterized at longer length scales, certifying them as promising model systems for semiflexible and rigid polymers. These chains offer a unique method to explore the interplay of thermal fluctuations, external forces, and interactions in semiflexible polymer systems. Additionally, these chains allow for new materials with considerable rigidity, yet are flexible enough to reorganize in response to external stimuli for microfluidic applications.

3.1. Worm-Like Chain Model chains

The bending rigidity of semiflexible filaments has been described well by the worm-like chain model (WLC). This model has been widely used in polymer physics to describe both equilibrium and dynamic properties of filaments that have finite elasticity. The bending rigidity of a WLC is characterized by its persistence length, L_P[4]. It is related to the flexural rigidity, EI, by $L_P = EI/k_BT$[5], where k_BT is the thermal energy. A polymer is denoted as rigid, semiflexible or flexible when the ratio of its contour length to persistence length L/L_P is $<<1$, ~ 1 or $>>1$, respectively. For a linked colloidal particle chain to qualify as a good polymer model, its persistence length has to be measured and

controlled. Measurements have been made previously by utilizing either optical tweezers[6] or magnetic fields[7] to impose small forces on these particle chains to deduce persistence lengths by observing changes in the curvature of a chain. A less intrusive manner to measure the persistence length of these chains is to let Brownian forces bend the chains and then use statistical mechanics calculations on their resulting curvature changes due to thermal fluctuations to extract persistence length values. This method has been widely used in the biophysics community to measure the elasticity of semiflexible polymers such as microtubules[1-3, 8], actin filaments,[1, 3, 9, 10] amyloid filaments,[11, 12] and recently single-wall carbon nanotubes[13]. However, to date, the persistence length of linked colloidal particle chains has not been measured from thermal fluctuations.

3.2. Experimental methods and materials

3.2.1. Particle preparation

DNA-functionalized paramagnetic particles are prepared by coupling streptavidin functionalized polystyrene beads (MyOne, Dynal Biotech, Oslo, Norway) with 3'-primary biotin modified single stranded DNA (ssDNA) oligomers (Integrated DNA Technologies, Coralville, IA). The mean diameter of the particles is 1.07 ± 0.04 m, confirmed by dynamic light scattering and scanning electron microscopy (SEM) measurements. As described in the previous chapter, the surface DNA is composed of two parts, 15-base sequence ("sticky end") at the free end that is complementary to half of the linker DNA, and a poly-thymine sequence ("spacer DNA") that extends the sticky end away from the particle surface. The linker DNA is a symmetric 30-base oligonucleotide designed to hybridize sticky ends from adjacent particle surfaces. Both

surface DNA and linker DNA sequence designs are described in Chapter 2[14]. In this study I vary the "spacer DNA" from 0 to 60 bases. Thus, the total length of ssDNA grafted to the particle surface are 15, 35, 50 and 75 bases, with grafting densities measured to be $5.0\text{x}10^4$, $2.8\text{x}10^4$, $8.0\text{x}10^3$, and $3.5\text{x}10^3$ strands/μm^2, respectively[15].

3.2.2. Chain preparation

The particles are linked in a glass flow cell of size $2cm \times 2cm \times 50\mu m$. Two block magnets are used to generate a uniform magnetic field at the center of the flow cell. Both the DNA-functionalized particles ($1\times10^5\ particles/\mu L$) and the linker DNA ($30\mu M$) are dispersed in phosphate buffer solutions (PBS, 60mM, pH 7.4). They are mixed with equal volume and immediately injected into the flow cell, which is subsequently sealed to prevent evaporation and flow currents. The system is incubated at room temperature for 2 hours before the magnets are removed and video recordings of the chain's Brownian motion are made. The incubation time is long enough to ensure that linking behavior is time independent, and the linker DNA concentration is high enough that the linking behavior is linker-DNA-concentration independent in that neither increasing incubation time nor linker DNA concentration leads to a change in measured persistence length. For any given linked chain, deviations of the particle centroids from the centerline are readily observable to be randomly distributed along the backbone. I denote these deviations as kinks, which are intrinsic short wavelength defects induced by a slight anisotropy of the magnetic material distribution within the particles[16-18].

3.2.3. Video recording and image processing

Upon removal of the magnets, the linked chains begin to have observable curvature fluctuations. I choose one chain of appropriate length (shows observable curvature change and fits within the field of view of the CCD camera, usually 30~80 beads long) to record. This chain is isolated from neighboring chains to ensure negligible hydrodynamic coupling. The thermal curvature fluctuation of the chain is observed using an inverted optical microscope with an $100\times$ oil immersion objective (Olympus IX71, Olympus America Inc., Melville, NY) and recorded using a CCD camera (Orca-HR, Hamamatsu Inc., Sewickley, PA) at 10 frames per second with a 5 ms exposure time for 20 minutes (Figure 3.1a). For each frame, the centroid position of each particle within the chain is obtained (Figure 3.1b) by fitting its intensity profile with a Gaussian distribution after eliminating image noise using boxcar averaging and Gaussian convolution to the whole image[15, 19].

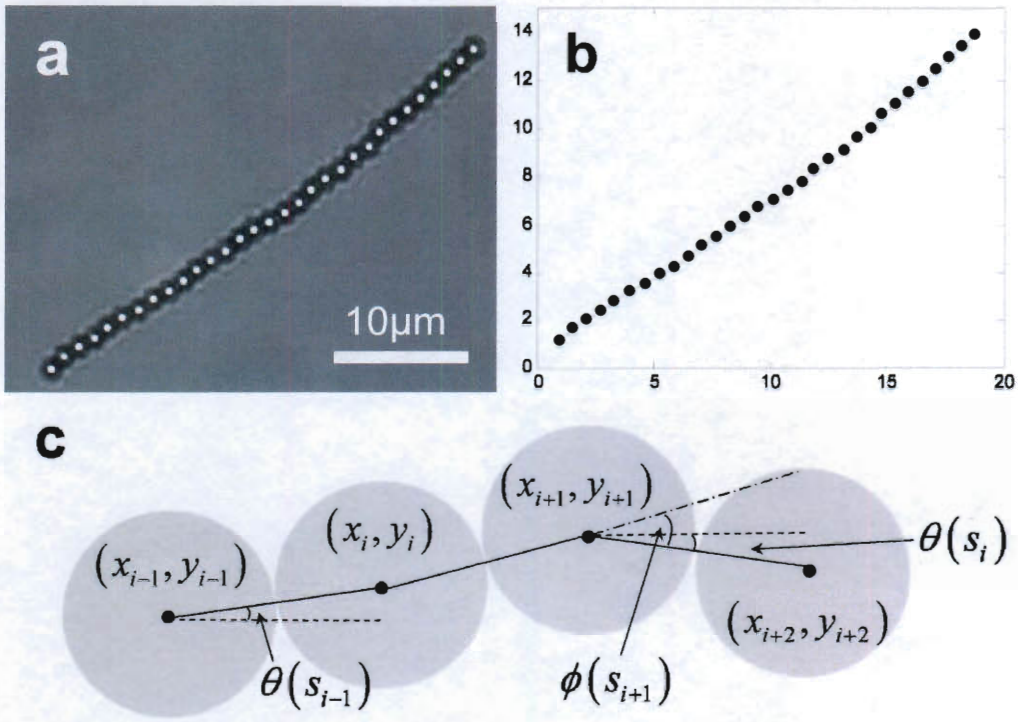

Figure 3.1. Measuring persistence length of a 31-bead DNA-linked chain by tracking thermal fluctuation in curvature. a) Snapshot of a 31-bead DNA-linked chain undergoing Brownian motion. b) Processed centroid positions of the same chain in a. c) Definitions of position coordinates, tangent angle θ(si) and bond angle φ(si) (zero without kink and finite angle with local kink) along the chain.

3.2.4. Fourier mode analysis of curvature from thermal fluctuation

In Fourier mode analysis, the instantaneous curvature of a chain at a given time is decomposed into a series of superimposed Fourier modes,

$$\theta(s) = \sum_{n=0}^{\infty} \theta_n(s) = \sqrt{\frac{2}{L}} \sum_{n=0}^{\infty} a_n \cos(\frac{n\pi s}{L}) \tag{3.1}$$

where L is the contour length of the chain, n is the Fourier mode number, a_n is the amplitude of the nth mode, s is the arc length from a reference point (usually the left end), and the tangent angle $\theta(s)$ is calculated using $\theta(s_i) = \tan^{-1}\left[(y_{i+1} - y_i)/(x_{i+1} - x_i)\right]$ (defined in Figure 3.1c), completely specifies the instantaneous shape of the chain. The bending energy $U = \frac{1}{2} EI \int_0^L \left(\partial\theta/\partial s - \partial\theta_0/\partial s\right)^2 ds$, can be written as a function of Fourier mode amplitudes by differentiating Equation 3. 1 and integrating along the arc length of the chain,

$$U = \frac{1}{2} EI \sum_{n=1}^{\infty} \left(\frac{n\pi}{L}\right)^2 \left(a_n - a_n^0\right)^2 \tag{3.2}$$

where a_n^0 is the intrinsic bending amplitude of the nth mode and EI is the flexural rigidity of the chain. The quadratic dependence of bending energy on bending amplitudes, according to equipartition theorem, results in the average bending energy of each mode equal to $\frac{1}{2} kT$, which leads to the equation:

$$\mathrm{var}(a_n) = \left\langle \left(a_n(t+\Delta t) - a_n(t)\right)^2 \right\rangle_{t,\Delta t \gg \tau_n} = \frac{kT}{EI}\left(\frac{L}{n\pi}\right)^2 \qquad (3.3)$$

where Δt is the lag time between frames, and τ_n is the relaxation time of the n^{th} mode. A long lag time where, $\Delta t >> \tau_n$, ensures that the amplitudes are uncorrelated in the bracket to be averaged and thus makes it equal to the variance of the amplitude. In fact, equipartition also makes the histogram of the amplitudes of each mode a Gaussian distribution. Thus one can also obtain the variance of amplitudes by fitting the histograms to a Gaussian profile.

3.2.5. Calculating persistence length

The thermal bending rigidity of a microscopic chain can also be discussed in terms of persistence length. Persistence length is the distance beyond which the tangent angles of two points along the chain become uncorrelated. In other words, it is the length scale at which a chain exhibits significant bending. By relating Equation 3.3 and $L_P = EI/kT$, one obtains the expression to calculate persistence length from Fourier mode analysis,

$$L_P = \frac{L^2}{n^2\pi^2\,\mathrm{var}(a_n)} \qquad (3.4)$$

From this equation I see that the amplitude variance of each mode provides an independent prediction of the overall persistence length of the chain, given the fact that the chain has uniform rigidity at least on the length scale of measurement. This also serves as a consistency check of the mode analysis method.

3.2.6. Error estimate in amplitude

Image noise causes random errors in the measurements of particle centroid positions, which result in systematic errors in the estimate of amplitude variances. This overestimation of amplitude variances, from Equation 3.4, leads to underestimation of the persistence length. The systematic error calculation is detailed elsewhere, but it obeys the simple form,

$$\mathrm{var}(a_n)^{noise} = \frac{4}{L}\left\langle \varepsilon_{xy}^2 \right\rangle \left[1 + (N-1)\sin^2\left(\frac{n\pi}{2N}\right) \right] \tag{3.5}$$

where $\left\langle \varepsilon_{xy}^2 \right\rangle$ is the standard error of centroid position measurements (previously determined to be on the order of 4 nm for chains formed from 1μm particle chains[15]), N is the number of beads within the chain, and $\mathrm{var}(a_n)^{noise}$ is the resulting error of the amplitude variance, which is always positive. This error is plotted as the noise floor in the amplitude variance verses mode number diagram, shown in Figure 3.2.

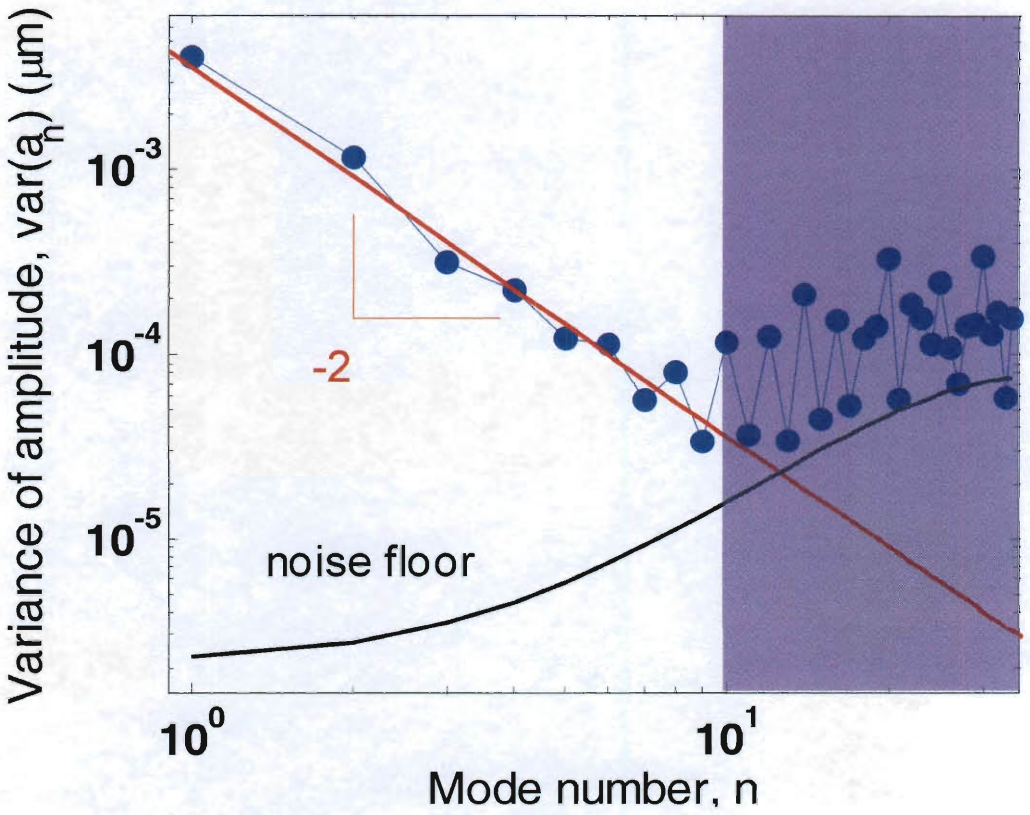

Figure 3.2. Variance of Fourier amplitude versus mode number plot for a 36-bead chain with 35-base surface DNA-coated particles. Red line is the best fit for the first seven modes. Noise floor is calculated using Equation 3.5. Shaded area is where the bending length scale is shorter than 3μm, and the variances are increasingly affected by axial rotation of intrinsic bends (kinks) in the chain.

3.2.7. Brownian dynamics simulation

In order to better understand the bending dynamics of DNA-linked particle chains observed experimentally, I have developed a Brownian dynamics (BD) simulation algorithm for a single free-draining chain (MATLAB codes in Appendix A). This

simulation allows us to study the effects of both kinks in a chain and axial rotation. I examine the consequences of these effects and relate the behavior of our colloidal chains to WLC.

I study three types of model chains in our BD simulation: Type I - a 2-D straight chain without kinks, whose lowest energy configuration is a straight line; Type II - a 2-D "zigzag" kinked chain with intrinsic bond angles $\phi_0(s_i) = -\phi_0(s_{i+1})$, where $i = 1, 2, ..., N-1$ and a chain that does not exhibit axial rotation; and Type III- a "zigzag" kinked chain of the same lowest energy configuration as Type II with a torsional force constant the same as its bending force constant[20]. This Type III chain is allowed to diffuse in 3-D space, but also includes the buoyancy force and electrostatic force from substrate to mimic the experimental conditions. Note, this Type III chain does rotate axially.

The equation of motion that describes the dynamics of each magnetic bead within a linked chain is,

$$m_i \frac{d^2\mathbf{r}_i}{dt^2} = \mathbf{F}_i^{bend} + \mathbf{F}_i^{tors} + \mathbf{F}_i^{constr} + \mathbf{F}_i^{metric} + \mathbf{F}_i^{hydro} + \mathbf{F}_i^{Brown} + \mathbf{F}_i^{grav} + \mathbf{F}_i^{ele} \qquad (3.6)$$

where for the i^{th} bead, m_i is the mass of the i^{th} bead (the left-hand-side inertia term is negligible compared with right-hand-side terms in the case of low Reynolds number), $\mathbf{r}_i$

is the position, $\mathbf{F}_i^{bend} = -\partial U/\partial \mathbf{r}_i$ is the worm-like chain bending force[21] with bending energy $U = \frac{1}{2} EI \int_0^L (\partial\theta/\partial s - \partial\theta_0/\partial s)^2 \, ds$, and $\partial\theta_0/\partial s = \partial\phi_0/\partial s$ where ϕ_0 is the bond angle of the local kink, $\mathbf{F}_i^{tors}$ is the torsional force that prevents twist in the case of Type III chain, $\mathbf{F}_i^{constr}$ is the constraint force used to keep the distance between adjacent beads constant, $\mathbf{F}_i^{metric}$ is the metric pseudo-potential forces required in simulations of chains with constrained bond lengths to mimic the behavior of infinitely stiff bead-spring chains[22], $\mathbf{F}_i^{hydro}$ is the hydrodynamic drag force, $\mathbf{F}_i^{Brown}$ is the stochastic Brownian force, $\mathbf{F}_i^{grav}$ is the buoyancy force of a magnetic bead (density ~1.6g/cm^3) dispersed in water, $\mathbf{F}_i^{ele}$ is the electrostatic force between a bead and the negatively charged glass substrate. Note that $\mathbf{F}_i^{tors}$, $\mathbf{F}_i^{grav}$ and $\mathbf{F}_i^{ele}$ are only used for the Type III chain. Since our system is at low Reynolds number flow, the mass of the bead in Equation 3.6 is neglected due to being in an inertialess regime.

The widely used BD algorithm proposed by Ermak and McCammon[23] is applied. In this algorithm, the current position $\mathbf{r}_{(n)}$ ($3N$ vector) of the beads is moved to the next position $\mathbf{r}_{(n+1)}$ according to

$$\mathbf{r}_{(n+1)} = \mathbf{r}_{(n)} + \frac{\Delta t}{k_B T} \mathbf{D}_{(n)} \mathbf{F}_{(n)} + \xi_{(n)} \tag{3.7}$$

where $\mathbf{F}_{(n)}$ is the collective vector of internal and external (except Brownian and hydrodynamic) forces acting on a bead $\mathbf{F}_{(n)} = \mathbf{F}_i^{bend} + \mathbf{F}_i^{tors} + \mathbf{F}_i^{constr} + \mathbf{F}_i^{met} + \mathbf{F}_i^{grav} + \mathbf{F}_i^{ele}$, $\xi_{(n)}$ is a random force generated at each time step from a Gaussian distribution with zero mean and variance $\left\langle \xi_{(n)} \xi_{(n')} \right\rangle = 2\mathbf{D}_{(n)} \Delta t \delta_{nn'}$, where Δt is the time step and $\delta_{nn'}$ is the Kronecker delta, and $\mathbf{D}_{(n)}$ is the 3×3 Rotne-Prager translational diffusion matrix[24] used to account for hydrodynamic interactions between all beads.

For the constraint force, I use the LINCS algorithm proposed by Hess et al[25] on the inextensible chains, which leads to the final expression for computing the motion,

$$\mathbf{r}_{(n+1)} = \left(\mathbf{I} - \mathbf{T}_{(n)}\mathbf{B}_{(n)}\right)\left(\mathbf{r}_{(n)} + \frac{\Delta t}{k_B T}\mathbf{D}_{(n)}\mathbf{F}_{(n)} + \xi_{(n)}\right) + \mathbf{T}_{(n)}\mathbf{d} \qquad (3.8)$$

where $\mathbf{T}_{(n)} = \mathbf{D}_{(n)}\mathbf{B}_{(n)}^T\left(\mathbf{B}_{(n)}\mathbf{D}_{(n)}\mathbf{B}_{(n)}^T\right)^{-1}$, $\mathbf{B}_{(n)}$ is a bi-diagonal $(N-1)\times 3N$ matrix containing the gradients of the inter-bead distance constraints and $\mathbf{d}$ is a vector containing the distances between adjacent beads.

Given the initial positions of each bead in the chain, forces and the diffusion tensor can be calculated. Then, by inserting a time step ($\sim 1\times10^{-6}\,s$) into Equation 3.8, positions for each bead in the chain at the next time step are solved. Evolution of bead positions with

time can be obtained by iterating the above steps, and all the position-based properties can be computed and compared with experimental data.

3.3. Results and discussion

The persistence length of DNA-linked colloidal particle chains is measured using Fourier mode analysis of their curvature change due to thermal fluctuations. The time-averaged Fourier amplitude of each mode provides an independent estimate for the persistence length at its corresponding length scale (approximately contour length divided by mode number). For a homogeneous filament (continuum limit), the persistence length over all length scales is the same, which provides a means to check internal consistency of the measurement. Consequently according to Equation 3.3, if the variances of Fourier mode amplitudes $\mathrm{var}(a_n)$ are plotted against mode number n, the data should have -2 power-law decay. In Figure 3.2, I show a typical plot of amplitude variance versus mode number for DNA-linked colloidal chains, where data for the first 8~9 modes follow the expected inverse squared dependence. At higher modes, the data begin to exhibit periodical oscillation and systematic deviation. The deviation at these higher modes can be partially accounted for by the errors in the bead position measurements resulting from noise in the images and pixelation[1-3, 13, 19], as the noise floor computed using Equation 3.5 sets the lower bound of data points in the higher mode region. As the mode increases, the expected variance of Fourier amplitude becomes smaller and more noise-dominated; the signal-to-noise ratios approach zero for data points close to the noise floor. However, this

does not explain the amplified periodic oscillation and significant deviations of some points at higher modes. I argue that these effects are caused both by intrinsic kinks and their rotation around the long axis of the chain. In the following sub-sections, I first show the evidence of kinks and axial rotation and then how they could consequently affect the Fourier mode amplitude variances.

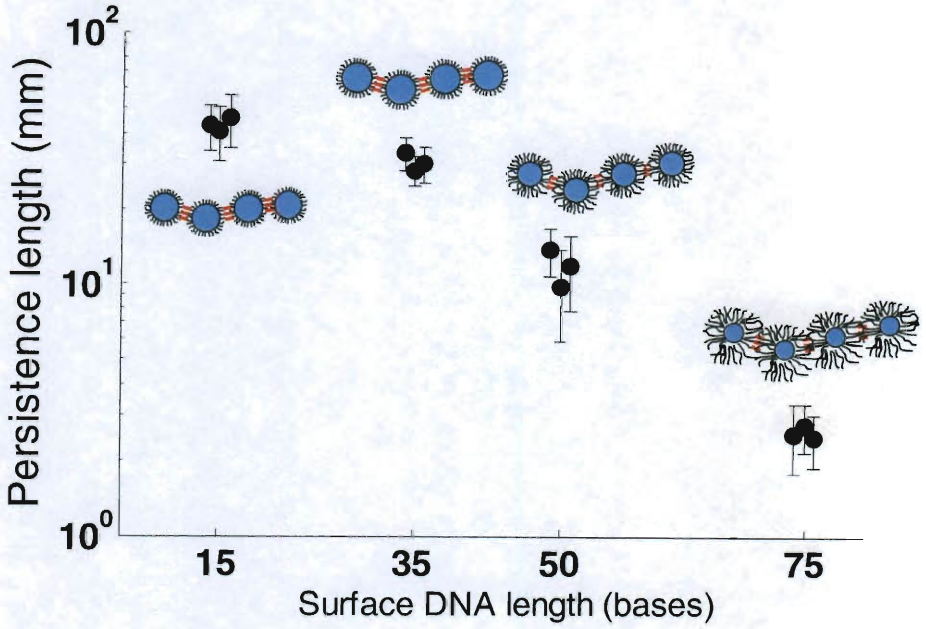

Figure 3.3. Summary of overall persistence length as a function of particle surface DNA length. Error bars are standard deviations of persistence lengths computed using different modes. Schematics next to each data point show (not to scale) the geometry of increasing particle surface DNA length (black filaments) and unchanged linker DNA length (red).

3.3.1. Persistence length as a function of surface DNA

For each of the chains assembled from particles with different surface DNA lengths, I first calculate the transition length scale and mode number using Fourier mode amplitudes as in Figure 3.2, 4, and 5. Then I use Equation 3.4 to compute persistence lengths from Fourier modes whose mode numbers are smaller than the critical mode number of the chain. The mean is taken to be the persistence length of the chain and the standard deviation the error. This procedure makes sure that the measured persistence lengths are purely from bending and does not include axial rotation of kinks.

In Figure 3.3, the persistence lengths of DNA-linked colloidal particle chains are plotted as a function of length of the DNA grafted on the particles. The persistence length ranges from 1 mm to 50 mm (L/L_P from 0.002 to 0.1) for surface DNA lengths of 15 to 75 bases, decreasing with increasing surface DNA length. A similar linker-length effect has been reported previously[3] using a polyethylene glycol linker system. Intuitive interpretation of this effect can be made by analogy with varying the length of connecting springs in the classical bead-spring model (e.g. the chain rigidity decreases with increase of spring length, and vice versa). I have shown that the bending elasticity of these colloidal particle chains can be carefully tuned to yield chains with a bending rigidity comparable to that of microtubules measured *in vitro*[1-3, 8, 26].

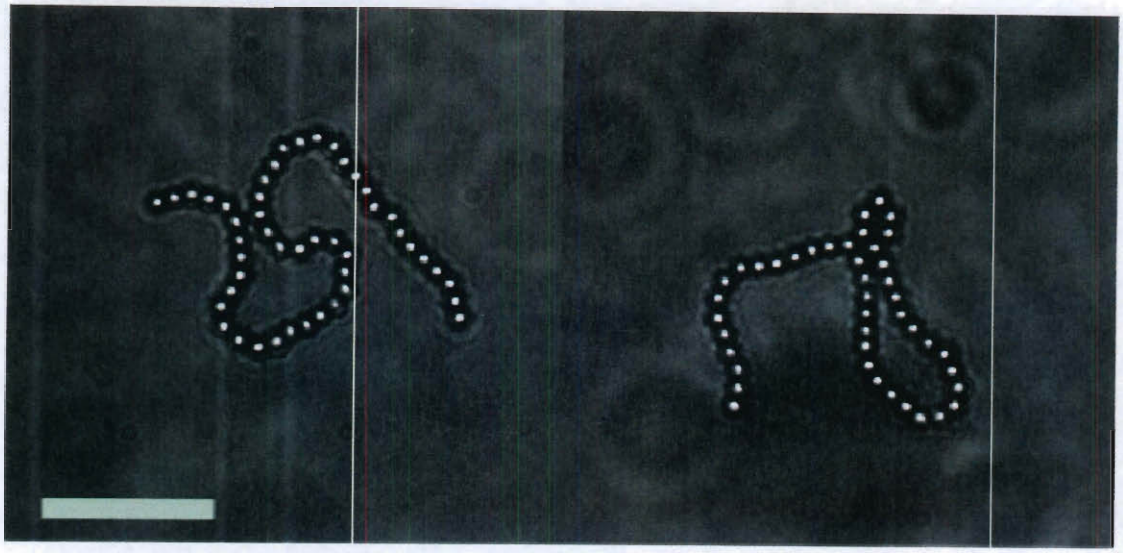

Figure 3.4. Representative configurations of 850bp double-stranded DNA (dsDNA) linked magnetic particle chains. The images are taken 5 minutes after magnetic field is taken off. The persistence length of the chains is measured to be ~5μm.

To make chains in the semiflexible to flexible region, one way is to increase the length of the springs. In my experiments, a 850bp dsDNA (both ends terminated with biotin groups) is used to link streptavidin coated Dynabeads. The use of double-stranded DNA is because they can be manufactured much longer (850bp dsDNA has a contour length of 290 nm while that of the 75-base ssDNA is 50nm), though their intrinsic stiffness is greater (persistence length of dsDNA is ~50nm while that of ssDNA is ~3nm). And the resulting chains have consistent persistence length of ~5μm. It is easily seen from their much coiled equilibrium configurations in Figure 3.4 that their persistence lengths are comparable to their contour lengths. Note that changing particle surface DNA length is not the only way to tune the persistence length of the chain. Alternative methods

include changing surface DNA grafting density, linker DNA length and concentration, temperature, salt concentration, particle spacing, particle size, etc. Our preliminary results show that by reducing the linker DNA concentration to ~1 nM, it is possible to make chains of persistence length $\sim 100\mu m$ ($L/L_P \sim 1.8$), close to that of actin filaments[1, 3, 9, 10]. These results make our colloidal chains promising model systems with which to study biopolymers.

3.3.2. Existence of kinks and their axial rotation

The kinks are directly observed as noticeable deviations of particle positions from a smooth curve in any snapshot in the video (Figure 3.5a). One might argue that this could also be instantaneous bending due to Brownian motion. To experimentally prove the existence of kinks I overlay the bond angles $\phi(s_i)$ of a 36-bead chain for all time frames as a function of positions on the chain (bond angle number from the left) in Figure 3.5b. The absolute values of these bond angles are much larger (10~20 degrees) than they should have been if they were the result of thermal bending (±1.5 degree for a chain with a persistence length of 30 mm, estimated from lower mode number data in Figure 3.2). Additionally, the means of the distributions for most bond angles deviate from zero, indicating that the equilibrium shape of the chain is not straight. Both observations rule out the possibility that the observed large bond angle values are solely due to thermal fluctuations, and support the existence of kinks within a chain.

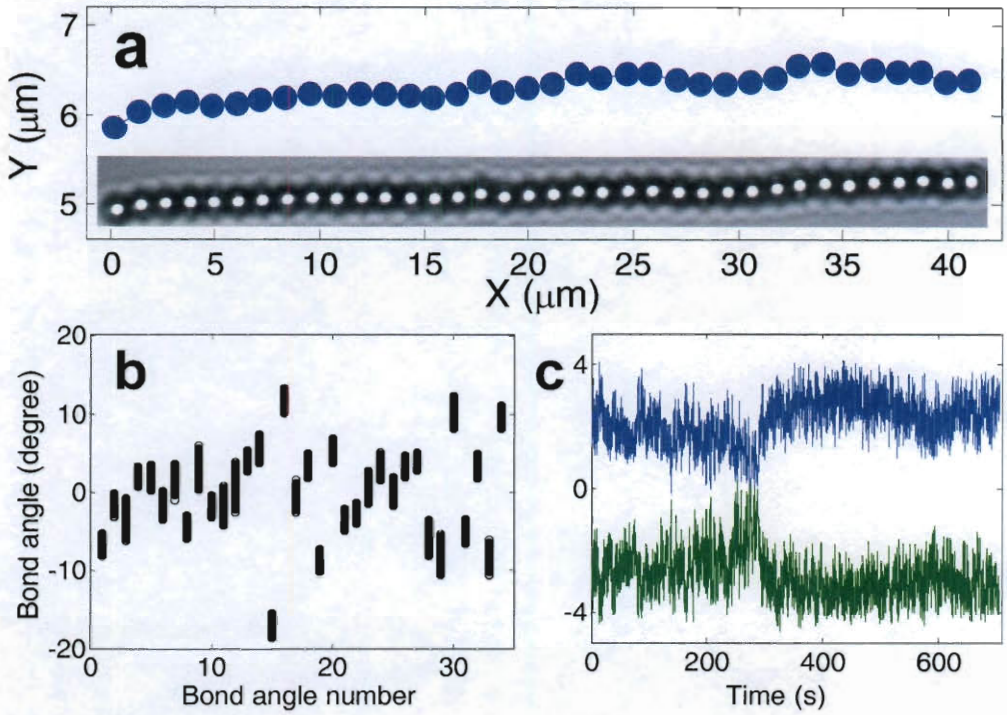

Figure 3.5. Evidence of axial rotational diffusion. a) A snapshot (inset) of the shape of the chain analyzed in Figure 3.2. Note that the Y-axis is scaled differently from the X-axis to demonstrate kinks. b) Bond angles $\varphi(s_i)$ along the backbone of the same chain. Deviations of mean angles from zero indicate the prevailing existence of kinks; and large variances of angles (5~10 degrees) imply dynamics other than bending. c) Plot of the 5th (blue) and 6th (green) bond angles as a function of time. The noticeable correlation (correlation coefficient 0.95) between them provides evidence of axial rotational diffusion.

I further argue that there exists rotational Brownian motion of the chain along its long axis that is revealed by the motion of kinks. Note that the bond angle distributions in Figure 3.5b is 5~10 degrees, which is much larger than the expected ±1.5 degree bond

angle variation for a typical chain with a persistence length of 30 mm. The significant correlation of adjacent bond angles in Figure 3.5c further indicates there are collective motions of these kinks resulting from axial rotation of the entire chain. At short time scales (~10 s), the bond angles exhibit a noisy pattern with a band width of ~1.5 degrees, as the bending relaxation time at the length scale of three particles (~1 ms) is much smaller than the observation time interval (0.1 s). At longer time scales (~100 s), however, both bond angles display correlated shifts, whose time scale is comparable to the axial rotational diffusion of a rod[26-28]. The above evidence, put together, strongly suggests the existence of kinks and their axial rotation in a chain.

3.3.3. Bending versus axial rotation of kinks

I analyze the consequence of the coupling between the bending dynamics of our DNA-linked colloidal particle chains and the axial rotation of the kinks, and show how they affect our persistence length measurements.

The artifacts in the bending dynamics of a chain are caused by neither kinks nor axial rotation alone[1, 2] (Figure 3.6), but by the combination of the two. Axial rotation of kinks would in theory introduce cross-correlations between affected Fourier modes[1]. To investigate which modes are affected, I calculated the covariance matrix of the Fourier mode amplitudes (Figure 3.6a) of the same 36-bead chain as described in Figure 3.2. Each matrix element C_{ij} represents the correlation coefficient of Fourier amplitudes of the i^{th} mode and the j^{th} mode. No statistically significant correlation is found either among the first four modes or between any of these modes with any higher modes. As

mode number increases, cross-correlations become increasingly significant. This is verified by comparing with the covariance matrix of a BD simulated chain with kinks (Type III, $\phi_0(s_i) = -\phi_0(s_{i+1}) = 6^o$), which displays similar patterns (Figure 3.6d). BD simulations also show that kinks or axial rotation alone do not result in significant cross-correlations (Figure 3.6b), even with different intrinsic bond angles (Figure 3.6c), because the change of a chain's curvature is truly represented in the 2-D images. This indicates that the Fourier mode amplitudes are only affected by axial rotation of kinks at higher bending modes, or shorter length scales. This makes sense because even though axial rotation of kinks induces large short length scale deviations of bond angles and tangent angles, based on which Fourier modes are computed, they get averaged out over a longer distance due to the random nature of the kink arrangement.

It is reasonable to ask the question, "What is the critical length scale at which the transition takes place?" To estimate the transition length scale, I make use of the Cosine Correlation Function (CCF)[9, 10, 20],

$$\left\langle \cos\left[\phi(s_i + \Delta L) - \phi(s_i)\right]\right\rangle_{s_i,t} = \exp(-\frac{\Delta L}{2L_P}) \qquad (3.9)$$

where s_i is the arc length of the i^{th} particle from the left and ΔL is the distance between two points along the backbone of the chain. In Equation 3.9, the bracket has been widely used to represent the time average, but here I use it to compute first the ensemble average

of $\cos\left[\phi(s_i+\Delta L)-\phi(s_i)\right]$ sampled over all possible two-point pairs that are of distances ΔL apart, and then the time average of the ensemble average.

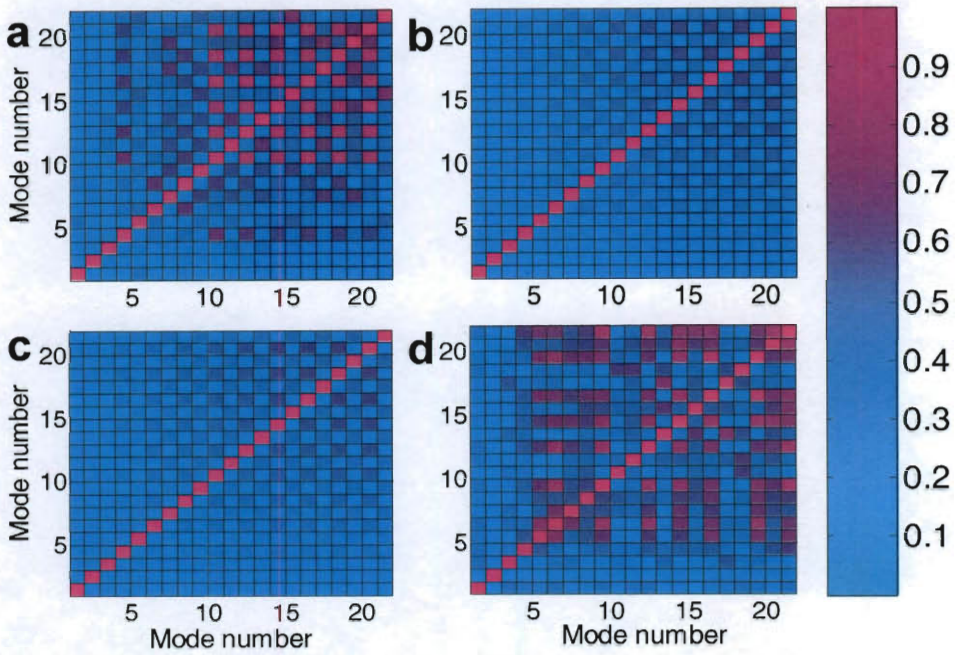

Figure 3.6. Covariance matrices of Fourier mode amplitudes obtained from a) the same 36-bead chain analyzed in Figure 3.2 (experimental data), b) simulated 24-bead straight chain without intrinsic kink (Type I), c) a simulated 24-bead 2D chain with intrinsic kinks (Type II, $\phi_0(s_i) = -\phi_0(s_{i+1}) = 6^o, 12^o, 24^o$, same result), d) a simulated 24-bead chain with kinks and axial rotation (Type III, $\phi_0(s_i) = -\phi_0(s_{i+1}) = 6^o$). The color in each box (matrix element C_{ij}) represents the correlation coefficient of Fourier amplitudes of the i^{th} mode and the j^{th} mode. This matrix is made to be symmetric, and the values of the diagonal elements are assigned the value 1 for better contrast and visualization.

Calculated this way, the $\left\langle \cos\left[\phi(s_i+\Delta L)-\phi(s_i)\right]\right\rangle_{s_i,t}$ versus ΔL profile of an ideal WLC in a log-linear plot should still assume a straight line shape with a slope of $-1/2L_P$, and any deviation implies imperfection. In Figure 3.7, systematic deviations are seen at length scales of 3 μm and 5 μm for chains assembled with either 35-base or 15-base surface DNA particles, respectively. It is the coupling of axial rotation of the kinks with bending that decreases the correlations between tangent angle differences at short length scales. The apparent variation of the difference between two tangent angles is related to the combination of bending energy, which stores instantaneous thermal energy and induce correlations, and the axial rotation of kinks, which is not associated with bending energy and does not necessarily induce correlation. The critical length scale calculated using the CCF method is 3~5μm for the 12 chains analyzed in this paper. This means that for a typical chain of length $40\mu m$, the transition occurs at the 8th~11th mode, which is in agreement with observations in both Figure 3.2 and Figure 3.6.

I conclude from the above analysis that there are two distinct regimes in the dynamics of DNA-linked colloidal particle chains that are separated by a length scale of 3~5μm. Above this length scale (small mode number), bending dominates and Fourier modes match behaviors predicted by WLC theory. Below this length scale (larger mode number), axial rotation of kinks dominates and causes artifacts.

3.4. Conclusions

In this chapter it is shown that DNA-linked colloidal particle chain mimic the behavior of linear semiflexible polymers and can therefore be thought of as a WLC. Using Fourier mode analysis to analyze the curvature fluctuations of these chains, I show that their persistence lengths can be finely tuned in the range of 5μm~50 mm by changing the particle surface DNA length from 850bp to 15 bases. It is found that both static and dynamic properties of our colloidal particle chains match well with WLC theory at length scales larger than 3~5μm, while at shorter length scales, they systematically deviate from theory due to coupling between transverse bending and axial rotation of intrinsic kinks. With careful analysis to account for this artifact, I show that our DNA-linked colloidal particle chain bending rigidity can be well controlled in a wide range that is useful both in being a model system for semiflexible polymer studies and other applications.

3.5. Reference

1. Gittes, F.; Mickey, B.; Nettleton, J.; Howard, J., Flexual rigidity of mircortubules and actin-filaments measured from thermal fluctuations in shape. *Journal of Cell Biology* **1993,** 120, (4), 923-934.
2. Janson, M. E.; Dogterom, M., A bending mode analysis for growing microtubules: Evidence for a velocity-dependent rigidity. *Biophysical Journal* **2004,** 87, (4), 2723-2736.
3. Brangwynne, C. P.; Koenderink, G. H.; Barry, E.; Dogic, Z.; MacKintosh, F. C.; Weitz, D. A., Bending dynamics of fluctuating biopolymers probed by automated high-resolution filament tracking. *Biophysical Journal* **2007,** 93, (1), 346-359.
4. Aragon, S. R.; Pecora, R., Dynamics of wormlike chains. *Macromolecules* **1985,** 18, (10), 1868-1875.
5. Yamakawa, H., *Modern Theory of Polymer Solutions*. Harper and Row: New York, 1971.
6. Biswal, S. L.; Gast, A. P., Mechanics of semiflexible chains formed by poly(ethylene glycol)-linked paramagnetic particles. *Physical Review E* **2003,** 68, (2), 021402.
7. Goubault, C.; Jop, P.; Fermigier, M.; Baudry, J.; Bertrand, E.; Bibette, J., Flexible magnetic filaments as micromechanical sensors. *Physical Review Letters* **2003,** 91, (26), 260802.
8. Mickey, B.; Howard, J., Rigidity of microtubules is increased by stabilizing agents. *Journal of Cell Biology* **1995,** 130, (4), 909-917.
9. Ott, A.; Magnasco, M.; Simon, A.; Libchaber, A., Measurement of the persistence length of polymerized actin using fluorescence microscopy. *Physical Review E* **1993,** 48, (3), R1642-R1645.
10. Isambert, H.; Venier, P.; Maggs, A. C.; Fattoum, A.; Kassab, R.; Pantaloni, D.; Carlier, M. F., Flexibility of actin-filaments derived from thermal fluctuations - Effect of bound nucleotide, phalloidin, and muscle regulatory proteins. *Journal of Biological Chemistry* **1995,** 270, (19), 11437-11444.
11. Knowles, T. P. J.; Smith, J. F.; Craig, A.; Dobson, C. M.; Welland, M. E., Spatial persistence of angular correlations in amyloid fibrils. *Physical Review Letters* **2006,** 96, 238301.
12. Knowles, T. P.; Fitzpatrick, A. W.; Meehan, S.; Mott, H. R.; Vendruscolo, M.; Dobson, C. M.; Welland, M. E., Role of intermolecular forces in defining material properties of protein nanofibrils. *Science* **2007,** 318, (5858), 1900-1903.
13. Fakhri, N.; Tsyboulski, D. A.; Cognet, L.; Weisman, R. B.; Pasquali, M., Diameter-dependent bending dynamics of single-walled carbon nanotubes in liquids. *Proceedings of the National Academy of Sciences of the United States of America* **2009,** 106, (34), 14219-14223.
14. Li, D. C.; Rogers, J.; Biswal, S. L., Probing the Stability of Magnetically Assembled DNA-Linked Colloidal Chains. *Langmuir* **2009,** 25, (16), 8944-8950.
15. Li, D. C.; N., L. C.; Biswal, S. L., Measuring short-range repulsive forces by imaging directed magnetic-particle assembly. *Soft Matter* **2009**, DOI:10.1039/b917675f.

16. Fonnum, G.; Johansson, C.; Molteberg, A.; Morup, S.; Aksnes, E., Characterisation of Dynabeads (R) by magnetization measurements and Mossbauer spectroscopy. *Journal of Magnetism and Magnetic Materials* **2005,** 293, (1), 41-47.
17. Fannin, P. C.; Cohen-Tannoudji, L.; Bertrand, E.; Giannitsis, A. T.; Mac Oireachtaigh, C.; Bibette, J., Investigation of the complex susceptibility of magnetic beads containing maghemite nanoparticles. *Journal of Magnetism and Magnetic Materials* **2006,** 303, (1), 147-152.
18. Janssen, X. J. A.; Schellekens, A. J.; van Ommering, K.; van Ijzendoorn, L. J.; Prins, M. W. J., Controlled torque on superparamagnetic beads for functional biosensors. *Biosensors & Bioelectronics* **2009,** 24, (7), 1937-1941.
19. Crocker, J. C.; Grier, D. G., Methods of digital video microscopy for colloidal studies. *Journal of Colloid and Interface Science* **1996,** 179, (1), 298-310.
20. L. D. Landau; Lifshitz, E. M., *Theory of Elasticity*. 3rd ed.; Pergamon Press: Oxford, 1986.
21. Allison, S. A., Brownian dynamics simulation of wormlike chains - Fluorescence depolarization and depolarized light-scattering. *Macromolecules* **1986,** 19, (1), 118-124.
22. Pasquali, M.; Morse, D. C., An efficient algorithm for metric correction forces in simulations of linear polymers with constrained bond lengths. *Journal of Chemical Physics* **2002,** 116, (5), 1834-1838.
23. Ermak, D. L.; McCammon, J. A., Brownian dynamics with hydrodynamic interactions. *Journal of Chemical Physics* **1978,** 69, (4), 1352-1360.
24. Kratky, O.; Porod, G., Rontgenuntersuchung geloster fadenmolekule. *Recueil Des Travaux Chimiques Des Pays-Bas-Journal of the Royal Netherlands Chemical Society* **1949,** 68, (12), 1106-1122.
25. Hess, B.; Bekker, H.; Berendsen, H. J. C.; Fraaije, J., LINCS: A linear constraint solver for molecular simulations. *Journal of Computational Chemistry* **1997,** 18, (12), 1463-1472.
26. Howard, J., *Mechanics of Motor Proteins and the Cytoskeleton.* Sinauer Associates, Inc.: Sunderland, Massachusetts, 2001.
27. Brenner, H., Effect of finite boundaries on the Stokes resistance of an arbitrary particle. *Journal of Fluid Mechanics* **1962,** 12, (1), 35-48.
28. Hunt, A. J.; Gittes, F.; Howard, J., The force exterted by a single kinesin on molecule against a viscous load. *Biophysical Journal* **1994,** 67, (2), 766-781.

Chapter 4

DNA-linked paramagnetic chains as a model system for semiflexible and rigid polymers chains

In this chapter, I demonstrate that DNA-linked paramagnetic colloidal chains with a wide span of bending rigidity can serve as an ideal model system for studying the dynamics of polymers. In particular, I show that the bending relaxation dynamics of semiflexible chains and the axial rotational diffusion of rigid chains can be measured precisely, which is difficult for their molecular analogs. Bending relaxation and axial rotational diffusion of rod-like polymers are important in processes like microtubule filament sliding and flagella beating. By imaging the motion of beads and small kinks along the backbone of chains of DNA-linked colloids, I produce a direct and systematic measurement of bending relaxation time scales and axial rotational diffusivity of chains both in bulk solution and near a wall. The results agree well with slender-body hydrodynamics theory.

Our system and measurements provide insights into fundamental bending relaxation and axial diffusion processes of slender objects, which encompass a wide range of entities including biological filaments and linear polymer chains.

4.1. Introduction to dynamics of slender objects

Unlike spheres, highly anisotropic objects diffuse in a complex manner, particularly so if they are flexible. The combined effects of their shape anisotropy, their internal degrees of freedom, and their environment greatly influence their behavior. Some of these dynamical effects are now being understood, like the strong coupling between translational diffusion and transverse rotation (usually simply termed rotation)[1] and enhanced transverse rotational diffusion of slightly flexible rods in crowded environments[2]. Despite its crucial importance in the phase separation and formation of liquid crystals [3] and in biological processes such as lipid bilayer dynamics[4] and microtubule sliding[5, 6], rotational diffusion around the long axis (axial rotation) of rod-like molecules and colloids is still poorly characterized and not understood. Direct measurement of axial rotation is challenging because most of the electro-optical properties of cylindrical macromolecules are also axisymmetric[7]. NMR relaxation[4], fluorescence anisotropy decay[8], and 3D-tracking of attached quantum dots [6, 9] have been used to measure the axial rotation of rod-like molecules. The first two techniques measure the ensemble average properties and are model dependent; the third lacks sufficient accuracy to capture diffusion.

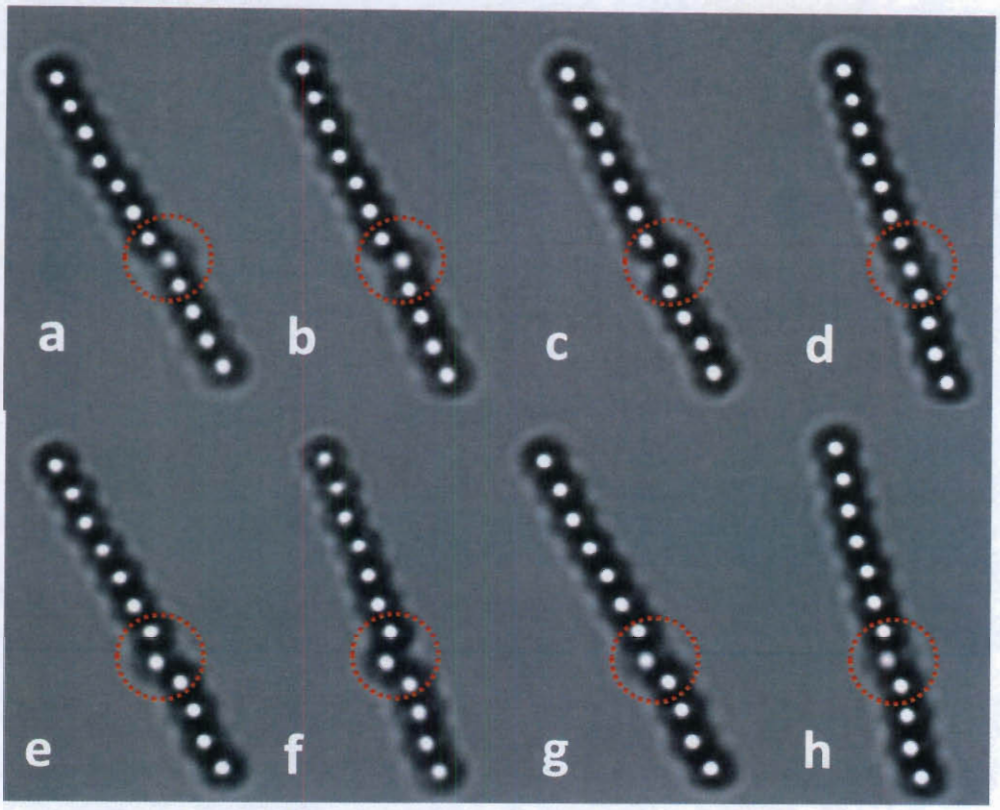

Figure 4.1. Snapshots of a 12-bead rigid DNA-linked chain under Brownian motion in aqueous solution near the bottom substrate. The snapshots a~h are taken 10 seconds apart and the red dashed circles are highlighting the kink formed by the 7^{th}, 8^{th} and 9^{th} bead from the left. The unusual large size ($\phi \approx 75^{o}$) of this kink is only for demonstration whereas the kinks used to measure the axial rotational diffusivities in this chapter are much smaller than this ($14^{o} \leq \phi \leq 25^{o}$).

Recently developed rod-like colloidal model systems[8-11] can be visualized accurately in real time and space and have tunable length and stiffness. Their axial symmetry can be broken simply, as shown by the recent observation of the axial rotation of a rod-like

tetramer along its long axis[10]. In this chapter, I present a systematic study of bending relaxation dynamics of semiflexible slender rods and axial rotational diffusion of rigid slender rods by directly observing with high accuracy the dynamics of asymmetric DNA-linked magnetic colloidal particles. This technique would allow us to probe complex dynamics behavior of rod-like polymers.

Axial rotational diffusion of elongated colloids was reported in 1827 by Robert Brown in the first report on thermal (now called Brownian) motion: "oval particles … their motion consisting in turning usually on their longer axis, and then often appearing to be flattened."[12] Brown's observation relied on the slight asymmetry of arsenic trioxide flakes. The same symmetry breaking principle is used in our experiments, but the measurements are quantitative with high precision. The colloidal rods consist of DNA-grafted paramagnetic particles aligned by a magnetic field and connected by linker DNA strands through hybridization[11, 13]. The axial rotation of these rods is revealed by the relative motions of small kinks (short range deviation of a particle segment from a straight contour) along their backbones, recorded by video microscopy and analyzed by image processing. The kinks act as tracers and are sufficiently large for accurate imaging while small enough not to introduce significant deviation from a perfectly straight rod in terms of axial rotational diffusivity. I first track the motion of kinks in 6 - 54μm stiff rigid rods that are undergoing Brownian motion near a flat substrate to measure their axial rotational diffusivities. Subsequently I apply a magnetic field to control the distance between the rods and the substrate and measure their axial rotational diffusivities in bulk.

In this chapter, I first measure the bending relaxation dynamics of semiflexible DNA-linked magnetic particle chains using Fourier mode analysis. Then, I measure the axial

rotational diffusivities of rigid chains both in bulk and near a wall. Both experimental data match reasonably well with theoretical predictions[7, 14-16], confirming the validity of the slender-body hydrodynamic theory calculations and our system a good model system for polymer dynamics studies.

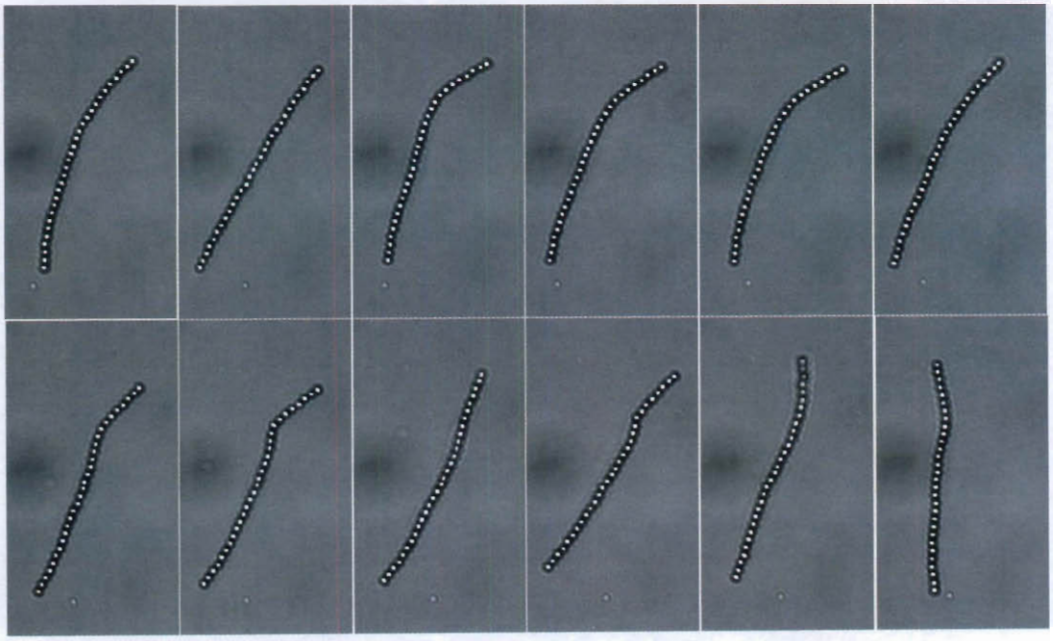

Figure 4.2. Snapshots of a 30-bead semiflexible DNA-linked chain (Lp=1mm) under Brownian motion in aqueous solution near the bottom substrate. The snapshots are taken 10 seconds apart.

4.2. Experimental methods and materials

4.2.1. Sample preparation

As previous described, paramagnetic polystyrene MyOne beads with diameter 1.08 ± 0.05μm (density ~1.8 x 10^3 kg/m^3) and streptavidin surface coating (Dynal Biotech,Oslo, Norway) are used in this study. They are further functionalized with biotinylated 15-base oligonucleotides[17] (surface density 5 x 10^4 strand/μm^2) and dispersed in phosphate buffer solution (pH = 7.4) with ionic strength of 60 mM. These beads are linked into straight rigid chains after mixing with linker DNA (0.03 mM) and aligned under an external magnetic field for 2 hours. Due to slight non-uniformity in the distribution of magnetic material inside the particles, their centers of mass deviate from the straight-line magnetic dipole alignment, forming kinks. These kinks are made permanent by hybridization of linker DNA and particle surface DNA. When the field is removed, all the linked chains undergo quasi-2D Brownian motion near the substrate due to gravity (Figure 4.3a). Their persistence lengths are measured to be 50 ± 7 mm (L/Lp ranging from 0.00005 to 0.001) via Fourier mode analysis of their curvature thermal fluctuation[18]. The Brownian motion of the isolated chains are observed using an inverted optical microscope with an 100× oil immersion objective (Olympus IX71, Olympus America Inc., Melville, NY) and recorded using a CCD camera (Orca-HR, Hamamatsu Inc., Sewickley, PA) at ~20 frames per second and 5-millisecond exposure time for 20 minutes (Figure 4.1a-h and Figure 4.2). For each frame, the centroid position of each particle within the chain is obtained by fitting its intensity profile with a Gaussian distribution after eliminating image noise using boxcar average and Gaussian convolution to the whole image[17, 19].

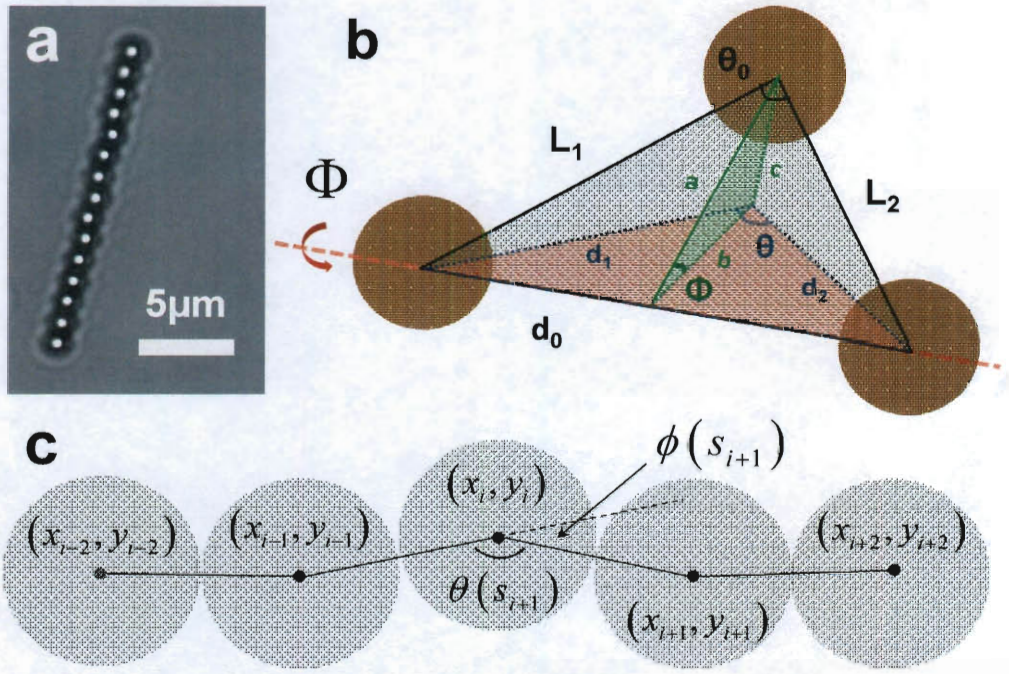

Figure 4.3. Measuring axial rotation of a 15-bead DNA-linked chain by tracking motions of kinks. a) Snapshot of a 15-bead DNA-linked chain undergoing Brownian motion. b) Geometry of a kink in 3D configuration and its projection. c) Definitions of position coordinates, bond angle $\phi(s_i)$ and tangent angle $\theta(s_i) = \pi - \phi(s_i)$ along the chain.

4.2.2. Axial rotational angle measurement

For each chain near the substrate, I first measure the diffusivity of regular in-plane rotation about its short axis and compare with theory[1] to ensure that the chain is not attached to the substrate (Figure 4.4).

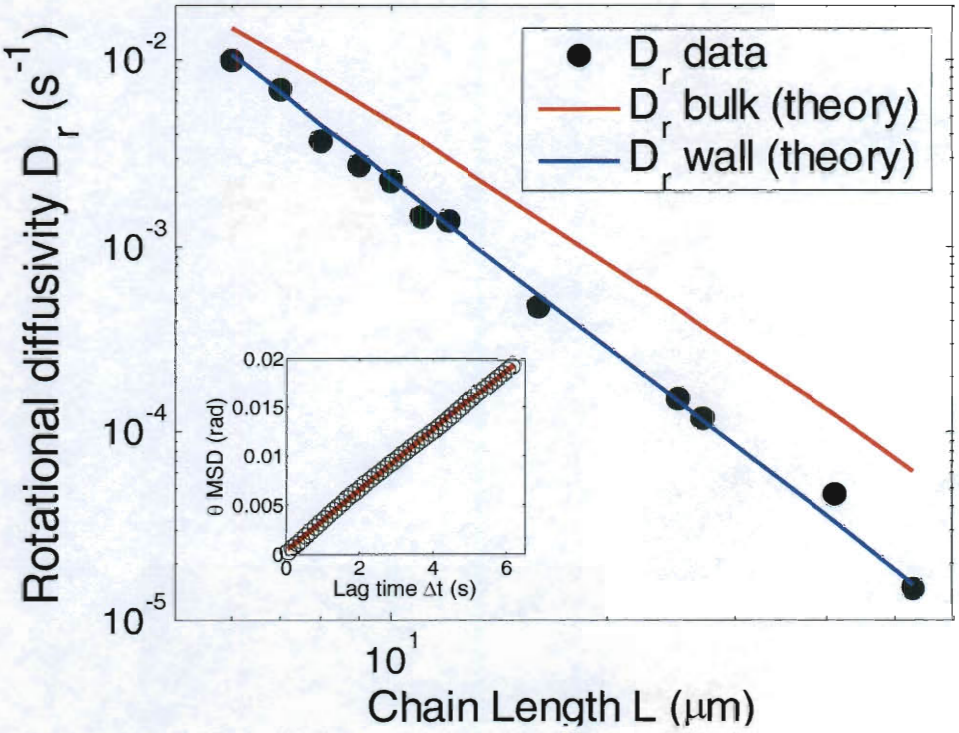

Figure 4.4. Measurement of in-plane rotational diffusivities of chains of different length diffusing near a wall. The measured diffusivities of all the chains match with theory describing rigid rods diffusing near a wall (with gap size 0.13μm). This indicates that all the chains measured are freely diffusing without attaching to the substrate.

To measure bulk axial rotational diffusivity of rigid rods, I use a magnetic gradient field to balance the gravitational force acting on the rods. After identifying an isolated straight chain, I levitate it to a certain height (~10 μm) above the substrate using the magnetic field gradient generated by two block magnets (2"×1"×1/2", 5738K33, McMaster-Carr, Elmhurst, Illinois, USA) placed 4.9 cm away from each other. At equilibrium height range, the magnetic gradient force is equal in magnitude to the rod's gravity (gravity minus buoyancy) but in the opposite direction. The height of the chain is determined by a

reference bead stuck to the substrate using a z-direction calibrated objective. The chain is seen diffusing freely along the vertical axis, indicating that the forces in the z-direction are balanced (Figure 4.8 top-right inset).

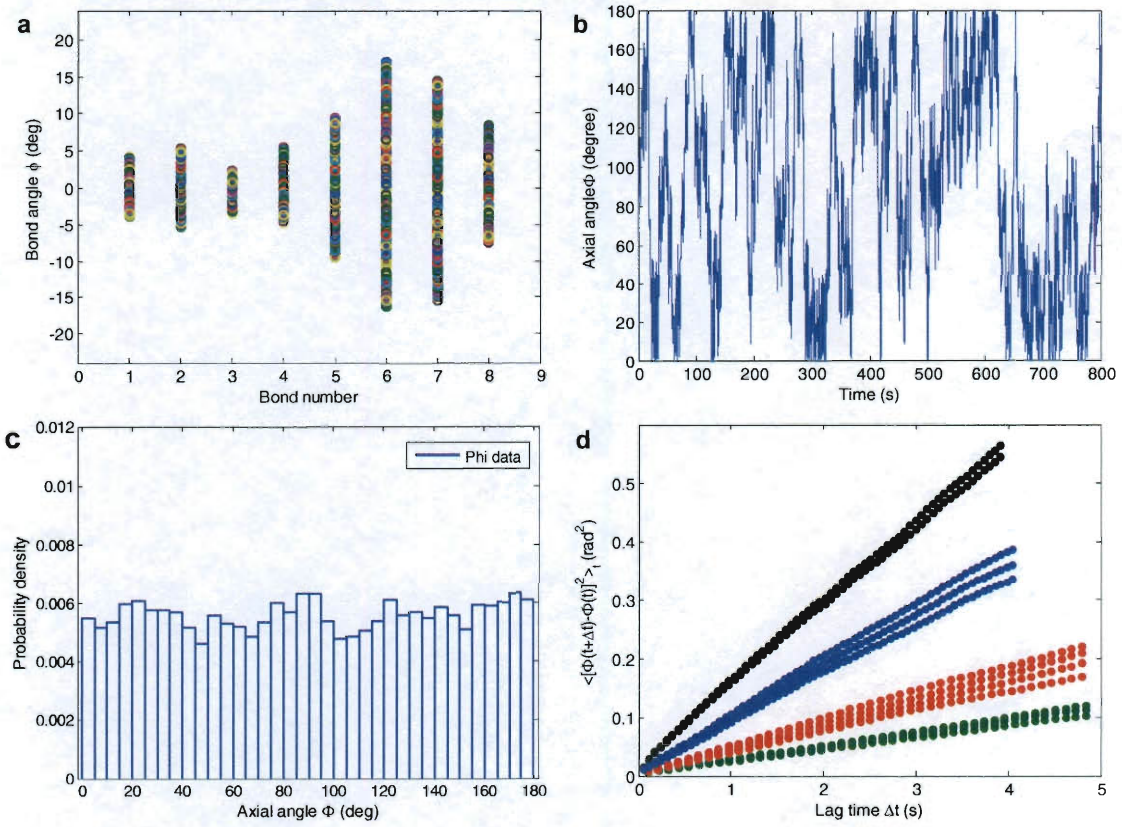

Figure 4.5. a) Overlay of bond angles ϕ of all kinks in a 10-bead chain within 800 seconds. b) Axial rotational angle $\Phi(t)$ measured from the sixth kink of the same chain in a). c) Histogram of the same angles in plot b). d) Typical plot of axial rotational angular mean-squared displacement (MSD) as a function lag time of 10-bead (black circle), 16-bead (blue circles), 30-bead (red circles) and 40-bead (green circles) chains in bulk.

Inter-particle distances are calculated as $d_i = \sqrt{(x_{i+1} - x_i)^2 + (y_{i+1} - y_i)^2}$ where d_i is the distance between the i[th] and (i+1)[th] bead. Bond angles (Figure 4.3c) are subsequently calculated as $\phi(s_i) = \cos^{-1}\left(\mathbf{u}_{i+1} \bullet \mathbf{u}_i / |\mathbf{u}_{i+1}| \cdot |\mathbf{u}_i|\right)$, where $\mathbf{u}_i = (x_{i+1} - x_i, y_{i+1} - y_i)$ is the bond vector connecting the i[th] and (i+1)[th] bead. Since the arc-cosine function does not give negative values for small negative angles, I use the sign of $y_{i+1} - y_i$ as the sign of $\phi(s_i)$ so that it ranges from $-\pi/2$ to $\pi/2$.

The distribution of bond angles between each pair of bond vectors (bond number) can be measured (Figure 4.5a). For example, the bond angle between the 1[st] and 2[nd] vectors (bond number 1) ranges from -5 degrees to 5 degrees while the bond angles between the 7[th] and 8[th] vectors (bond number 7) range from -15 to 15 degrees. Since this range of angles is symmetric about 0 degrees, it indicates that the chain is making full axial rotations. I can calculate the axial rotation angle $\Phi(s_i)$ based on the kinks whose bond angle exceeds 14 degrees. The choice of this angle is arbitrary but will be detailed later in this chapter. My intention is to minimize error while still providing a large enough number of kinks within a chain to provide statistics. For each kink, I compute the axial rotation angle $\Phi(s_i)$ based on the geometry illustrated in Figure 2b where solid lines represent a 3D construct and dashed lines are 2D projections on the image plane. θ_0 is assumed to be fixed for a given kink due to rigidity and is calculated as $\theta_0 = \max\{abs(\theta(t))\}$ after obtaining all $\theta(t)$ for the kink. The trigonometric relations between all variables in Figure 4.3b are presented in the following equations,

$$\begin{cases} d_1 d_2 \sin\theta_1 - b d_0 = 0 \\ L_1 L_2 \sin\theta_0 - a d_0 = 0 \\ b^2 + c^2 - a^2 = 0 \\ d_1^2 + c^2 - L_1^2 = 0 \\ d_2^2 + c^2 - L_2^2 = 0 \end{cases} \tag{4.1}$$

where d_1, d_2, d_0, θ_0 and θ are obtained from the analysis of each image and L_1, L_2, a, b and c are 5 unknowns to be computed from the above 5 equations. The axial rotation angle $\Phi(s_i)$ is calculated as $\Phi(s_i) = \cos^{-1}(b/a)$ and it spans between 0 and π (Figure 4.5b). The fact that $\Phi(s_i)$ has a uniform distribution (Figure 4.5c) indicates the rods undergo Brownian motion without any bias in the direction of axial rotation. Mean squared displacement (MSD) of $\Phi(s_i)$ of each chosen kink within a rod is plotted against lag time (Figure 4.5d). Finally, the axial rotational diffusivities D_{ar} are calculated by fitting a straight line to the MSD vs. lag time curve using the Einstein relation $\left\langle \left(\Phi(t+\Delta t) - \Phi(t)\right)^2 \right\rangle_t = 2D_{ar}\Delta t$. D_{ar} values from different kinks within each rod are averaged to give the final diffusivity values and their standard deviations.

4.3. Theory

4.3.1. Relaxation time scales of modes

As shown in the previous chapter, persistence length can also be estimated from the bending dynamics of each mode by examining its relaxation time scale. Although Fourier modes are not the true normal modes of the equation of motion that describes the dynamics of a chain because the end-effects do not satisfy the boundary conditions, they nevertheless are reasonable approximations to the true normal modes in computing the relaxation times[20,21]. The single-exponential relaxation of the modes is described as,

$$\left\langle \left(a_n(t+\Delta t)-a_n(t)\right)^2 \right\rangle_t = \left(1-e^{-\Delta t/\tau_n}\right)\frac{L^2}{n^2\pi^2 L_P} \tag{4.2}$$

with the relaxation time of the n[th] mode τ_n being approximated by[20]

$$\tau_n \approx \frac{\gamma}{kTL_P}q^{-4} \tag{4.3}$$

where the wavevector $q=\pi(n+1/2)/L$, and γ is either the bulk drag coefficient[22] of a chain in an unbounded environment $\gamma \approx 4\pi\eta/\left[\ln\left(L/2a\right)+0.84\right]$ or the effective

hydrodynamic drag coefficient for a rigid chain near a flat rigid substrate and with its orientation parallel to the substrate[16,23]:

$$\gamma \approx \frac{4\pi\eta}{\cosh^{-1}(\frac{h}{r})} \tag{4.4}$$

where h is the distance between the center of the chain to the substrate, η is the solvent viscosity, and r is the radius of the chain, which is the average radius of the beads in the chain. By plotting the amplitudes as a function of lag time and fitting them with Equation 4.2, one can obtain the relaxation time for each mode. Persistence length can then be estimated using Equations 4.3 and 4.4.

4.3.2. Axial diffusivities of rigid rods in bulk and near a wall

The drag coefficient of a rigid rod rotating around its long axis predicted by slender-body hydrodynamic theory[5,14,24] is approximately the sum of rotational drag coefficients of spheres, $8\pi\eta r^3$, constituting the rod, i.e.,

$$D_{ar}^{Bulk} = \frac{k_B T}{4\pi\eta r^2 L} \tag{4.5}$$

where k_B is Boltzmann constant, T is absolute temperature, η is the solvent viscosity, r is the radius of a bead and, L is the length of the rod. A more detailed shell-model [7,24]

gives $D_{ar}^{Bulk} = k_B T / 3.84\pi\eta r^2 L\left(1+0.677p^{-1}-0.183p^{-2}\right)$, where $p = L/2r$ is the aspect ratio of the rod. Because the rods investigated in this letter have aspect ratio ranging from 6 to 50, the difference between the two expressions is negligible (<4%) and for simplicity, I use Equation 4.5 to compare with experimental results.

Near a wall, diffusion is slower due to the hydrodynamic reflections of the rod on the wall. The wall hinders axial rotational diffusion according to [15,25]

$$D_{ar}^{Wall} = \frac{k_B T}{4\pi\eta r^2 L}\sqrt{1-(r/h)^2} \tag{4.6}$$

where h is the distance between the center of the rod (beads) and the wall.

4.4. Results and discussions

4.4.1. Semiflexible chain bending relaxation dynamics

To validate the DNA-linked particle chains to be a model system for semiflexible polymers, I characterize their dynamic relaxation properties using Fourier mode analysis. Since Fourier modes are a convenient basis set that captures the shape of a chain at any given point in time, it is well suited for calculating equilibrium properties such as persistence length. However, Fourier modes are not true normal modes of the dynamical

equation of motion of a chain[20], because they do not completely satisfy the no-force-no-torque boundary conditions on both ends of a chain[21,26]. This end effect results in a possible non-single-exponential relaxation behavior that differs from that described in Equation 4.2. The deviation decreases with increasing mode number where the end effect is less pronounced. Nevertheless, it is found that within the experimentally accessible timescales, this non-single-exponential effect is small (Figure 4.6) and Fourier modes still provide reasonable approximations of relaxation times within 10~15% error[21].

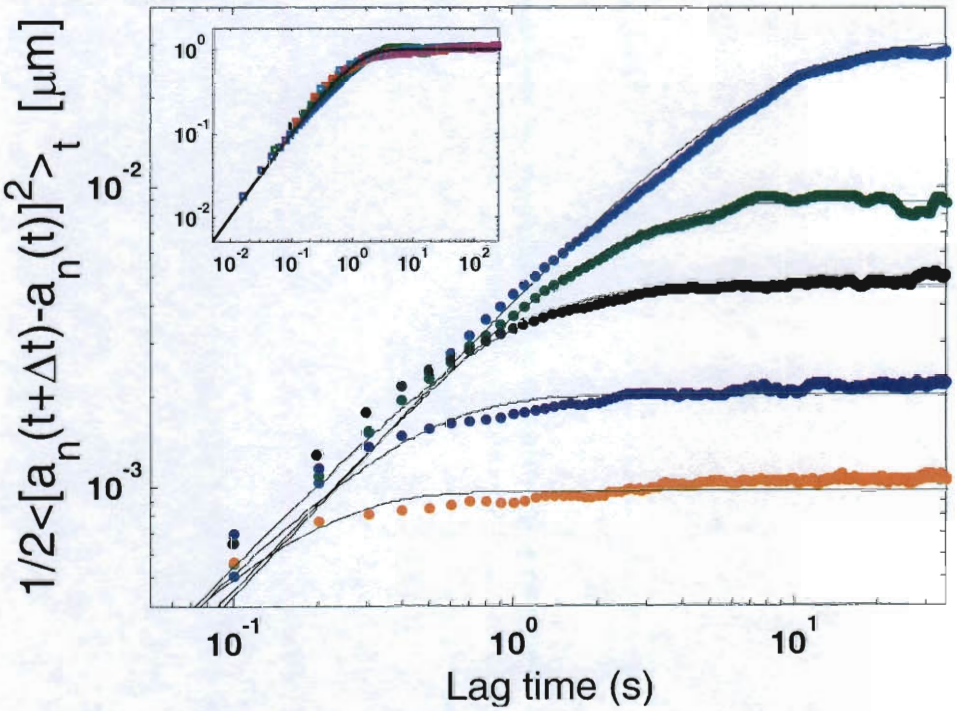

Figure 4.6. Lag time-dependence of mode amplitude of the first five modes of a 70-bead chain with 35-base surface DNA-coated particles. Lines are single-exponential fits to the data points using Equation 4.2. Insert: data points collapse into a single master curve using scaled variables $MSD(a_n)/MSD(a_n)_{plateau}$ and t/τ_n (n=1,2,3,4,5).

The relaxation behavior of lower modes ($n < 6$) is reasonably characterized by single-exponential saturation from Equation 4.2 (Figure 4.6), while higher modes ($n > 10$) show anomalous slow relaxation due to the effect of axial rotation of kinks (data not shown). Note that when the variables are scaled with their respective saturation amplitudes and relaxation times, they collapse into a single exponential master curve (Figure 4.6 inset). If the relaxation dynamics of the chains are measured in an unbounded environment where the hydrodynamic drag coefficients are the same as in bulk, the relaxation times of each mode can provide an independent estimate of the persistence length. However, the density of the particles is significantly larger than that of the buffer solution and the chains settle to the glass surface with an average distance of 50~300 nm from the bottom (estimated by comparing with the focal plane of a particle stuck to the substrate). This wall effect greatly increases the viscous dissipation[16,25] and thus the effective hydrodynamic drag coefficient of the chains. By using the persistence length of a measured chain, I can obtain the effective drag coefficient (Equation 4.3) and thus its average elevation (Equation 4.4) from the substrate.

The collected data for the relaxation times τ_n of 4 chains assembled by 35-base surface DNA particles of various chain lengths (36~70 beads) is plotted in Figure 4.7 as a function of wavevector. The data displays the expected q^{-4} dependence. The data is fit to Equation 4.3 using the average persistence length, $L_p = 30mm$, and an effective drag coefficient of $\gamma = 17.6\ mPa \cdot s$ and an average elevation of $h \approx 150$ nm is calculated, which is in reasonable agreement with the estimated elevation range. For a consistency

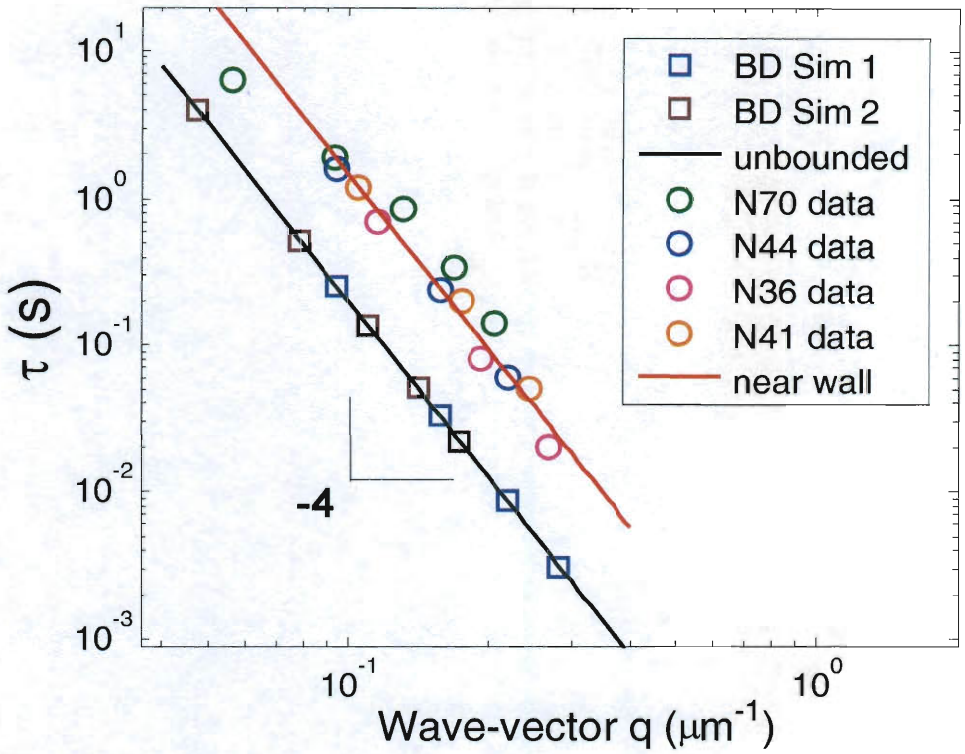

Figure 4.7. Relaxation times of bending modes of chains with average persistence length 30 mm. Open circles are experimental data for chains assembled by 35-base surface DNA-coated particles of various chain lengths (36~70 beads). Open squares are results of two chains of the same persistence length from Brownian dynamics simulations (40 and 100 beads). Red line is the best fit for experimental data using Equation 4.3 by varying γ (or height h). Black line is the exact solution of Equation 4.3 using the unbounded hydrodynamic drag coefficient.

check, relaxation times of two chains of the same persistence length from Brownian dynamics simulations are also plotted and are shown to display the same q^{-4} dependence as well as a perfect match to the exact solution of Equation 4.3 using the bulk drag coefficient. The above evidence confirms the homogeneous nature of bending relaxation behaviors of DNA-linked colloidal particle chains at larger length scales, again certifying them as model systems to study the behavior of semiflexible polymers. Caution has to be taken when one interprets the dynamics of these chains near a wall where thermal motion is surpressed due to higher effective hydrodynamic drag induced by elevated chain-wall viscous dissapation.

4.4.2. Rigid chain axial rotation dynamics

To test the slender-body hydrodynamic theory, the axial rotational diffusivities of rigid rods in bulk liquid are measured. For each chain I monitored, a magnetic field is applied that has a gradient in the vertical direction but is uniform in the horizontal plane. The magnetic field in the horizontal plane induces dipole interactions that keep the chain from rotating in the image plane[17,28], but do not affect the force balance in the image plane; therefore, the axial rotational diffusion of the chain should not be affected. The measured bulk axial rotational diffusivities of the 6 rigid chains (green circles in Figure 4.8) decrease with increasing chain length, L, in agreement with slender-body hydrodynamic theory (red line in Figure 4.8).

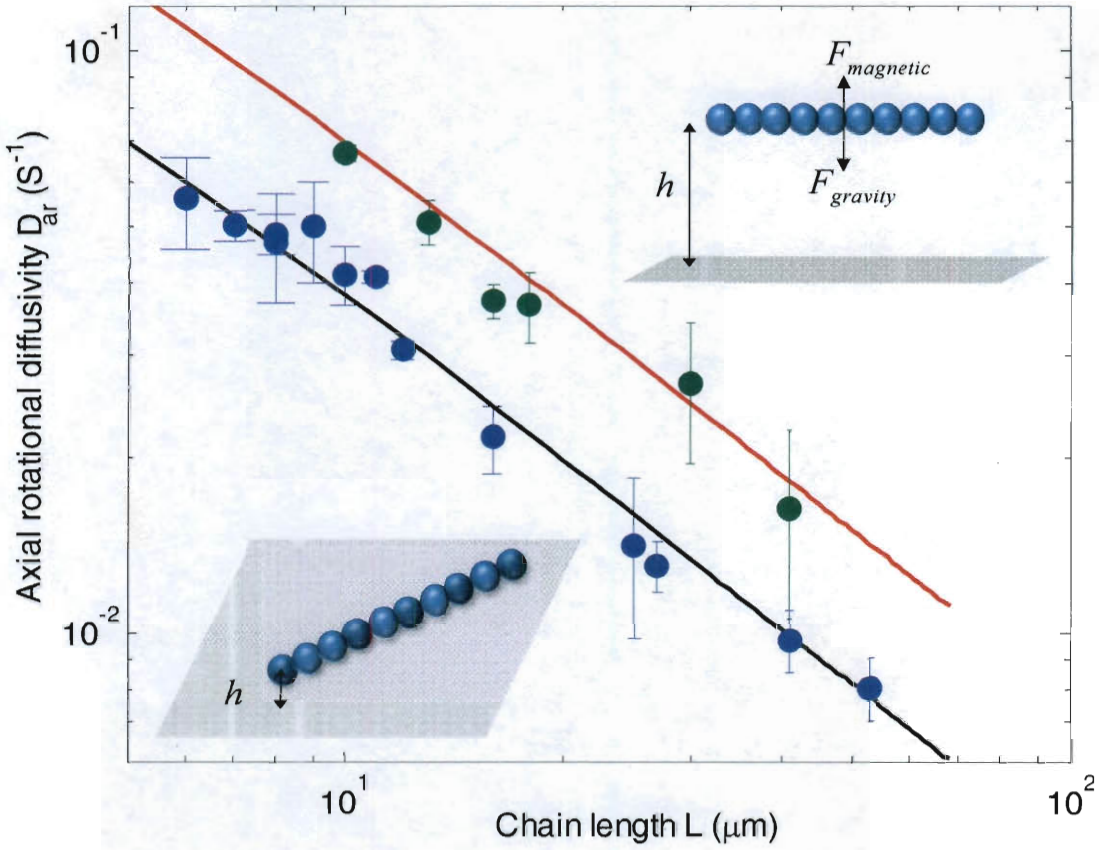

Figure 4.8. Axial rotational diffusivities of rigid rods. Slender-body hydrodynamics thoery predictions of axial roational diffusivitis in bulk (red line) and near a wall (black line) as a function of rod lengths. Experimental measured axial rotational diffusivities of rods in bulk (green circles) and near a wall (blue circles). Error bars are standard deviations of axial rotational diffusivities obtained from different kinks of the same chains. (*Insets*) Schematic illustrations of a chain near a wall (bottom left, where h is the distance between the center of the beads and the wall) and a chain elevated by a magnetic field (top right). Distances are not to scale.

Experimentally, the axial rotational diffusivities of rigid rods are measured near a wall by monitoring their Brownian motion near the glass substrate. Due to the high density of the paramagnetic beads (~1800 kg/m^3), chains longer than 6 beads are confined in quasi-2D[11] and rarely fluctuate out of focal plane (~300 nm). The 13 data points (blue circles in Figure 4.8) fit reasonably well with Equation 4.6 with a power law of -1 (black line in Figure 4.8) in a log-log plot. The right-hand side of Equation 4.6 contains the same bulk diffusivity term as in Equation 4.5 and a factor determined by the height of the rod above the substrate. Because no systematic deviation of data points from Equation 4.6 is observed when using a single fitting parameter. h ($h = r + 0.12\mu m$), all the chains, long and short, have approximately the same average height above the substrate. The value of the height is in agreement with both the height of the same chains calculated using their short-axis rotational dynamics data ($h = r + 0.13\mu m$, Figure 3.4) and the height of more flexible chains calculated from their bending relaxation dynamics ($h = r + 0.15\mu m$)[11]. The above evidence strongly suggests the validity of previous hydrodynamic dissipation model.

While high precision in our axial rotational diffusivity measurement is claimed, particular attention has to be paid to quantify all the major sources of error. Error (1) comes from the inaccuracy in determining the particles' centers of mass positions. A ±4 nm position error[17] would lead to $1^o \sim 4^o$ error in the $\Phi(s_i)$ measurement, depending on the instantaneous position of the kink, for kinks of size larger than 14^o ($\phi(s_i) \geq 14^o$). This random error source ultimately leads to a systematic underestimate of diffusivity by up to 3%. Error (2) comes from the fact that kinks are ubiquitous in any rod I measure.

Depending on the size of each kink, its effect on the deviation of the axial rotational drag coefficient of the whole chain is given by the expression $\zeta^{error} = 6\pi\eta rz^2$ [29], where z is the particle center of mass deviation from the long axis. I use the theory for straight rigid rods that does not take into account the kinks with size $2^o \le \phi(s_i) \le 20^o$, which is equivalent to an overestimate of diffusivity by 2%. Error (3) results from the fact that the $\phi(s_i)$ angles should vary between -∞ and +∞ but are only measured to be between -π/2 and π/2. This effect is equivalent to confined 1D diffusion between 2 walls[30] and would bend and saturate the MSD vs. time curves (Figure 3.5d) when time approaches the axial rotational relaxation time scale. This effect could potentially result in an underestimate of diffusivity by $O\left(t/2\pi^2\tau\right)$. I reduce this underestimation to less than 1% by limiting the time scale plotted to be less than 5% of the relaxation time scale. As seen in Figure 3.5d, the MSD vs. time curves are straight within 0~5s timeframe (relaxation time 200~1000s). Error (4) is due to the assumption in the geometric calculation that both centers of mass of the particles (left and right in Figure 3.3b) next to the kinked particle (top one in Figure 3.3b) are on the rotation axis, which might not be true due to the fact that the kink arrangement within a rod is random and 3D in nature. Error (5) is caused by occasional tilting of the rods during recording that results in inaccurate measurements of the particle positions. Errors (4) and (5) are negligible (causing the final measured diffusivity values to be <1%) since the tilting angle and the degree of axis mismatch are small enough[17,19]. In summary, a conservative estimate of error would be ±3%, which is unprecedented in single rod axial rotational diffusivity measurements.

4.5. Conclusions

In this chapter I have present a novel model of DNA-linked paramagnetic colloidal particle chains with a wide range of bending rigidities to study the semiflexible and rigid rod dynamics. I have measured the bending relaxation dynamics of semiflexible chains of persistence lengths 1~50mm, the results of which show good agreement with existing worm-like chain polymer theory. In addition, I have demonstrated a convenient and systematic approach to measure axial rotational diffusivities of colloidal rigid rods of length 6~54μm, both in bulk and near a wall. I have shown that the experimentally measured diffusivities match reasonably well with slender-body hydrodynamics theory calculations. Our DNA-linked colloidal rods, with controllable length, rigidity and elevation, in conjunction with the imaging and processing technique provide an excellent prototype to study semiflexible filament axial rotation, twisting and writhing dynamics. I believe this opens the door to investigating polymer dynamics using colloidal rods both in bulk and confined environments.

4.6. Reference

1. Han, Y.; Alsayed, A. M.; Nobili, M.; Zhang, J.; Lubensky, T. C.; Yodh, A. G., Brownian motion of an ellipsoid. *Science* **2006,** 314, (5799), 626-630.
2. Fakhri, N.; MacKintosh, F. C.; Lounis, B.; Cognet, L.; Pasquali, M., Brownian Motion of Stiff Filaments in a Crowded Environment. *Science* **2010,** 330, (6012), 1804-1807.
3. Leisen, J.; Werth, M.; Boeffel, C.; Spiess, H. W., Molecular dynamics at the glass transition - 1D and 2D nuclear magnetic resonance studies of a glass-forming discotic liquid-crystal. *Journal of Chemical Physics* **1992,** 97, (5), 3749-3759.
4. Pastor, R. W.; Venable, R. M.; Karplus, M., Model for the structure of lipid bilayer. *Proceedings of the National Academy of Sciences of the United States of America* **1991,** 88, (3), 892-896.
5. Yajima, J.; Cross, R. A., A torque component in the kinesin-1 power stroke. *Nature Chemical Biology* **2005,** 1, (6), 338-341.
6. Yajima, J.; Mizutani, K.; Nishizaka, T., A torque component present in mitotic kinesin Eg5 revealed by three-dimensional tracking. *Nature Structural & Molecular Biology* **2008,** 15, (10), 1119-1121.
7. Delatorre, J. G.; Bloomfield, V. A., Hydrodynamic properties of complex, rigid, biological macromolecules - Theory and applications. *Quarterly Reviews of Biophysics* **1981,** 14, (1), 81-139.
8. Christensen, R. L.; Drake, R. C.; Phillips, D., Time-resolved fluorescence anisotropy of perylene. *Journal of Physical Chemistry* **1986,** 90, (22), 5960-5967.
9. Nitzsche, B.; Ruhnow, F.; Diez, S., Quantum-dot-assisted characterization of microtubule rotations during cargo transport. *Nature Nanotechnology* **2008,** 3, (9), 552-556.
10. Hong, L.; Anthony, S. M.; Granick, S., Rotation in suspension of a rod-shaped colloid. *Langmuir* **2006,** 22, (17), 7128-7131.
11. Li, D. C.; Banon, S.; Biswal, S. L., Bending dynamics of DNA-linked colloidal particle chains. *Soft Matter* **2010,** 6, (17), 4197-4204.
12. Brown, R., A brief account of microscopical observations on the particles contained in the pollen of plants and the general existence of active molecules in organic and inorganic bodies. *Not Published* **1827.**
13. Li, D. C.; Rogers, J.; Biswal, S. L., Probing the Stability of Magnetically Assembled DNA-Linked Colloidal Chains. *Langmuir* **2009,** 25, (16), 8944-8950.
14. Cox, R. G., The motion of long slender bodies in a viscous fluid. Part 1. General theory. *Journal of Fluid Mechanics* **1970,** 44, 791-810.
15. Jeffrey, D. J.; Onishi, Y., The slow motion of a cylinder next to a plane wall. *Quarterly Journal of Mechanics and Applied Mathematics* **1981,** 34, (MAY), 129-137.
16. Hunt, A. J.; Gittes, F.; Howard, J., The force exerted by a single kinesin on molecule against a viscous load. *Biophysical Journal* **1994,** 67, (2), 766-781.
17. Li, D. C.; Lam, C. N.; Biswal, S. L., Measuring short-range repulsive forces by imaging directed magnetic-particle assembly title. *Soft Matter* **2010,** 6, (2), 239-242.

18. Li, D. C.; Banon, S.; Biswal, S. L., Bending dynamics of DNA-linked colloidal particle chains. *Soft Matter* **2010**.
19. Crocker, J. C.; Grier, D. G., Methods of digital video microscopy for colloidal studies. *Journal of Colloid and Interface Science* **1996,** 179, (1), 298-310.
20. Gittes, F.; Mickey, B.; Nettleton, J.; Howard, J., Flexual rigidity of mircortubules and actin-filaments measured from thermal fluctuations in shape. *Journal of Cell Biology* **1993,** 120, (4), 923-934.
21. Brangwynne, C. P.; Koenderink, G. H.; Barry, E.; Dogic, Z.; MacKintosh, F. C.; Weitz, D. A., Bending dynamics of fluctuating biopolymers probed by automated high-resolution filament tracking. *Biophysical Journal* **2007,** 93, (1), 346-359.
22. Edwards, M. D. a. S. F., *The Theory of Polymer Dynamics*. Oxford University: Oxford, 1986.
23. Brenner, H., Effect of finite boundaries on the Stokes resistance of an arbitrary particle. *Journal of Fluid Mechanics* **1962,** 12, (1), 35-48.
24. Brennen, C.; Winet, H., Fluid mechanics of propulsion by cilia and flagella. *Annual Review of Fluid Mechanics* **1977,** 9, 339-398.
25. Tirado, M. M.; Garciadelatorre, J., Rotational dynamics of rigid, symmetric top macromolecules - application to circular cylinders. *Journal of Chemical Physics* **1980,** 73, (4), 1986-1993.
26. Howard, J., *Mechanics of Motor Proteins and the Cytoskeleton*. Sinauer Associates, Inc.: Sunderland, Massachusetts, 2001.
27. Aragon, S. R.; Pecora, R., Dynamics of wormlike chains. *Macromolecules* **1985,** 18, (10), 1868-1875.
28. Biswal, S. L.; Gast, A. P., Rotational dynamics of semiflexible paramagnetic particle chains. *Physical Review E* **2004,** 69, (4), 9.
29. Suzuki, N.; Miyata, H.; Ishiwata, S.; Kinosita, K., Preparation of bead-tailed actin filaments: Estimation of the torque produced by the sliding force in an in vitro motility assay. *Biophysical Journal* **1996,** 70, (1), 401-408.
30. Bickel, T., A note on confined diffusion. *Physica a-Statistical Mechanics and Its Applications* **2007,** 377, (1), 24-32.

Chapter 5

The use of paramagnetic particles as a repulsive colloidal force probe

In this chapter, I present the use of video microscopy of magnetic colloidal particles to measure short range repulsive forces between surfaces. The forces between the particles can be directly measured by monitoring the inter-centroid distances between the particles at various magnetic field strengths. Using a chain consisting of a minimum of 35 micron sized particles, a distance resolution of ~0.21 nm is achieved. Measurements of the interactions between charged and oligonucleotide-coated surfaces agree well with predicted force interactions calculated using Derjaguin-Landau-Verwey- Overbeek (DLVO) theory and Milner's polymer brush theory.

5.1. Introduction to colloidal force measurement techniques

Repulsive surface interactions control the dynamics, stability, and phase behavior of a suspension. A number of experimental techniques have been successfully developed to directly measure repulsive surface forces including the atomic force microscope (AFM) colloidal probe [1, 2], optical tweezers (OT) [3-5], and the magnetic chaining technique (MCT) [6, 7]. The AFM colloidal probe has sub-angstrom distance resolution, but its force measurement is limited to tens of pico-Newtons [8]. Meanwhile, OT and MCT can measure sub-pico-Newton forces the distance resolution is limited to ±3 nm and ±2 nm, respectively [4-7]. Direct measurements of electrostatic interactions between colloidal particles using MCT technique [6] and optical tweezers [9] have been reported. Additionally, the thermal expansion of a magnetic chain was recently used as a simple model of a one-dimensional anharmonic crystal, allowing force versus distance relationships between charged colloids to be measured [10]. The interactions between DNA-coated particle surfaces can also be measured using colloidal particles [5, 11]. However, these initial studies have not investigated short-range interactions that are on the order of pico-Newtons with angstrom-level distance resolution.

In this chapter, I combine MCT with video microscopy to measure repulsive force versus distance relationships between coated colloidal particles with a distance resolution of ~0.21 nm. By measuring the magnetic attractive force between magnetic particles at varying field strength, the repulsive surface forces can be calculated with sub-pico-Newton accuracy. Unlike the Bragg scattering technique used to measure particle spacing in MCT, distance resolution in our technique is achieved by averaging the inter-centroid distances between adjacent particles within a chain under a given magnetic field strength.

The validity of this measurement is verified by measuring the repulsive forces between charged colloidal surfaces at various salt concentrations. Our measurements are compared with Derjaguin-Landau-Verwey- Overbeek (DLVO) theory for accuracy. I also demonstrate the feasibility of measuring short-range repulsive forces between colloidal surfaces coated with 15, 35, 50, and 75 base oligonucleotides. Experimental data for the 50 and 75 base oligonucleotide-coated surfaces agrees well with polymer brush theory developed by Milner. Interestingly, the shorter 15 and 35 base oligonucleotide-coated surfaces deviate significantly from theory. This is important in understanding the self- or directed-assembly of DNA-coated colloidal particles.

5.2. Experimental methods and materials

The particles used in this study are carboxyl-coated paramagnetic polystyrene MyOne beads (Dynal Biotech, Oslo, Norway). The mean particle diameter of the particles is 1.07 ± 0.04 μm, confirmed by dynamic light scattering and scanning electron microscopy (SEM) measurements. The magnetic susceptibility of the particles varies from 1.44 to 0.78 in the field range of 0.1 mT to 50 mT, as provided by the manufacturer. The particles are taken from a stock solution, washed and sonicated in the desired sodium chloride solution (1 mM, 2 mM, or 5 mM), and diluted to a final particle concentration of 80,000 particles/μL. The zeta potential of the particles are measured to be -48.0 mV, -39.2 mV and -38.7 mV in 1 mM, 2 mM and 5 mM salt solutions, respectively. The particles are injected in a flow cell consisting of two glass coverslips sandwiched together with double-stick tape. The coverslips are washed with sulfuric acid and hydrogen

peroxide (7:3 v/v) to prevent the particles from sticking to the glass surface. The cell is then sealed with epoxy to prevent evaporation of the solution. The flow cell is placed between a pair of iron-cored Helmholtz coils, used to provide a homogeneous magnetic field within the flow cell, on an inverted optical microscope (Olympus IX71) stage with a 100x/1.2 N.A. oil immersion objective. Chains of paramagnetic colloidal particles are allowed to form under a constant flux density of 10 mT. The magnetic field is then varied and images of the chains are taken using video microscopy with a digital camera (Hamamatsu) at a rate of 5 frames/sec for 1 minute using Simple PCI software and analyzed using Matlab. Centroid positions of particles within a chain are calculated via image processing [12] and inter-centroid distances between adjacent particles are averaged over all particle pairs to give the "averaged inter-centroid distance". As shown in Figure 5.1, histograms for the inter-particle spacing are generated at various magnetic field strengths by measuring the average inter-centroid distance for a chain using 300 frames for each field strength. The standard deviation of a Gaussian fit to the histograms of the centroid distance distribution is ~0.2 nm for forces larger than 4 pN, or a field strength greater than 6mT, signifying the distance resolution of our technique. Note that at lower field strengths the inter-particle spacing distribution becomes broader due to an increase in the ratio of thermal energy to magnetic energy.

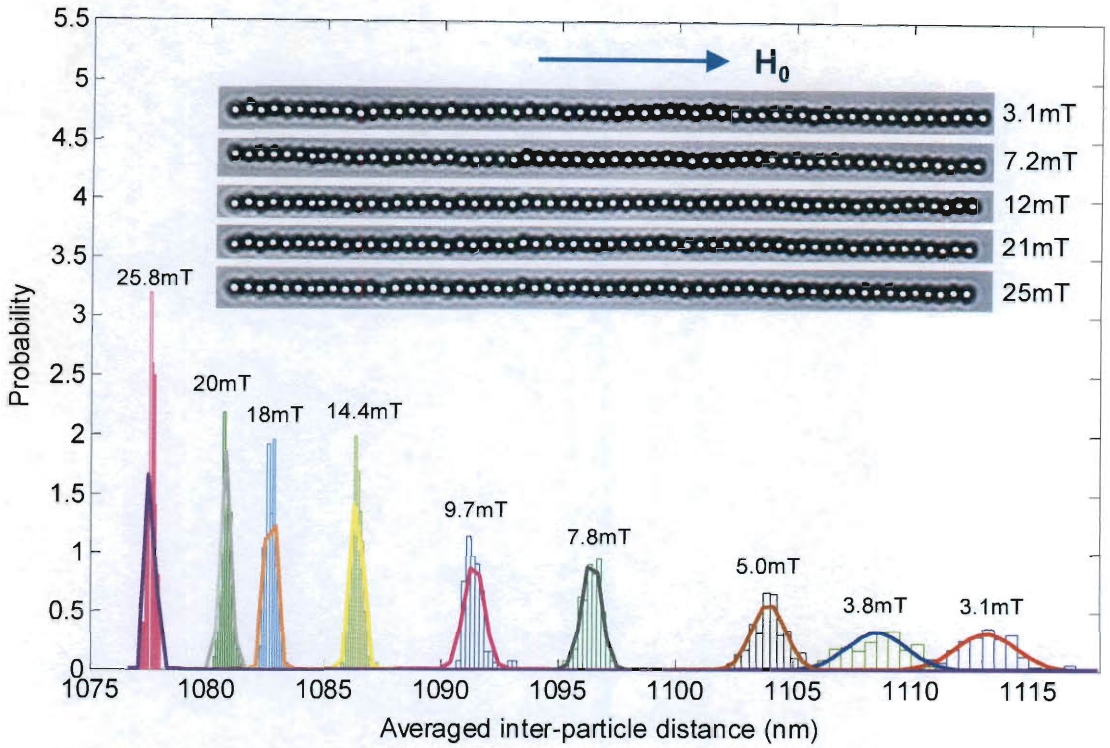

Figure 5.1. Probability distributions of particle inter-centroid distances at various magnetic field strengths in 1 mM NaCl solution. Colored lines are Gaussian fits to the distribution data, where the standard deviations provide the error estimates for the inter-centroid distance measurements. Inset: Images of a 59-particle chain dispersed in 1 mM NaCl solution taken at magnetic field strengths ranging from 3.1 mT to 25 mT.

5.3. Results and discussions

5.3.1. Like charge repulsion

I quantify the repulsive electrostatic force between the particle surfaces by measuring the magnetic force used to align the particles at a given magnetic field strength. The

magnetic force between adjacent particles aligned with the external field is calculated using Equation 5.1, proposed by Zhang and Widom [13],

$$F_{mag} = -\frac{1.202}{2\pi\mu_0} \cdot \frac{3m^2}{d^4} \tag{5.1}$$

where μ_0 is the permeability of vacuum, $m = \mu_0 \chi V B_0$ is the magnetic dipole moment of a spherical particle, χ is volumetric magnetic susceptibility, V is the volume of a particle, B_0 is the applied magnetic field strength, and d is the inter-centroid distance between the two particles. Using different salt solutions, the equilibrium inter-centroid distances between particles are measured at different magnetic field strengths and converted into a force versus particle surface separation distance relationship using Equation 5.1, as plotted in Figure 5.2. The measured force-distance relations are compared to those obtained using DLVO theory. At equilibrium, the magnetic force balances the electrostatic force. The electrostatic force profiles are calculated assuming constant potential boundary conditions, as shown in Equation 5.2,

$$F_{el} = 2\pi\varepsilon\phi_Z^2 a\kappa \frac{\exp(-\kappa D)}{1+\exp(-\kappa D)} \tag{5.2}$$

where ε is the dielectric permittivity of the medium, ϕ_Z is the zeta potential, κ is the inverse Debye length, and D is the separation between two surfaces. The diameter of the particle surface up to the "slip" plane in the electric double layer, $2a$, cannot be measured *in situ* during the experiments. Therefore, the particle diameter is a fitting parameter found to be 1059 nm, 1073.5 nm and 1061 nm for 1 mM, 2 mM and 5 mM salt solutions, respectively. The calculated DLVO force profiles, shown in Figure 5.2, show

good agreement with the experimental data, indicating that accurate force-distance measurements can be made with our technique.

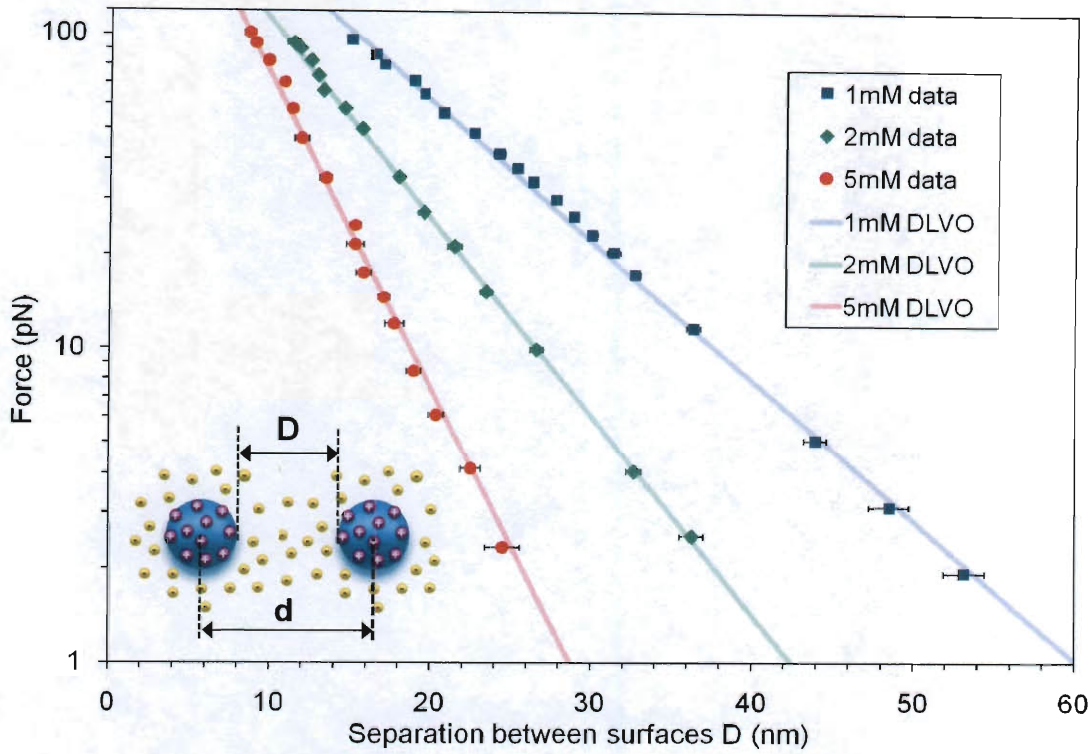

Figure 5.2. Experimentally measured force-distance profiles of charged particles at different ionic strengths: 1 mM (blue squares), 2 mM (green diamonds), and 5 mM (red circles). Solid lines of corresponding colors are obtained from DLVO theory (Equation 2) using the measured zeta potential of the particlees. Separations between surfaces are calculated by using the mean particle diameters (only fitting parameter), found to be 1059 nm (1 mM), 1073.5 nm (2 mM), and 1061 nm (5 mM), from measured inter-centroid distances. The separation error bars are standard deviations of the averaged inter-centroid distances measured using 300 images under each specific magnetic field strength.

5.3.2. Steric repulsion

To prove the capability of our method to capture short-range interactions between colloidal particles with high resolution, I demonstrate the first direct measurement of force-distance profiles between particles grafted with oligonucleotides (15, 35, 50 and 75 bases). Streptavidin-coated particles (Dynal M-270, Dynal Biotech, Oslo, Norway), with a diameter of 3.05 ± 0.1μm and a zeta potential of -50 mV, are used for the following experiments. Oligonucleotides are grafted onto the particle surfaces via streptavidn-biotin coupling [14]. Surface grafting densities are measured using a fluorescent-based complementary strand method[15] and found to be 5.0×10^4, 2.8×10^4, 8.0×10^3, and 3.5×10^3 strands/ m^2 for the 15, 35, 50, and 75-base oligonucleotide grafted particles, respectively. All particles are washed and centrifuged in phosphate buffer solution (pH = 7.4) with ionic strength of 0.12 M. The inter-centriod distances between particles are first measured as the magnetic field strength is increased, representing chain compression, and then as the magetic field strength is decreased, representing chain expansion. Using Equation 5.1, the calculated force versus distance relationships for the different oligonucleotide-grafted particles are plotted in Figure 5.3. No hysteresis is seen in the the force versus distance data profiles during chain compression and expansion. Also note that the separation distance error bars are much smaller compared to that of the previous experiment due to use of larger particles, which are less susceptible to thermal fluctations.

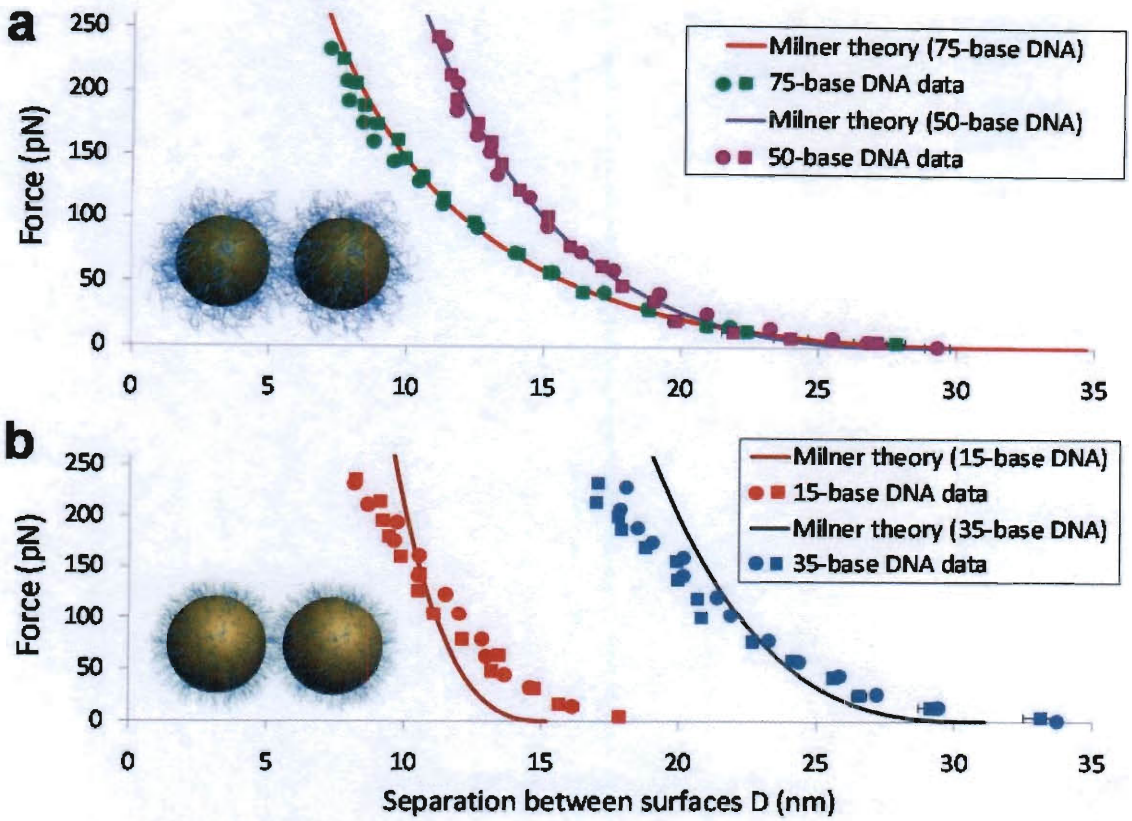

Figure 5.3. Experimentally measured force-distance (circles for chain compression and squares for chain expansion) profiles of particles grafted with different oligonucleotide lengths: a) 50-base (purple) and 75-base (green); and b) 15 base (red), and 35 base (blue). Solid lines are calculated from Milner's theory of compressed polymer brushes using the measured oligonucleotide grafting densities. Separations between surfaces are calculated by subtracting mean particle diameters (only fitting parameter) from measured inter-centroid distances. Separation error bars, given by the standard deviations of averaged inter-centroid distances measured for the 300 images under a specific magnetic field strength, are also plotted.

The theory describing the inter-particle interaction between two spherical particles with end-grafted polymers was first developed by Alexander and de Gennes [7] using scaling arguments and then by Milner using mean field theory [15]. Both theories fit well to experimental data with grafted long chain polymers [16,17]; however, the inter-particle interactions between surfaces grafted with short polymers, such as oligonucleotides with less than 100 bases, have not been confirmed by experiments. Milner's theory predicts a soft repulsive force-distance profile between two planar surfaces with uniformly grafted homopolymers [15,16]. Detailed derivations of the potential-distance law between two flat walls with grafted oligonucleotides is provided elsewhere [14-16]. The calculated force versus distance relationship, between two spherical particles, shown in Figure 5.3, can be derived using the Derjaguin approximation: $F_S(D) = \pi R E_S(D)$, where $F_S(D)$ is the steric repulsive force between two spheres, R is the particle radius and $E_S(D)$ is the steric interaction energy between flat walls grafted with the identical polymer brushes. Excellent agreement is found between our experimental results and Milner's theory for particles grafted with 50 and 75-base oligonucleotides, as shown in Figure 3a. However, the experimental force versus distance profiles start to deviate from those predicted using Milner's theory for particles grafted with 15 and 35 base oligonucleotides, shown in Figure 5.3b. This discrepancy can be attributed to neither particle surface charge nor particle surface roughness.

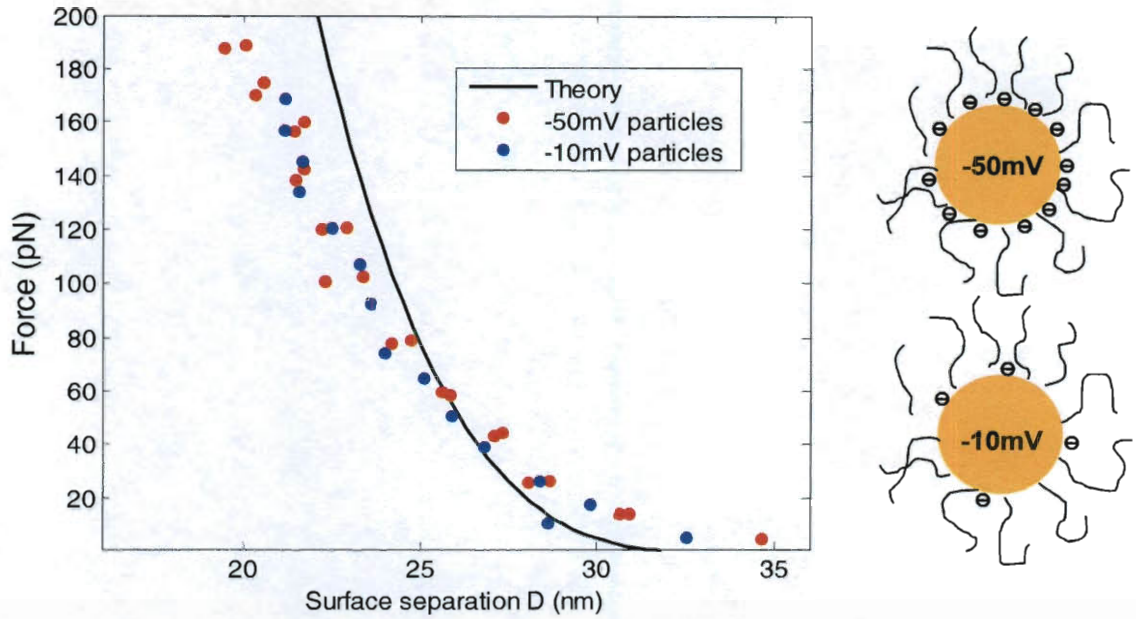

Figure 5.4. Experimentally measured force-distance profiles of particles grafted with same 35-base oligonucleotides but different zeta potentials. Solid line is calculated from Milner's theory of polymer brushes using the measured oligonucleotide grafting densities. The schematic on the right is not drawn to scale.

To investigate the effect of surface charge, I functionalized streptavidin-coated particles with a much lower surface charge density (zeta potential of -10 mV) (Dynal M-280, Dynal Biotech, Oslo, Norway), with the same 15-base and 35-base oligonucleotides using the same surface grafting densities decribed previously. Force-distance profiles obtained from these particles overlap with their higher surface-charged particle counterparts (Figure 5.4). This rules out the possibility that the discrepency between the measurments and theory are due to either electrostatic interactions between the particle surfaces or the negatively-charged oligonucleotides. Furthermore, I argue that the discrepancy is likely is

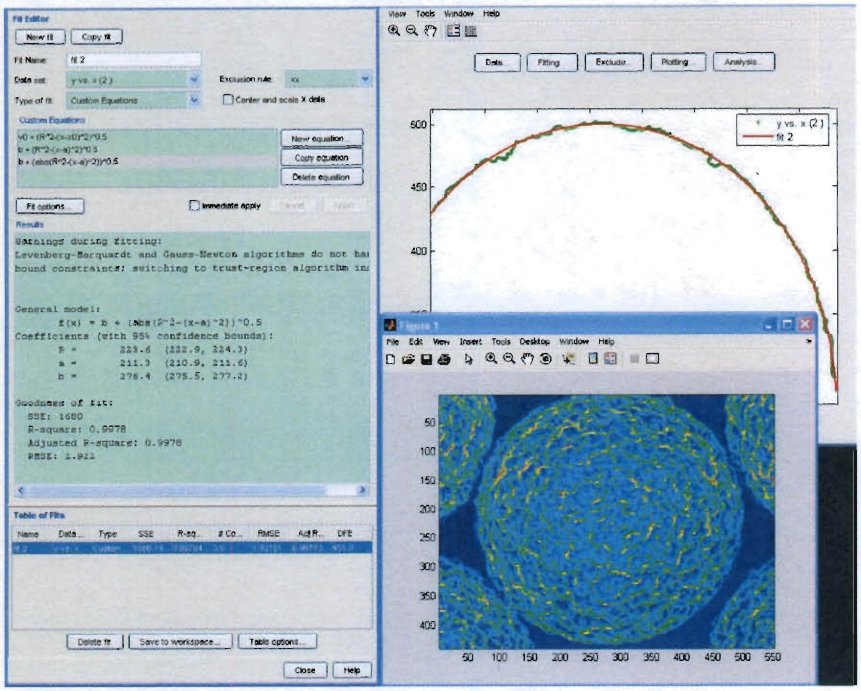

Figure 5.5. Experimentally measured roughness of the particle surface is 9nm determined using SEM and image processing via MATLAB.

due to the surface roughness of the particles since the root-mean-square roughness of these particles, measured to be ~9 nm using SEM (Figure 5.5), is comparable to the length scale of the deviations. It might also be cause by the fact that steric interactions between colloidal particles grafted with very short (< 35 bases) oligonucleotides are not well described by Milner's polymer brush theory, which is derived to predict interactions between polymer brushes in the limit of long chains. This is the first experimental data on force versus distance relations between colloidal particles grafted with short oligonucleotides. Since increasing interest in the assembly of short oligonucleotide grafted colloids continues to grow, further investigations are necessary to fully

understand the force versus distance relationship between short oligonucleotide -grafted surfaces.

5.3.3. Distance resolution

To quantify the distance resolution of this technique, I measure the maximum standard deviation of the inter-centroid distance between particles in linked chain. I record the Brownian motion of a 35-bead chain chemically linked using a 15 base-pair DNA for 30 minutes during which 11000 frames are taken (linking procedure provided in [14]). The inter-centroid distances between all adjacent bead-pairs in a chain are measured and averaged to give the averaged inter-centroid distance, shown in Figure 5.6.

The change in the averaged inter-centroid distance due to the rigid DNA linkages between particles is insignificant. The standard deviation between adjacent dimers (σ), measured to be 3 ± 1 nm, represents the spatial resolution of a single particle pair technique [4,19]. In the limit of a straight chain, the contour length of the chain has the same standard deviation as that of any dimers within the chain, with no dependence on bead number. When the chain shape roughens, or deviates from a straight line, position errors normal to the chain orientation become less negligible. Additionally, the standard deviation of the contour length becomes slightly larger with a weak dependence on the number of beads within the chain. The measured standard deviation of the contour length of a 35-bead chain is 7.1 nm, slightly larger than the mean standard deviation for dimers, indicating small deviation from a straight line conformation. The standard deviation of averaged inter-centroid distances within the chain is that of the contour length divided by

the number of adjacent particle dimers (N-1), or 0.21 nm for our 35-bead chain. This standard deviation signifies the distance resolution of our technique.

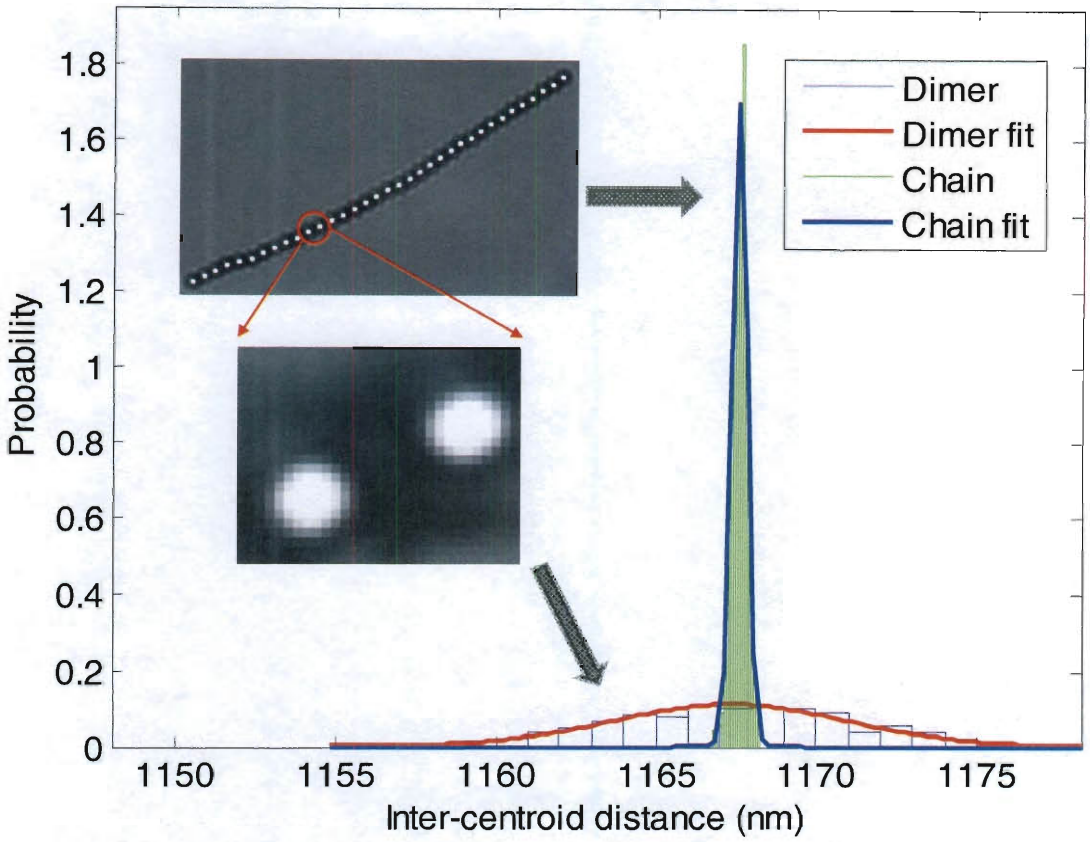

Figure 5.6. Probability distributions of inter-centroid distances for chemically linked particles measured using a particle dimer and an entire 35-particle chain. The standard deviation for the dimer distribution measured using a dimer (shown between the 11^{th} and 12^{th} particles) is 3.6 nm. The standard deviation using averaged inter-centroid distances among all particles within the linked chain (35 beads) is 0.21nm. Solid lines are Gaussian fits to the histograms.

5.4. Conclusions

In this chapter I have demonstrated the feasibility of using video microscopy of directed magnetic particle assembly to measure force versus distance relationships between coated surfaces. This technique has a distance resolution of ~0.21 nm when using a 35-bead chain. It is shown that it is possible to measure the forces between particles with great precision. This technique also allows researchers to measure short-range steric interactions between polymer brushes with reasonable accuracy. With ease of manipulation and excellent distance resolution, this technique allows measurements of a variety of short range repulsive force-distance relationship between coated colloidal particles.

5.5. Reference

1. Ducker, W. A.; Senden, T. J.; Pashley, R. M., Direct measurement of colloidal forces using an atomic force microscope. *Nature* **1991,** 353, (6341), 239-241.
2. Tarasova, A.; Griesser, H. J.; Meagher, L., AFM study of the stability of a dense affinity-bound liposome layer. *Langmuir* **2008,** 24, (14), 7371-7377.
3. Crocker, J. C.; Grier, D. G., When Like Charges Attract: The Effects of Geometrical Confinement on Long-Range Colloidal Interactions. *Physical Review Letters* **1996,** 77, (9), 1897.
4. Biancaniello, P. L.; Crocker, J. C., Line optical tweezers instrument for measuring nanoscale interactions and kinetics. *Review of Scientific Instruments* **2006,** 77, (11), 113702.
5. Kegler, K.; Salomo, M.; Kremer, F., Forces of interaction between DNA-grafted colloids: An optical tweezer measurement. *Physical Review Letters* **2007,** 98, (5), 058304.
6. Calderon, F. L.; Stora, T.; Monval, O. M.; Poulin, P.; Bibette, J., Direct measurement of colloidal forces. *Physical Review Letters* **1994,** 72, (18), 2959-2962.
7. Dreyfus, R.; Lacoste, D.; Bibette, J.; Baudry, J., Measuring colloidal forces with the magnetic chaining technique. *European Physical Journal E* **2009,** 28, (2), 113-123.
8. Israelachvili, J., *Intermolecular and Surface Forces*. Second edition ed.; Academic Press: 1991.
9. Crocker, J. C.; Grier, D. G., Microscopic measurement of the pair interaction potential of charge-stabilized colloid. *Physical Review Letters* **1994,** 73, (2), 352-355.
10. Lacoste, D.; Brangbour, C.; Bibette, J.; Baudry, J., Thermal expansion within a chain of magnetic colloidal particles. *Physical Review E* **2009,** 80, 011401.
11. Koenig, A.; Hebraud, P.; Gosse, C.; Dreyfus, R.; Baudry, J.; Bertrand, E.; Bibette, J., Magnetic force probe for nanoscale biomolecules. *Physical Review Letters* **2005,** 95, (12), 128301.
12. Crocker, J. C.; Grier, D. G., Methods of digital video microscopy for colloidal studies. *Journal of Colloid and Interface Science* **1996,** 179, (1), 298-310.
13. Zhang, H.; Widom, M., Field-induced forces in colloidal particle chains. *Physical Review E* **1995,** 51, (3), 2099-2103.
14. Li, D. C.; Banon, S.; Biswal, S. L., Bending dynamics of DNA-linked colloidal particle chains. *Soft Matter* **2010,** 6, (17), 4197-4204..
15. Li, D.; Rogers, J.; Biswal, S. L., Probing the Stability of Magnetically Assembled DNA-Linked Colloidal Chains. *Langmuir* **2009,** 25, (16), 8944–8950.
16. Milner, S. T.; Witten, T. A.; Cates, M. E., THEORY OF THE GRAFTED POLYMER BRUSH. *Macromolecules* **1988,** 21, (8), 2610-2619.
17. Milner, S. T., Compression polymer brushes - A quantitative comparison of theory and experiment. *Europhysics Letters* **1988,** 7, (8), 695-699.
18. Taunton, H. J.; Toprakcioglu, C.; Fetters, L. J.; Klein, J., Forces between surfaces bearing terminally anchored polymer-chains in good solvents. *Nature* **1988,** 332, (6166), 712-714.

19. Gutsche, C.; Keyser, U. F.; Kegler, K.; Kremer, F., Forces between single pairs of charged colloids in aqueous salt solutions. *Physical Review E* **2007,** 76, (3), 031403.

Chapter 6

Visualizing phase transitions of 2-D colloidal systems using paramagnetic particles with tunable potentials

In this chapter, I present a novel to study coexistence and phase transition behavior of a 2-D colloidal system with an effective potential that can be easily tuned. The system consists of charged paramagnetic colloidal particles in which a long-range attractive part of the pair potential is induced using a high frequency magnetic field, while the short-range repulsive part of the pair potential is controlled by electrostatic interactions between the spheres. The exciting feature of this technique this that the attractive potential can be controlled by adjusting the frequency and strength of the magnetic field. In this chapter, I measure the equilibrium phase properties by calculating the radial distribution function and the bond-orientation correlation function, phase transition dynamics, as well as phase separation. These studies allow me to construct a phase

diagram that capture the 2-D structuring of the system. In addition, Brownian Dynamics (BD) and Monte Carlo simulations are performed to compare with experimental results.

6.1. Introduction to two-dimensional colloidal system phase behavior

6.1.1. Colloids as model systems to provide "atomic" resolution

Micron-scale colloids provide an important platform for investigating statistical physics[1, 2] of atomic systems for the following reasons. First, the sizes of the colloids are small enough so that thermal energy, k_BT, drives their dynamics; that is why colloids display intriguing transitions between gas, liquid, solid and liquid crystalline phases that exist in nature (Figure 6.1). Second, micron-sized colloids are large enough to interact with electromagnetic waves in the visible region so that their instantaneous locations can be tracked precisely on a single-object level, even in bulk samples. Third, their interactions can be precisely manipulated by surface functionalization[3, 4], solvent type, and external fields[4, 5]. For these reasons, colloidal particles can mimic both equilibrium and dynamic behavior of atomic systems, providing an ideal model experimental system to study statistical physics with "atomic" resolution.

.

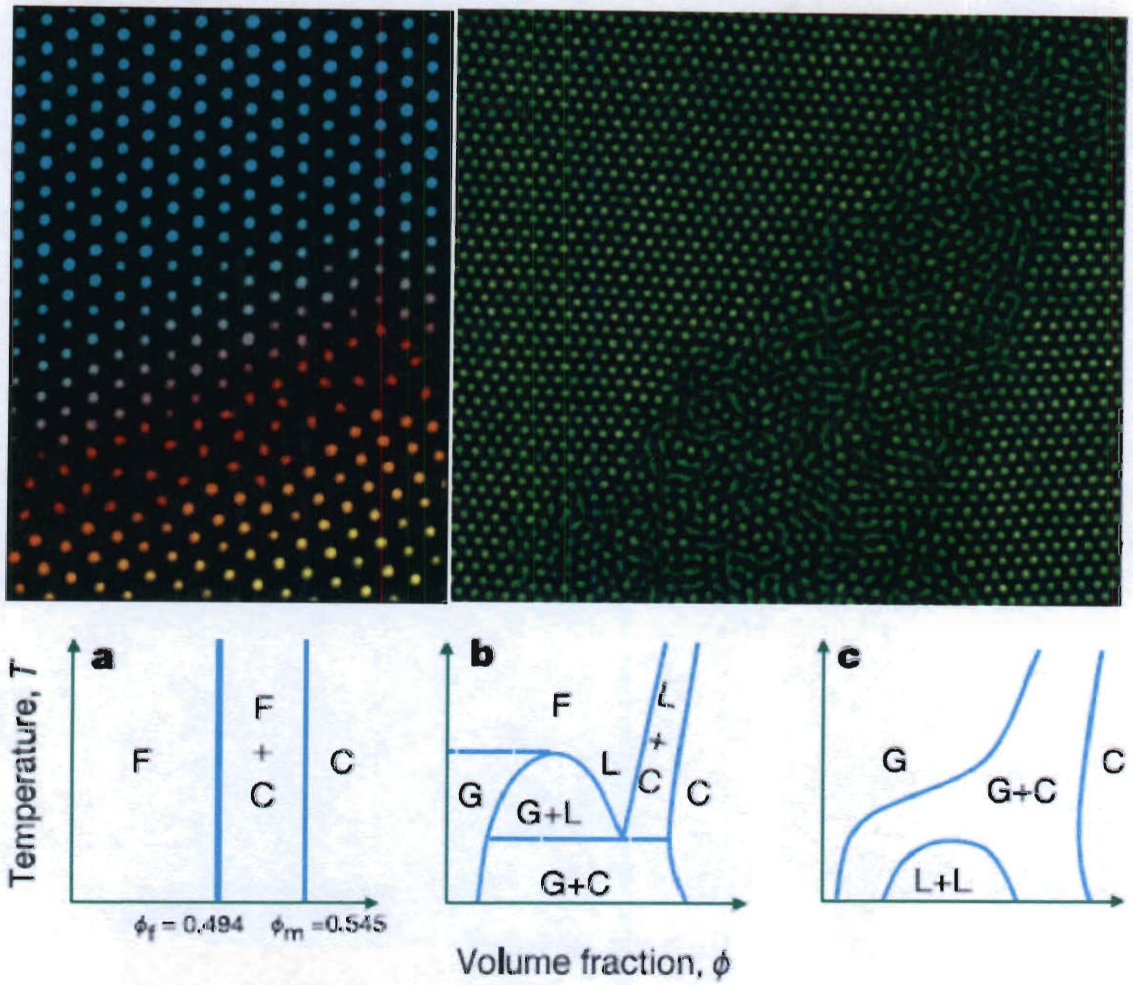

Figure 6.1. (Images adapted from reference 1) Top, Premelting of the colloidal crystal at a grain boundary. Left image, color indicates mean-square-displacement magnitude. Right image, showing the width of a premelting region. Bottom, a wide range of phase diagrams occurs naturally. a) For a purely hard-sphere system the phase diagram shows only fluid (F) and crystalline (C) phases. b) Atomic systems are often modeled by hard spheres with long-range attractions. This leads to equilibrium between gas (G), liquid (L) and crystal phases. c) In cases where the attraction is short-range, as in protein systems, equilibrium between gas and crystalline is found, but the liquid-liquid transition becomes metastable.

The virtuosity of colloidal model systems also lies in the range of dimensionalities that are experimentally feasible. With the help of confocal microscopy, colloids can be imaged in real-time in three dimensions[6]. They can also be confined in two dimensions by means of trapping at oil/water or air/water interfaces[7]. And confinement to one dimension has been realized by micron-scale channels[8] made using soft lithograph technology. The system developed in this chapter has the advantage of straightforward setup and easy manipulation compared with other two dimensional systems.

6.1.2. Melting in two dimensions

It is known for almost half a century that the density-density correlation function in a two-dimensional crystal decays algebraically to zero with distance[3, 9]. This is in stark contrast to the 3D case where a finite value is attained. Kosterlitz and Thouless[10] pointed out that the nature of the melting transition in 2D is different from 3D and suggested that crystal melting was a continuous transition mediated by the dissociation of dislocation pairs. Later it was shown that the resulting phase is not an isotropic liquid, but a hexatic phase, characterized by two order parameters: a short-range positional and a quasi-long-range orientational (sixfold) order[3, 4, 11]. A second transition induced by the formation of dislocations is necessary to drive the system from the so-called hexatic phase into the isotropic liquid phase[11, 12]. This two-stage melting scenario is referred to as the Kosterlitz-Thouless-Halperin-Nelson-Young theory (KTHNY). This theory predicts the temperature where the system becomes unstable and topological defects (dislocations or

disclinations) are formed. It predicts that in two dimensions, a hexatic phase exists between the solid and liquid phases, different from a simple first order transition from solid to liquid, as is typical in three-dimensional systems[3, 4]. Several computer simulations and experiments have been performed[3, 13], leading to inconsistent results. So far it seems that the melting scenario in 2D is not universal but depends on the specific properties of the systems[14]..

Despite the many simulation and experimental observations, the existence of the hexatic phase between solid and liquid phases, as well as its dependence on the types of pair interactions between particles continues to remain unclear[3, 4, 7, 15, 16]. There have been very limited experimental studies of the melting transition in two dimensions. Of these studies very few validate the KTHNY theory. Zahn and colleagues[9] have studied the equilibrium and dynamics of paramagnetic particles trapped at the air-water interface. By modulating the electric field which controls the particle interaction, they found a first-order transition from a fluid to a solid-like phase. A group led by Rice[17] have studied the melting process of colloidal particles confined between parallel plates (quasi-2D system), and found that poly(methylmethacrylate) particles undergo a melting process that is in agreement with the KTHNY theory, while silica particles simply undergo a solid-fluid transition. Lin and Chen[18] found a melting transition in agreement with a KTHNY scenario for charged polystyrene particles adsorbed at the decane-water interface. All these results suggest that the melting mechanism in a 2-D environment is highly dependent on the interaction potential between particles[7].

In this chapter, I present a novel two-dimensional experimental colloidal system to study phase behavior and dynamics. This system consists of an aqueous suspension of charged paramagnetic colloidal particles that are confined near a subtrate by gravity. The long-range attractive part of the pair potential between particle pairs is induced by a tunable high frequency magnetic field. The short-range repulsive part of the pair potential is a result of electrostatic interactions. First, I calibrate the system to validate inter-particle pair potentials. Then, I measure the phase transition properties and compare my experimental results with Monte Carlo and BD simulations.

6.2. Theory

6.2.1. Pair potential in DC magnetic field

In the presence of a DC magnetic field, the pair potential between a pair of charged paramagnetic spheres consists of two parts: i) short range electrostatic repulsion can be determined from DLVO theory:

$$U_{el} = \left(64\pi k_B T R \rho_\infty \gamma^2 / \kappa^2\right) \exp(-\kappa D) \qquad (6.1)$$

where kb is Boltmann's constant, T is temperature, R is the radius of the spheres, ρ_∞ is the number density of ions in the bulk solution, κ is the reciprocal of Debye length, $\gamma = \tanh\left(ze\psi_0 / 4k_B T\right)$ is the reduced potential, where ψ_0 is surface potential, and D is the distance between the surfaces; and ii) the long range magnetic attraction

$$U_{Mag}^{DC} = 1.202 \cdot 4/9 \cdot \pi \mu_0 \chi^2 H_0^2 R^6 \cdot \left(1 - 3\cos^2 \alpha\right) \cdot r^{-3} \tag{6.2}$$

where μ_0 is permeability of vacuum, χ is volumetric magnetic susceptibility of a sphere, H_0 is magnetic flux intensity, α is the angle between the magnetic field direction and the direction of the vector that connects the centers of the two spheres, and r is the distance between the two centers.

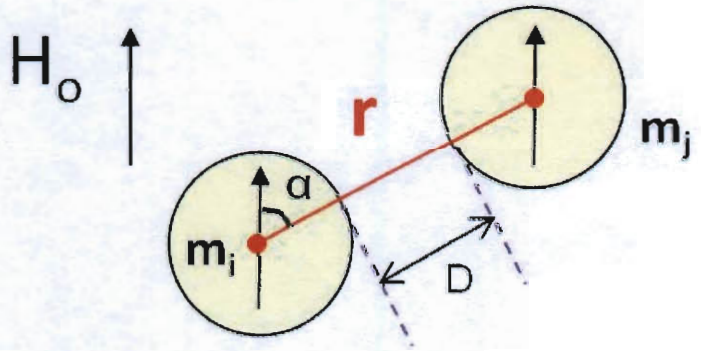

Figure 6.2. Skematic illustation of the definition of geometrical variables in this section.

The total pair potential in a DC magnetic field between two spheres of distance r in the direction of $\vec{r}$ is repulsion

$$U_{tot}^{DC} = U_{el} + U_{mag}^{DC} \tag{6.3}$$

with a torque in the direction perpendicular to $\vec{r}$ as

$$\Gamma_{mag}^{DC} = 1.202 \cdot 4/9 \cdot \pi \mu_0 \chi^2 H_0^2 R^6 \cdot \sin 2\alpha \cdot r^{-3} \tag{6.4}$$

that would eventually drive the pair to align in the direction of the external field.

6.2.2. Pair potential in rotational magnetic field

In the presence of a rotational magnetic field at high frequency, the time average of magnetic torque vanishes. First of all, the integration of Equation 6.4 with respect to α from 0 to 2π is zero. Secondly, the relaxation time for the magnetic torque is longer than hydrodynamic relaxation time at high frequencies. Similarly, integrating the DC magnetic potential with respect to α results in the time average (or effective) magnetic potential in a rotational field attraction:

$$U_{Mag}^{Rot} = \int_0^{\pi/2} U_{Mag}^{Rot} d\alpha = 1.202/18 \cdot \pi^2 \mu_0 \chi^2 H_0^2 R^6 \cdot r^{-3} \qquad (6.5)$$

It is obvious from Equation 6.5 that the effective magnetic potential at high frequencies is not a function of α; in other words, the magnetic potential U_{Mag}^{Rot} acts as an effective potential between particles in the direction of the connector vector. This means that the magnetic attraction has effectively the same nature as any other type of naturally incurred attractions (e.g. van der Waals or depletion attraction) in terms of directionality. Therefore, the total pair potential between paramagnetic colloidal spheres induced by rotational magnetic field

$$U_{tot}^{Rot} = \left(64\pi k_B T R \rho_\infty \gamma^2 / \kappa^2\right) \exp(-\kappa D) + 1.202/18 \cdot \pi^2 \mu_0 \chi^2 H_0^2 R^6 \cdot r^{-3} \qquad (6.6)$$

is a good model potential for two-dimensional phase behavior studies.

6.2.3. Frequency effect

A natural question to be raised at this point is "how high a frequency is high enough for the resulting pair potential to be considered effectively constant?" The idea is to determine a frequency threshold above which there is no effective magnetic torque and the center-to-center distance fluctuation between particles equals that of a particle pair under a static field. This frequency threshold can be determined by monitoring the motion of a particle pair under rotational magnetic field experimentally or by using a Brownian dynamics (BD) simulation. Here we present the results obtained by performing a BD simulation for a particle pair under a rotational magnetic field with a magnitude of 0.8mT at a variety of frequencies. It is determined from Figure 6.3 that the frequency threshold is 50Hz. Experimental data for the rotational diffusion at this frequency and above also confirms that the effective magnetic torque of the particle pair is negligible (data not shown). As a result, I use a 50Hz magnetic field in the experiments and simulations described in this chapter.

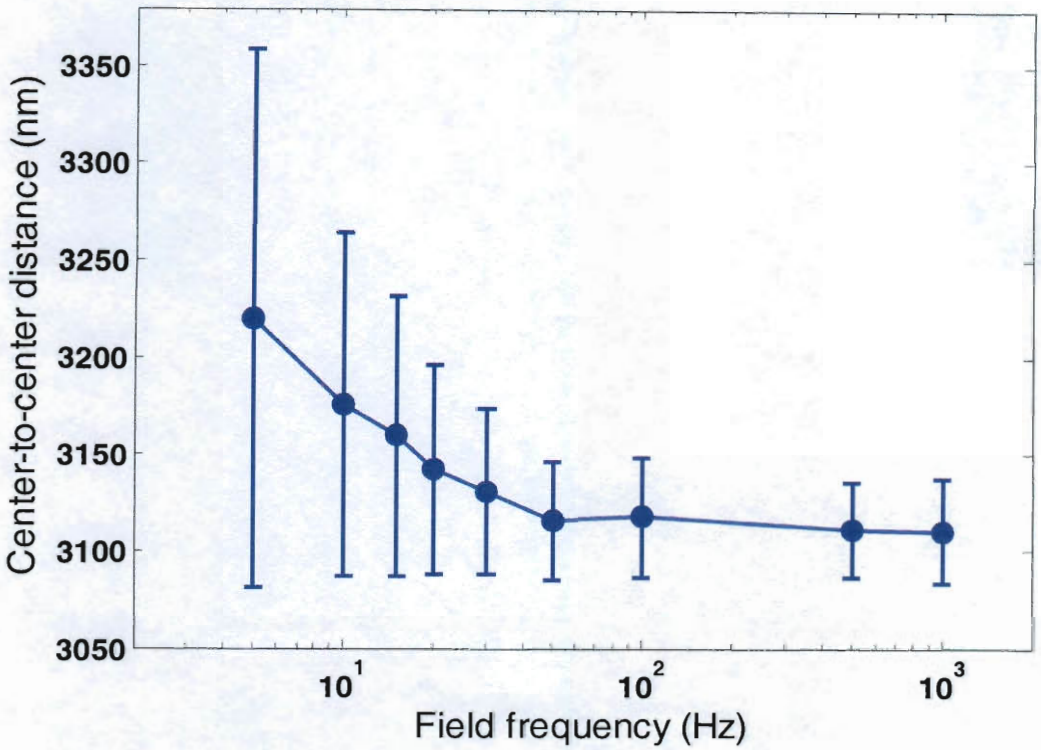

Figure 6.3. Frequency dependence of the particle pair center-to-center distance at a field magnitude of 0.8mT.

6.3. Methods and materials

6.3.1. Experimental magnetic and imaging system setup

The experimental magnetic coil system is setup in such a way to provide a uniform rotational magnetic field to the sample. Two pairs of air-core solenoids are placed perpendicular to each other (Figure 6.4) with each generating orthogonal magnetic field. A multifrequency power supply (Agilent N6784A) is programmed to provide sinusoidal

currents through the coils to create a magnetic field in the x-direction $H_x = H_0 \sin(\omega t)$, and in the y-direction $H_y = H_0 \sin(\omega t + \pi/2)$. This results in a homogeneous magnetic field that rotates in the horizontal plane. The instantaneous direction of the field is monitored using a digital oscilloscope embedded in the power supply mainframe (Agilent N6705A). A 100x / 1.2 N.A. oil immersion objective is mounted at the center of the two pairs of solenoids, beneath the sample holder. A dichroic mirror in the light path and a CCD camera (Hamamatsu) are used to capture the images. We monitor and record the colloid dynamics at a rate of 10 frames/sec using Simple PCI software. The images are processed using MATLAB (refer to Chapter 3 for details regarding image processing) where the x and y coordinates of spheres, density and structure of the system, and the radial distribution functions could be obtained.

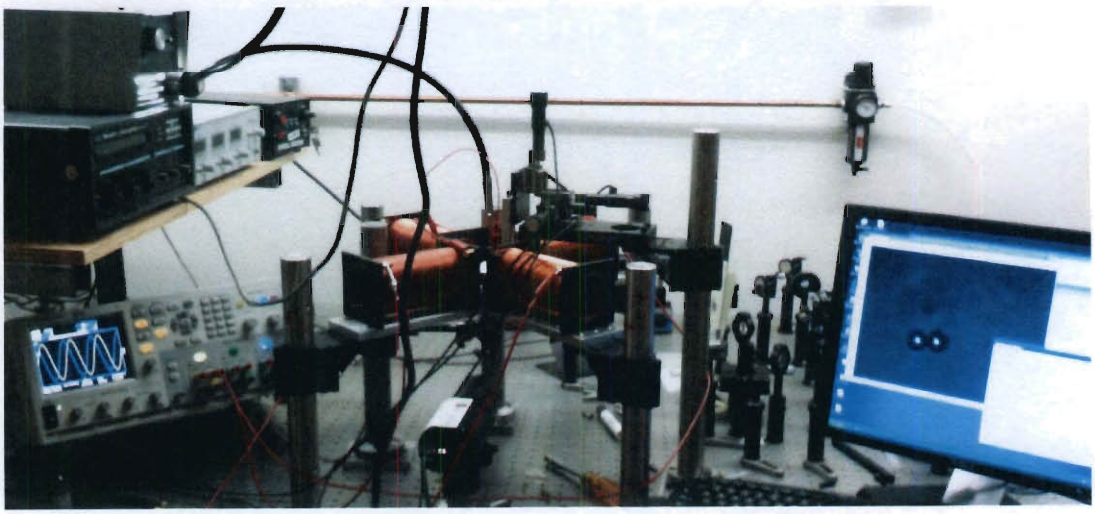

Figure 6.4. Experimental magnetic solenoids and imaging system demostration.

6.3.2. Sample preparation

The particles used in this study are carboxyl-coated paramagnetic polystyrene M-270 Dynabeads (Dynal Biotech, Oslo, Norway). The mean particle diameter of the particles is 3.02 ± 0.08 μm, confirmed by dynamic light scattering and scanning electron microscopy (SEM) measurements. The magnetic susceptibility of the particles varies from 0.84 to 0.29 in the field range of 0.1 mT to 50 mT, as provided by the manufacturer. The particles are taken from a stock solution, washed and sonicated in 1mM sodium chloride solution, and diluted to a variety of final particle concentrations from 0.01wt% to 1wt%. The zeta potential of the particles is measured to be -50.0 mV in 1 mM salt solution. The particles are injected in a flow cell consisting of two glass coverslips sandwiched together with double-stick tape. The coverslips are washed in a solution of sulfuric acid and hydrogen peroxide (7:3 v/v) prior to experiments to prevent the particles from sticking to the glass surface. The cell is then sealed with epoxy to prevent evaporation of the solution. The seal is stable for over a month. The cell is then placed on the sample holder at the center of the solenoids. Five minutes is allowed for all the spheres to sediment to the bottom of the flow cell and reach equilibrium before any experimental operations or observations are made.

6.3.3. Experimental methods

6.3.3.1. Pair potential calibration

To better understand the interactions between these paramagnetic colloidal spheres, the pair potential profiles at different magnetic field strengths, H_0 (0.31mT, 0.46mT, 0.62mT and 0.78mT), is used to calibrate the systems. First, a very dilute (0.001wt %) particle suspension is prepared and loaded into the flow cell and placed under the sample holder as described in Chapter 3. Then, a rotational magnetic field is applied and an isolated pair of spheres is located. To capture the phase behavior, ~1000 frames of images are recorded at a speed of 1frame/sec. The images are subsequently analyzed in MATLAB to provide the inter-particle distance r and the pair potential data is computed by inverting the Boltzmann distribution:[19]

$$\frac{U(r)-U(r_{ref})}{k_BT}=\ln\left[\frac{n(r_{ref})}{n(r)}\right] \tag{6.7}$$

where the largest of r is set to be r_{ref} and the corresponding reference potential $U(r_{ref})$ is set to be zero. From Equation 6.7, the pair potential $U(r)$ at a given magnetic field strength is determined experimentally and compared with theoretical calculations in section 6.4.1.

6.3.3.2. Experimental Measurements Used to Construct a Phase diagram

To determine the experiemental data points in the phase diagram, I measure the densities of different phases and their radial distribution function(RDF) and bond-orientation correlation function (BOCF) at equilibrium. For each experiment, I allow at least 8 hours before equilibrium is considered reached, the criteria of which is that the phase separation is on macroscopic scale (O(1mm)) and that the densities within each phase are uniform. Once each system is considered to be in equilibrium, I record the ~100 images of each phase. The images are subsequently processed in MATLAB (codes are provided in Appendix E) to analyze their structures using RDF and BOCF and determine their densities and state.

The expression to compute the RDF is given as

$$g(r) = \frac{A}{\pi r N} \sum_{i} \sum_{i \neq j} \delta(r - r_{ij}) \tag{6.8}$$

with N being the total number of particles within the image, A is the total area counted in the image and $\delta(r - r_{ij})$ is the Dirac delta function. The BOCF is computed using

$$g_6(r) = \frac{\left\langle \left| \psi_6^*(0) \psi_6(r) \right| \right\rangle}{g(r)} \tag{6.9}$$

with the bond-orientation parameter $\psi_6(r)$ computed as

$$\psi_6(r_i) = \frac{1}{6} \sum_{j=1}^{6} \exp(6i\theta_j(r_i)) \tag{6.10}$$

where $\theta_j(r_i)$ is the angle between an arbitrary (fixed) axis and the line connecting particle i with its j^{th} neighbor; two particles are neighbors if they share a Voronoi cell edge[2]. In the Kosterlitz-Thouless-Halperin-Nelson-Young (KTHNY) theory, g6(r) approaches a constant in crystal (long-ranged order), decays algebraically in hexatic phase (quasi-long-ranged order), and decays exponentially in liquid phase (short-ranged order)[3,4,15].

6.3.4. Simulation methods

6.3.4.1. Brownian Dynamics simulation

A Brownian dyanmics (BD) simulation is used to simulate the motion of an ensemble of spheres in 2-D is based on the algorithm described in detail in Chapter 3. The main difference is the addition of a magnetic dipole-dipole force between particle pairs and the absence of metric, bending and constraint forces used to describe particles within a chain. Thus, the equation of motion changes into

$$m_i \frac{d^2\mathbf{r}_i}{dt^2} = \mathbf{F}_i^{Mag} + \mathbf{F}_i^{hydro} + \mathbf{F}_i^{Brown} + \mathbf{F}_i^{ele} \qquad (6.11)$$

where for the i^{th} bead, m_i is the mass of the i^{th} bead (the left-hand-side inertia term is negligible compared with right-hand-side terms in the case of low Reynolds number), $\mathbf{r}_i$ is the position, $\mathbf{F}_i^{hydro}$, is the hydrodynamic drag force, $\mathbf{F}_i^{Brown}$, is the stochastic Brownian

force, $\mathbf{F}_i^{mag}$, is the magnetic dipole-dipole force that is dependent on time, magnetic field strength and frequency, and $\mathbf{F}_i^{ele}$, is the electrostatic force between beads.

In these BD simulations, time steps are from 0.001ms to 0.1ms, and the initial particle positions are manually assigned to be within vicinity of each other. (MATLAB code of the main program and subroutines are provided in Appendix C)

6.3.4.2. Monte Carlo simulation

To roughly determine phase coexistence curves in this two-dimensional system, I use Metroplis Monte Carlo (MC) simulation of 256 spheres in NVT ensemble (FORTRAN codes provided in Apendix D). In this MC simulation, the spheres start from a FCC lattice and 10.5 million steps are allowed for system to reach equilibrium before any statistics are calculated. Periodic boundary conditions are used to mimic bulk behavior and pair potentials are used from Equation 6.6. After the system reaches equilibrium, we collect position information of the spheres at 100-step intervals to compute the radial distribution function and average over 0.5 million steps to get the statistics. Chemical potential is computed using Widom particle insertion method[20] and pressure from virial expansion using radial distribution function

$$P = \rho k_B T - \rho^2 / 3 \int_0^\infty r g(r) U'(r) \cdot 2\pi r dr \qquad (6.12)$$

with ρ being the number density (coverage) of spheres scaled with diameter squared. For each simulation, a density and potential well depth are assigned, and the chemical

potential and pressure are computed if the equilibrium phase is homogenous. However, if there is phase separation, the system is inhomogeneous and thermodynamic properties cannot be computed. Thus, densities of each phase are computed and two points on two phase-coexistence curves are located.

Since this simulation involves phase separation in a micro-system where interfacial tension effects are not included, the phase diagram constructed using this MC simulation can only be seen as a guide to the true theoretical phase diagram. Better ways to simulate gas-liquid coexistence would be to use a Gibbs ensemble method and there are numerous advanced techniques to simulate liquid-solid coexistence (discussed in detail in Chapter 7).

6.4. Results and discussions

6.4.1. Pair potential calibration

The pair potentials of magnetic particles under rotational magnetic field are quantified by observing the inter-particle distance change in the particle pair using the inverse Boltzmann distribution (Equation 6.7). Ideally, one needs to allow infinite long time for the particle pair to sample all possible inter-particle distances. In real experiments, it is difficult to do so because 1) for weak-attraction pairs (potential on the order of k_BT), they are usually trapped in the potential well for a very short period of time before parting each other; and 2)for strong-attraction pairs (potential close to or larger than 10 k_BT), they usually spend too much time in the potential well making it difficult to fully capture the shape of the rest of the pair potential curve. In this section, I experimentally measure

pair potentials at two different magnetic field strengths, corresponding to a theoretical pair potential well depth of 2.7 and 5 k_BT. These moderate attraction potentials allow the particle pair to spend enough time in the potential well to get good statistics and sample enough inter-particle distances to provide a complete pair potential profile.

It is obvious from the inter-particle distance histograms in Figure 6.5 a and c that the particle pairs spend more time closer together than farther apart. This time increases as the potential well depth is deeper (Figure 6.5c). After the inverse of the Boltzmann distribution (Equation 6.7), the histograms are converted to pair potentials and compared with theoretical profiles computed using the corresponding magnetic field strengths. The experimental pair potential profiles match reasonably well with theoretical profiles (Figure 6.5b and d). The roughness in the experimental data is attributed to the relatively short time or recording (15 minutes) and lack of statistical points (~1000 data points in the histogram).

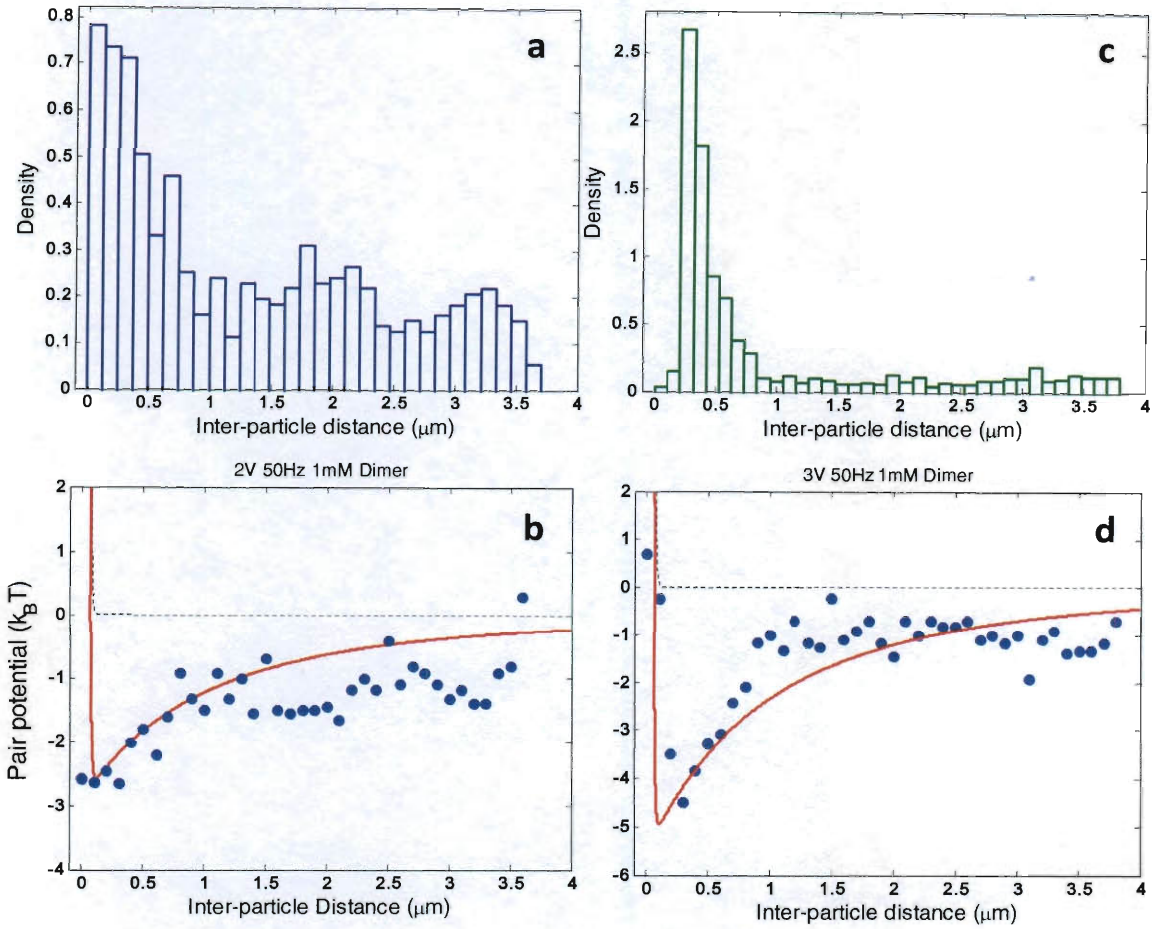

Figure 6.5. Experimental pair potential calibrations. a and c are inter-particle distance histograms of a particle pair (~1000 frames); b and d are pair potential obtained from a and c, respectively, by inversion of Boltzmann distribution using Equation 6.7. Magnetic field frequency is 50Hz and field strengths are 0.31mT for a,b and 0.47mT for c,d.

6.4.2. Radial distribution function

One of the most important properties of a thermodynamic equilibrium system is its radial distribution function g(r). Important thermodynamic quantities such as pressure and virial coefficient can be computed using g(r), which also lead to constructing the equation of

state of the system. The 2D colloidal system is ideal to provide g(r) information for the images taken at any regoin of interest (Matlab code provided in Appendix E). The radial distribution functions of representative phases are shown in Figure 6.6.

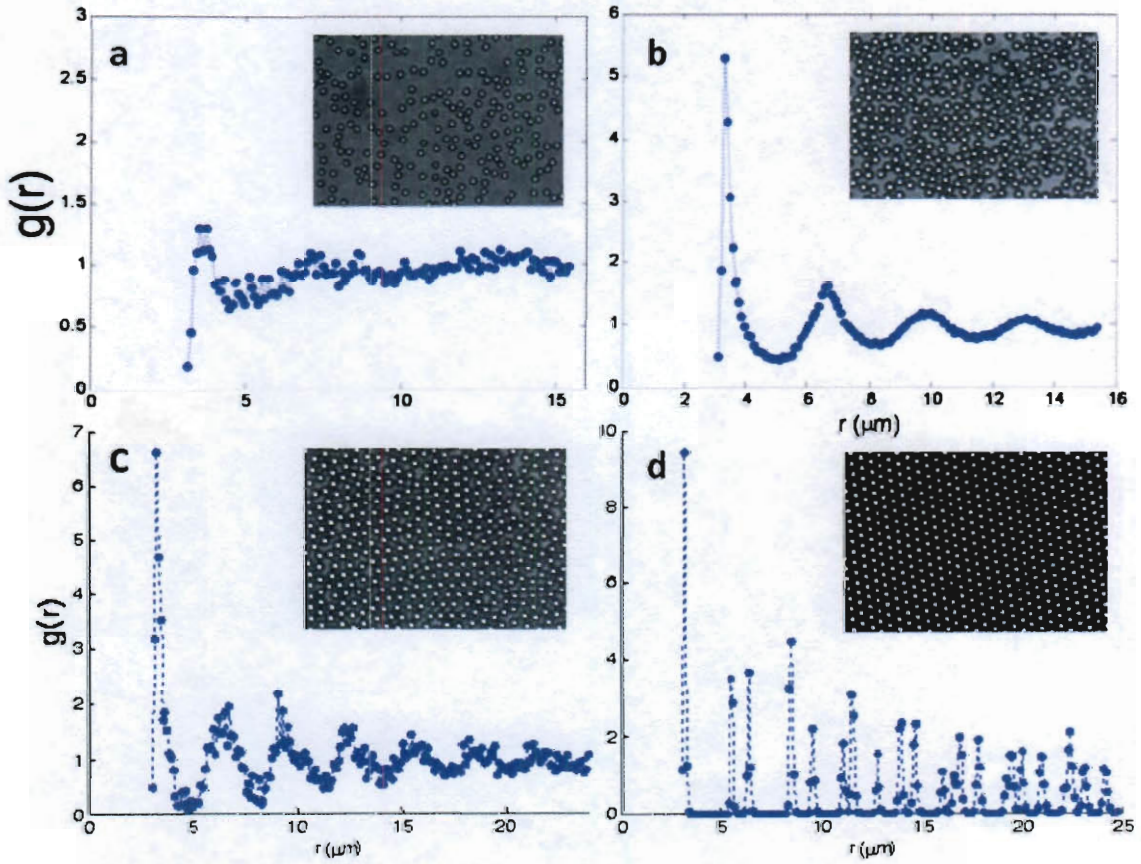

Figure 6.6. Experimental radial distribution functions (RDF) of different phases. a) Gas; b) Liquid; c) Hexatic; d) Solid. The g(r) values are averaged over data from 10~100 image frames. Insets are snapshots of small regions of the real images analyzed.

For a dilute gas phase (Figure 6.6a inset), the g(r) increases from zero to unity at around one sphere diameter and remains near unity for larger distances. The isotropic nature of equilibrium particle locations indicate a dilute gas phase. For a liquid phase (Figure 6.6b inset), the g(r) has damped periodic profile as predicted by theory. For hexatic phase (Figure 6.6c inset), the equilibrium structure has both crystal grains and liquid-like regions, thus the g(r) has a combined feature of a liquid-like wavy shape as well as crystal-like spikes at certain distances. For a crystal solid phase (Figure 6.6d inset), the g(r) has spikes at certain distances but vanishes elsewhere, indicating the high regularity of the lattice arrangement.

6.4.3. Bond-orientation correlation function

According to the Kosterlitz-Thouless-Halperin-Nelson-Young (KTHNY) theory, the bond-orientation correlation function g6(r) approaches a constant for crystals (long-range order), decays algebraically for hexatic phases (quasi-long-range order), and decays exponentially for liquids (short-range order). The g6(r) can be accurately measured in my colloidal system and the above argument can serve as criteria for determining the state of a phase.

From the experimental images of different equilibrium phases, the computation of g6(r) can be performed (Section 6.3.3.2) on three representative images. A black solid line in Figure 6.7 corresponds to the inset image of Figure 6.6d; a red solid line corresponds to the inset image of Figure 6.6c; and a green solid line corresponds to the inset image of Figure 6.6b. The regularity of particle arrangement in the Figure 6.6d inset is obvious to

the eye and it is also confirmed by g6(r) measurements where its value approaches a constant 0.85. It can also be seen in the Figure 6.6c inset that the existence of crystal grains amid less regularly aligned spheres, indicating a hexatic phase. This is again confirmed by the algebraical decay in g6(r) value with a power-law factor of -1/4. The match between the g6(r) of liquid phase profile to an exponential decay is not as good as the other two phases. This might be caused by either a lack of sufficient images to give average values of g6(r) since only one image is analyzed to give the the green curve; or it may be that the distance range of g6(r) measured is not long enough for the trend to be clear.

The experimental results (Figure 6.7, red lines) clearly show the existence of hexatic phase in the system. In addition, the difference in the slope of g6(r) profiles can serve as criterion for determining wether a phase is liquid or solid or hexatic, which is important in constructing a experimental phase diagram of the system.

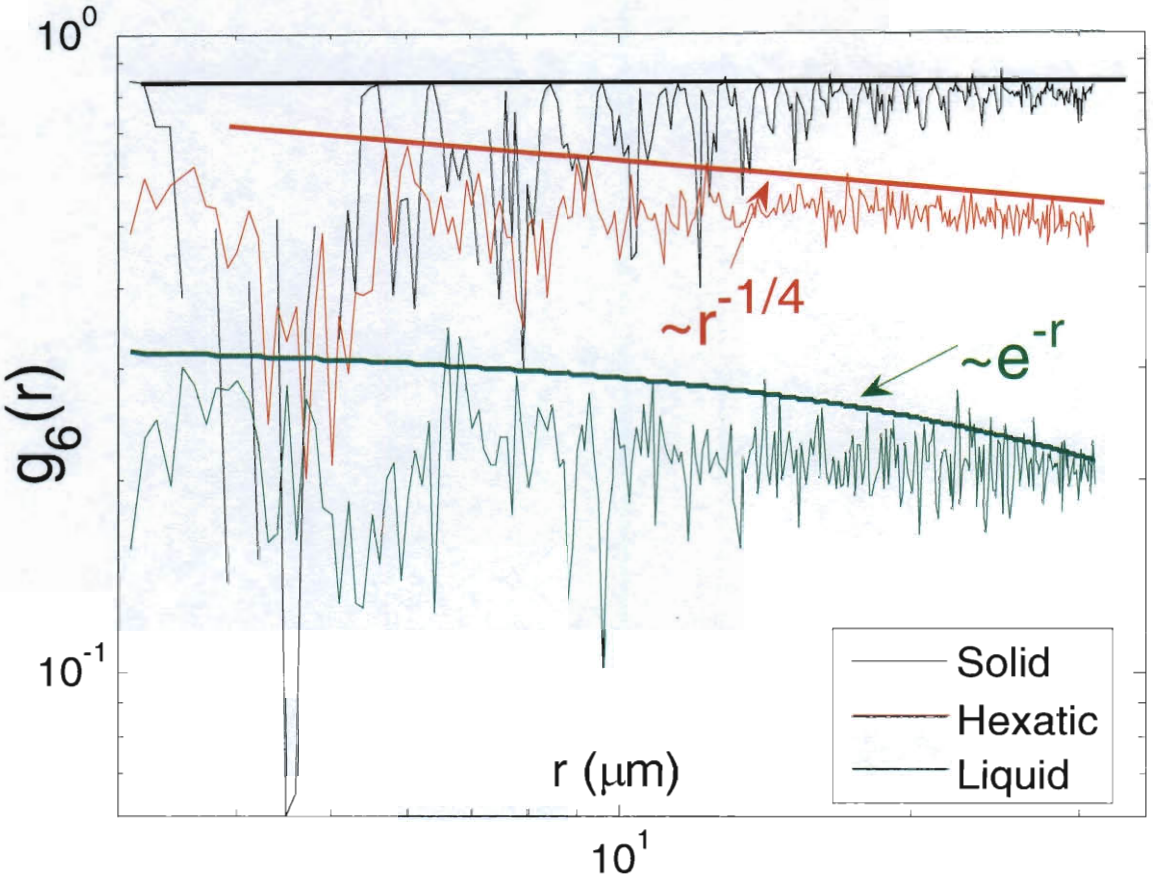

Figure 6.7. Experimental bond-orientation correlation functions (BOCF) of different phases. The black solid line represents the cystalline or solid phase where the g6(r) value approaches a constant close to unity. The red solid line is the hexatic phase where the g6(r) value decays algebraically with the power-law factor of -1/4, matching with KTHNY scenario. The green solid line is liquid where g6(r) values are small in magnitude and decays exponentially. All the dashed lines are trend lines to guide the eye.

6.4.4. Phase diagram

To quantify the equilibrium phase behavior of the 2D system at different conditions, I have constructed an experimental phase diagram which is then compared with results from Monte Carlo simulations. In each experiment, I fix the 2D particle density and magnetic field strength (pair potential well depth) and allow the system to equilibrate. When it equilibrates, I measure the density of each bulk phase and use the g6(r) profile to determine the state of the phase. So each experiment provides one density in one-phase region, two densities in the three two-phase regions, and three densities at the triple point (Figure 6.8 the sharp peak on the blue line).

Experimentally, the gas-solid, gas-liquid, solid-liquid coexistence at equilibrium have been observed but I have not observed the three phase coexistence. Experiments under the same conditions have been carried out several times and have shown reproducible equilibrium densities with minimum error bars (Figure 6.8).

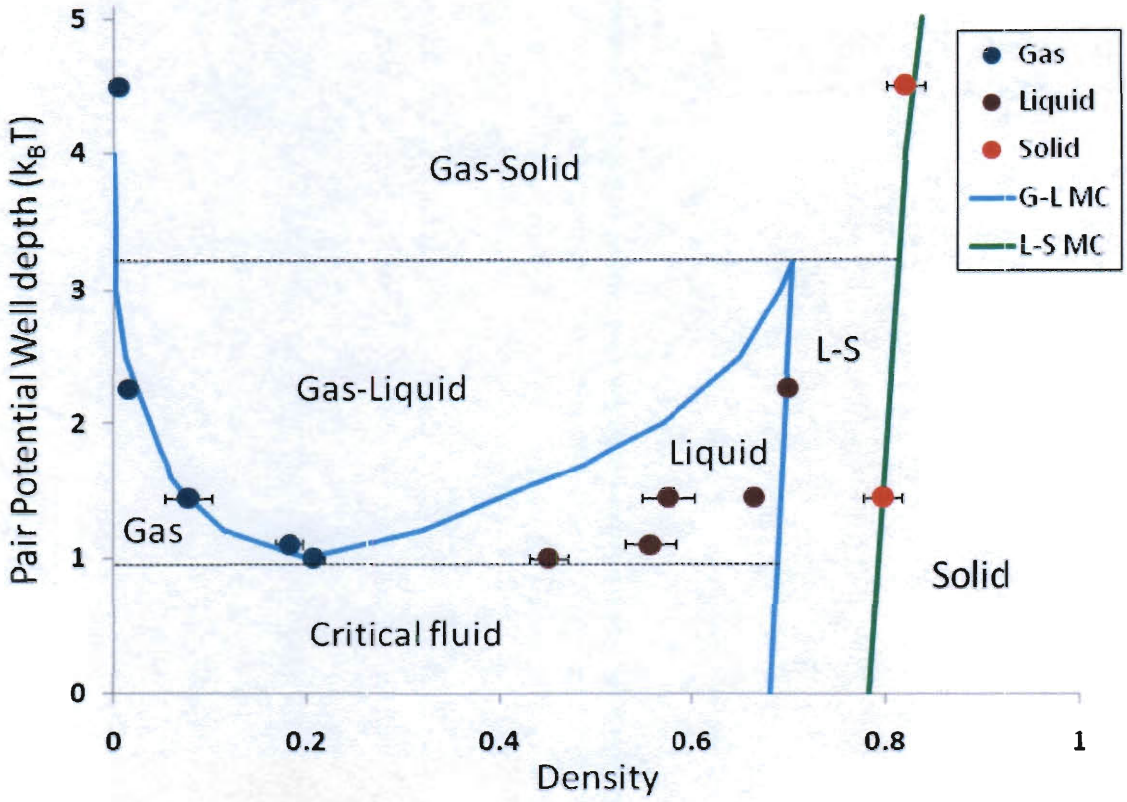

Figure 6.8. Computational phase diagram of the 2D system and experimental data. Blue and green curves are gas-liquid and liquid-solid coexistence curves computed using Monte Carlo simulation described in Section 6.3.4.2. Experimental data include gas, liquid and solid densities at equilibrium at different pair potential well depths and the horizontal error bars indicate the uncertainties in density measurement.

The agreement between the experimental data and the Monte Carlo simulation curves are good for the gas and solid phases while the liquid densities deviate substantially from the simulation results. This may be due to the fact that the NVT ensemble Monte Carlo simulation used in obtaining this phase coexistence curve is unrealistic since the small

system phase separates in the simulation box, creating interfaces, making the computed results erroneous. Another possible reason is that the pair-wise additivity assumption in the MC simulation may break down when the system increases its density (this assumption is only strictly valid at the dilute gas extreme). Both causes should be carefully examed and I expect interesting discoveries in the course of investigating the mismatch of the experimental data and the simulation results in the phase diagram.

6.5. Conclusions

In this chapter I have demonstrated the feasibility of using magnetic colloidal spheres and a rotational magnetic field to create a system with tunnable pair potentials to study phase transitions in two dimensions. Important statistical mechanics quantities such as radial correlation function and bond-orientation correlation function are conveniently obtained via image processing and computation. A phase diagram is mapped out experimentally and compared with Monte Carlo simulation results. I believe this system provides an ideal platform to study phase behavior, dynamics and melting in two dimensions.

6.6. Reference

1. Anderson, V. J.; Lekkerkerker, H. N. W., Insights into phase transition kinetics from colloid science. *Nature* **2002,** 416, 811-815.
2. Alsayed, A. M.; Islam, M. F.; Zhang, J.; Collings, P. J.; Yodh, A. G., Premelting at defects within bulk colloidal crystals. *Science* **2005,** 309, (5738), 1207-1210.
3. Strandburg, K. J., Two-dimensional melting. *Reviews of Modern Physics* **1988,** 60, (1), 161-207.
4. Gast, A. P.; Russel, W. B., Simple ordering in complex fluids - Colloidal particles suspended in solution provide intriguing models for studying phase transitions. *Physics Today* **1998,** 51, (12), 24-30.
5. Zahn, K.; Lenke, R.; Maret, G., Two-Stage Melting of Paramagnetic Colloidal Crystals in Two Dimensions. *Physical Review Letters* **1999,** 82, (13), 2721.
6. Lu, P. J.; Zaccarelli, E.; Ciulla, F.; Schofield, A. B.; Sciortino, F.; Weitz, D. A., Gelation of particles with short-range attraction. *Nature* **2008,** 453, (7194), 499-U4.
7. Bonales, L. J.; Rubio, J. E. F.; Ritacco, H.; Vega, C.; Rubio, R. G.; Ortega, F., Freezing Transition and Interaction Potential in Monolayers of Microparticles at Fluid Interfaces. *Langmuir* **2011,** DOI: 10.1021/la104917e.
8. Chou, C. Y.; Eng, B. C.; Robert, M., One-dimensional diffusion of colloids in polymer solutions. *Journal of Chemical Physics* **2006,** 124, (4).
9. Zahn, K.; Lenke, R.; Maret, G., Two-stage melting of paramagnetic colloidal crystals in two dimensions. *Physical Review Letters* **1999,** 82, (13), 2721-2724.
10. Kosterlitz, J. M.; Thouless, D. J., Ordering, metastability and phase-transitions in 2 dimensional systems. *Journal of Physics C-Solid State Physics* **1973,** 6, (7), 1181-1203.
11. Nelson, D. R.; Halperin, B. I., Dislocation-mediated melting in two dimensions. *Physical Review B* **1979,** 19, (5), 2457.
12. Young, A. P., Melting and the vector Coulomb gas in two dimensions. *Physical Review B* **1979,** 19, (4), 1855.
13. Strandburg, K. J., *Bond-Orientational Order in Condensed Matter Systems*. Springer: New York, 1992.
14. Saito, Y., Melting of Dislocation Vector Systems in Two Dimensions. *Physical Review Letters* **1982,** 48, (16), 1114.
15. Peng, Y.; Wang, Z.; Alsayed, A. M.; Yodh, A. G.; Han, Y., Melting of Colloidal Crystal Films. *Physical Review Letters* **2010,** 104, (20), 205703.
16. Naidoo, K. J.; Schnitker, J.; Weeks, J. D., 2-Dimensional melting revisited - Molecular dynamics simulations initiated with optical microscopy data. *Molecular Physics* **1993,** 80, (1), 1-24.
17. Zangi, R.; Rice, S. A., Nature of the transition from two- to three-dimensional ordering in a confined colloidal suspension. *Physical Review E* **2000,** 61, (1), 660-670.
18. Lin, B. J.; Chen, L. J., Phase transitions in two-dimensional colloidal particle system observed in Langmuir trough. *Colloids and Surfaces a-Physicochemical and Engineering Aspects* **2006,** 284, 239-245.
19. Wu, H. J.; Everett, W. N.; Anekal, S. G.; Bevan, M. A., Mapping patterned potential energy landscapes with diffusing colloidal probes. *Langmuir* **2006,** 22, (16),

6826-6836.
20. Frenkel, D.; Smit, B., *Understanding Molecular Simulations*. 2 ed.; Academic Press: New York, 2001; Vol. 1, p 663.

Chapter 7

Proposed future work

In this chapter I propose both theoretical and experimental work that will further our insights into fundamental colloidal dynamics and applications of magnetic colloidal particle assemblies. First, I propose to use the repulsive force probe technique described in chapter 5 to capture amyloid fibril growth dynamics. Then, I propose to perform more detailed Monte Carlo simulations to completely capture the phase diagram of the two-dimensional magnetic sphere system under an AC field. I also propose to experimentally research the longstanding question of occurrence of hexatic phase in 2D melting. Lastly, I propose to use DNA-linked magnetic chains in patterned microfluidic devices to study diffusion of polymers in confined geometry. Subsequently, I propose to engineer the magnetic particle chains with uniform length by synthesizing them in emulsions. Finally, the magnetic particle chains are proposed to be used as microrheometers to probe viscoelastic properties of complex fluids.

7.1. Repulsive force probe to understand amyloid fibril growth and aggregation

In nature, a range of polypeptide sequences can adopt an alternative highly organized state commonly known as an amyloid fibril[1,2]. These elongated aggregates are highly anisotropic, composed of a number of intertwining protofilaments, and possess an ensemble of common chemical and structural properties. These structures can result from aberrations in the normal protein folding process and are hence involved in a range of human disorders, including Alzheimer's disease and late onset diabetes[2,3]. In the Chapter 5, I have demonstrated a technique to measure repulsive forces between colloidal surfaces. In this section, I propose that this technique can be used to study the growth dynamics of amyloid fibrils with the advantage of simultaneously capturing an ensemble of individual fibrils growth rate, and relating the stalling forces, which are the counteracting forces required to stop the growth of a fibril, to their growth kinetics. This technique may help uncover unknown amyloid fibril growth kinetics at its early oligomers stage, where length scales between 10~200 nm are common.

The proposed experimental scheme (Figure 7.1) is as follows. First, the streptavidin-coated non-fluorescent magnetic particles are conjugated with biotin Aβ-40 monomers. Then, they are mixed with fluorescent magnetic particles of the same size without surface functionalization at 1:1 ratio. Additional Aβ-40 monomers are subsequently added to the binary dispersion. Finally, the sample is injected immediately into a flow cell and placed under uniform magnetic field to be imaged.

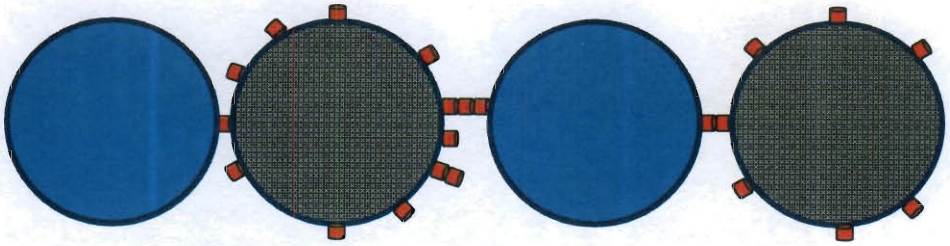

Figure 7.1. Schematic of the experimental system described in this section. Blue spheres represent fluorescent magnetic particles without any surface functionalization. Dark spheres represent Aβ-40 coated magnetic particles. Red cylinders represent Aβ-40 monomers. The size ratio of Aβ-40 monomer to magnetic particle is not to scale.

Preliminary results of a single chain indicates an average linear growth for lengths less than 70 nm followed by a stalling force of 1 pico-Newton(Figure 7.2). However, length increments at individual particle pair level are less regular. Future investigations are needed to better understand the role played by monomer concentration and the stalling force on Amyloid oligomers growth with better statistics.

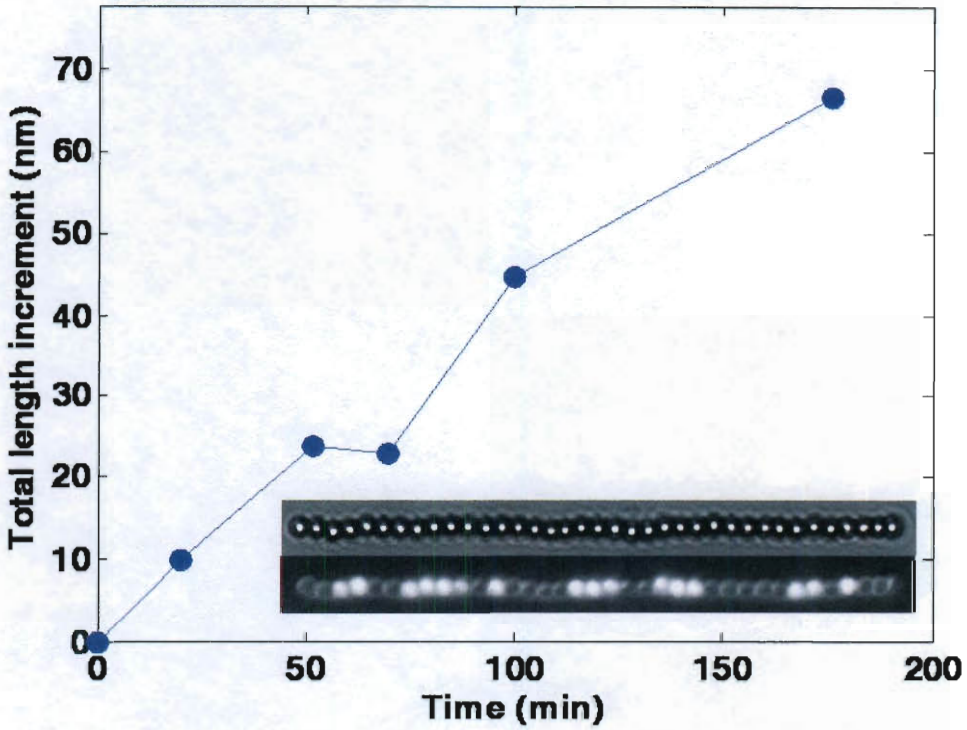

Figure 7.2. Aβ-40 growth kinetics data from a single chain experiment. The data (blue circles) are averaged increments over all the fluorescent/non-fluorescent particle pairs; upper inset, bright field image of the particle chain under uniform magnetic field; lower inset, fluorescent image of the same chain.

7.2. Monte Carlo simulation

In chapter 6, I have proposed colloidal model system to study two-dimensional phase behavior. There is wide spectrum of phenomena that this system is an ideal candidate to study. In this section, I propose computational and experimental investigations to probe the two-dimensional phase behavior.

7.2.1. Monte Carlo simulation

In chapter 6, Monte Carlo in NVT ensemble is correct when the system does not phase separate within the simulation box. Once it does, interfaces form causing the simulation to become inaccurate. In this section, I propose two other Monte Carlo simulation schemes to simulate the system more accurately.

7.2.1.1. Grand-canonical ensemble for gas-liquid transition

At phase coexistence temperature and density, there are usually interfaces between two phases whose properties are different from those in bulk. To better capture gas-liquid equilibrium structure without introducing any interface, I propose the grand-canonical ensemble Monte Carlo simulation method[4] (or μVT ensemble). In this ensemble, the temperature, volume, and chemical potential are fixed. Two simulation boxes in which one is gas phase and the other liquid phase are allowed to fluctuate in number of particles till equilibrium is reached between two boxes. The simulation technique is quite easy to implement and a pseudo-algorithm can be found in reference 4.

7.2.1.2. NPT ensemble for solid-liquid transition

To better capture solid-liquid equilibrium structure without introducing any interface, I propose the isobaric-isothermal ensemble Monte Carlo simulation method[4] (or NPT ensemble). It is conveniently used in the vicinity of a first-order phase transition because at constant pressure, the system is free to transform completely into the state of lowest

Gibbs free energy, whereas in a NVT ensemble the system may be kept at a density where it would like to phase separate into two bulk phases of different densities but is prevented from doing so by finite-size effects.

In each NPT ensemble simulation, a temperature is assigned and an equilibrium density is obtained at the end. By plotting the system density vs. temperature plot after a number of simulations, transitioning temperature and densities can be obtained and two data points on the solid-liquid coexistence curve are obtained. This process can be repeated for different pair interaction potentials and would allow the computation of a more complete solid-liquid coexistence curve.

7.2.2. Melting in two dimensions

As discussed in Chapter 6, despite the many simulation and experimental observations, the existence of hexatic phase between solid and liquid phase regions, as well as its dependence on types of pair interactions remains an open question to date[5-9]. There have been very limited experimental studies of the melting transition in two dimensions, and only validate the KTHNY theory for some systems. Zahn and colleagues[10] have studied the equilibrium and dynamics of paramagnetic particles trapped at the air-water interface. By modulating the electric field (the interaction), they found a first-order transition from a fluid to a solid-like phase. A group led by Rice[11] have studied the melting process of poly(methylmethacrylate) and silica particles confined between two walls (quasi-2D systems) and found that in the first system the melting process is in agreement with the KTHNY theory, while in the second it is a first-order solid-fluid transition. Lin and Chen[12] found a melting transition in agreement with a KTHNY scenario for charged

polystyrene particles adsorbed at the decane-water interface. All these results suggest that the melting mechanism seems to depend on the interaction potential between particles trapped in the 2D or quasi-2D environment[9].

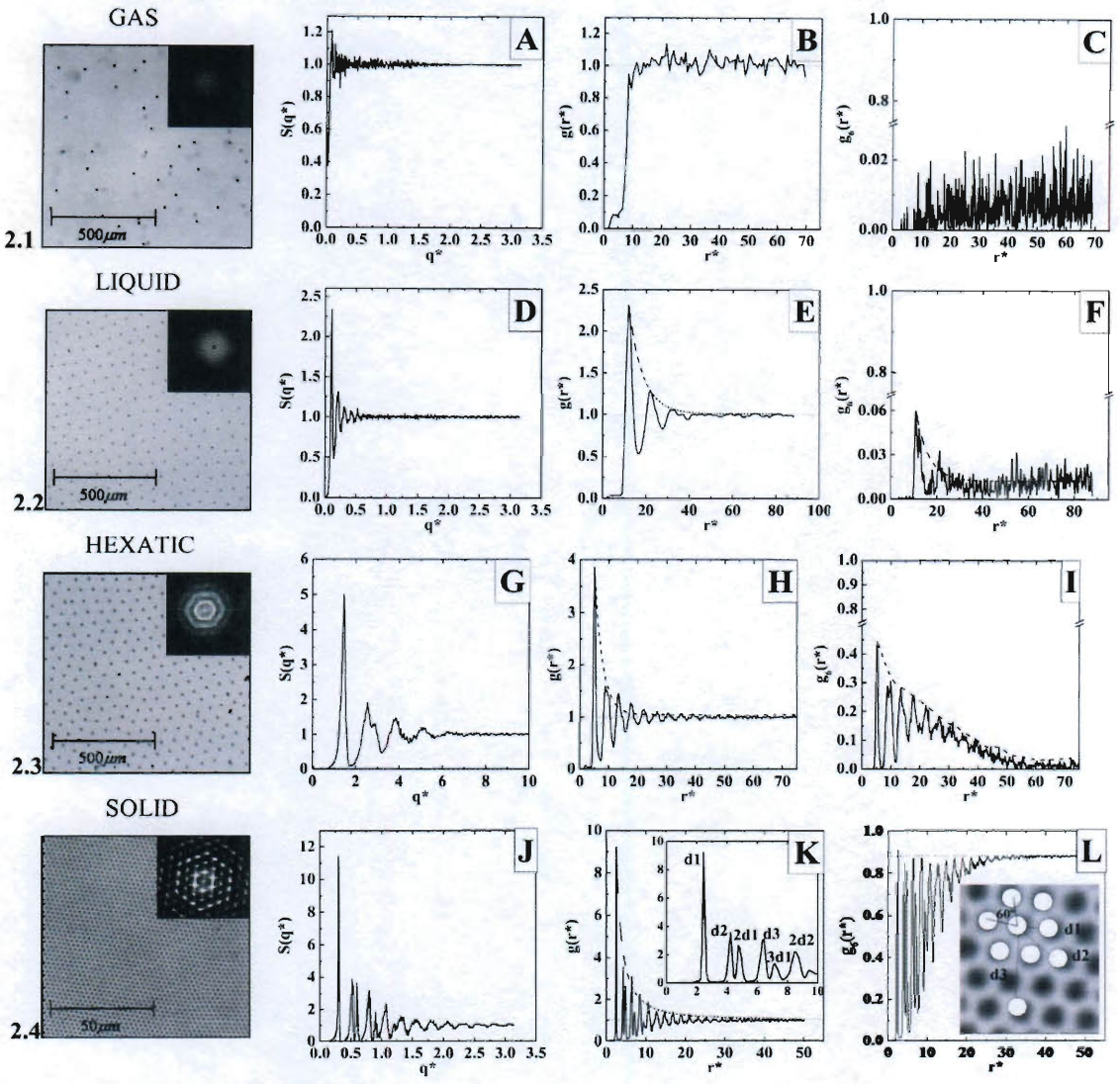

Figure 7.3. (Images adapted from reference 6) From left to right, examples of images, FFT images, structure factor S(q*), radial distribution function g(r), and the bond orientational correlation function g6(r) corresponding to charged polystyrene particles adsorbed at the octane-water interface.

The two-dimensional model system described in Chapter 6 provides an ideal platform to test the validity of KTHNY theory due to its easily controllable pair potential and the ease to precisely capture instantaneous information of a large region of the system. I propose that a systematic study of the solid-liquid phase transition will determine the existence of the hexatic phase and its dependence on pair potential. More specifically, at a given magnetic field strength (attraction potential depth), samples of magnetic colloidal spheres at a spectrum of densities (surface coverage) from 0.05 to 0.8 can be prepared and allowed sufficient time to reach equilibrium. Then images of different bulk phases can be taken to compute structure factor S(q*), radial distribution function g(r), and the bond orientational correlation function g6(r) as shown in Figure 7.3. From the positional and orientational correlations, crystalline and hexatic phases can be identified and a detailed phase diagram including hexatic phase region(s) can be constructed. The results can be further compared with existing experimental results to analyze the effect of pair potential on the onset of hexatic phase in two-dimensional melting phenomena.

7.3. Rod diffusion in confined geometry

The diffusion of filaments in a crowded environment is highly constrained and anisotropic; it underlies the behavior of such disparate systems as polymer materials, nanocomposites, and the cell cytoskeleton[13]. Despite decades of theoretical study, the fundamental diffusion dynamics of such systems remains a mystery[14]. Due to the

nanoscale sizes, the diffusion dynamics of polymer are difficult to be resolved at the single-molecule scale; thus they are often studied by observing their colloidal counterparts of similar shape and rigidity[14-17].

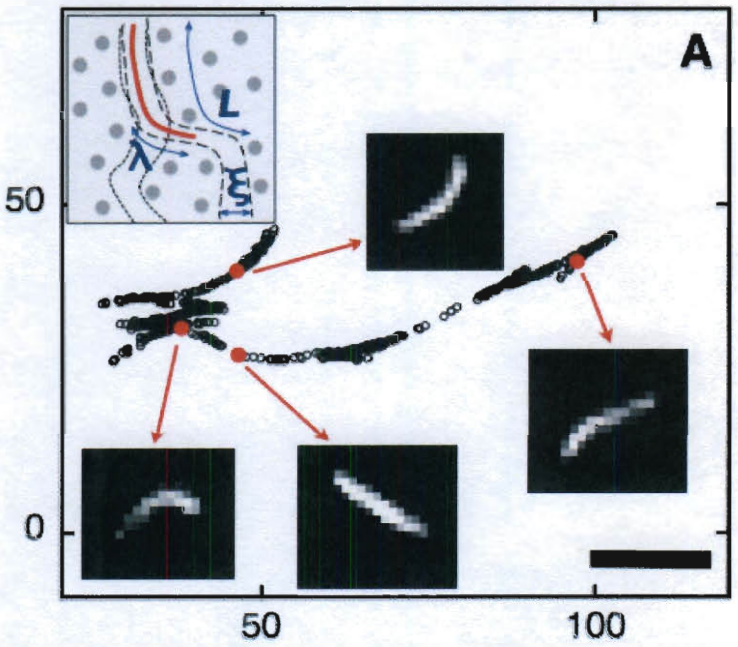

Figure 7.4. (Adapted from reference 11) (x, y) center-of-mass trajectories of a SWNT reptating in 1.5 w/w % agarose gel and representative NIR images of the SWNT, illustrating the effect of flexibility on reorientation of SWNT in different pores (scale bar, 5 mm). (Inset) Schematic of a stiff filament in a fixed network: L is the length of the filament, l is the deflection length, and x is the pore size of the network.

Though filaments such as microtubules, actin filaments, and carbon nanotubes have been demonstrated to be good candidates for crowed polymer dynamics studies, they suffer

from difficulties in imaging, virtuosity of rigidity range and desired length control. I believe my system of DNA-linked magnetic particle chains, with their wide range of controlled bending rigidity, ease of precise imaging and length control, coupled with the well-designed microfluidic patterns, could be used to study diffusion dynamics of filaments with finite rigidity in confined geometries.

7.4. Using emulsions to synthesize uniform length chains

In Chapter 2 and 3, I have discussed the assembly of chain structure using magnetic particles in batches in a flow cell. The length distribution depends on the initial particle concentration, applied magnetic field strength, and synthesis time. For many applications[16,18] (e.g. uniform mixing, supplying chains as models to study diffusion, etc.) uniform chain length distribution is desired. Thus it is valid to investigate an efficient assembly method to engineer a uniform length distribution of these chains.

In this section, I propose a technique using emulsions within flow-focusing microfluidic device to synthesize uniform length chains. The idea is demonstrated in the following sketch (Figure 7.5).

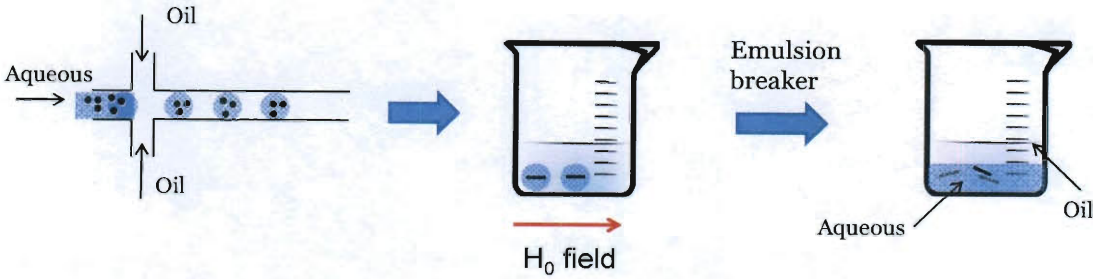

Figure 7.5. Schematic illustration of the technique of using emulsions within flow-focusing microfluidic device to synthesize uniform length chains.

7.4.1. Idea of encapsulation

In this proposed technique, surface-functionalized magnetic particles and linkers are pre-mixed with W/O emulsifier in aqueous phase. This aqueous dispersion is flown through a microfluidic flow-focusing cross section to be uniformly divided[15] into droplets dispersed in oil continuous phase. This W/O emulsion is collected in a beaker and an uniform magnetic field is applied to make the particles in each water droplet to form chains (Figure 7.5). Since the droplets are of the same size and each droplet has similar number of magnetic particles, the resulting chains have similar length. After the chains are made, emulsion breaker molecules are added to the beaker to make the water droplets coalesce into a continuous aqueous phase where the chains are finally collected.

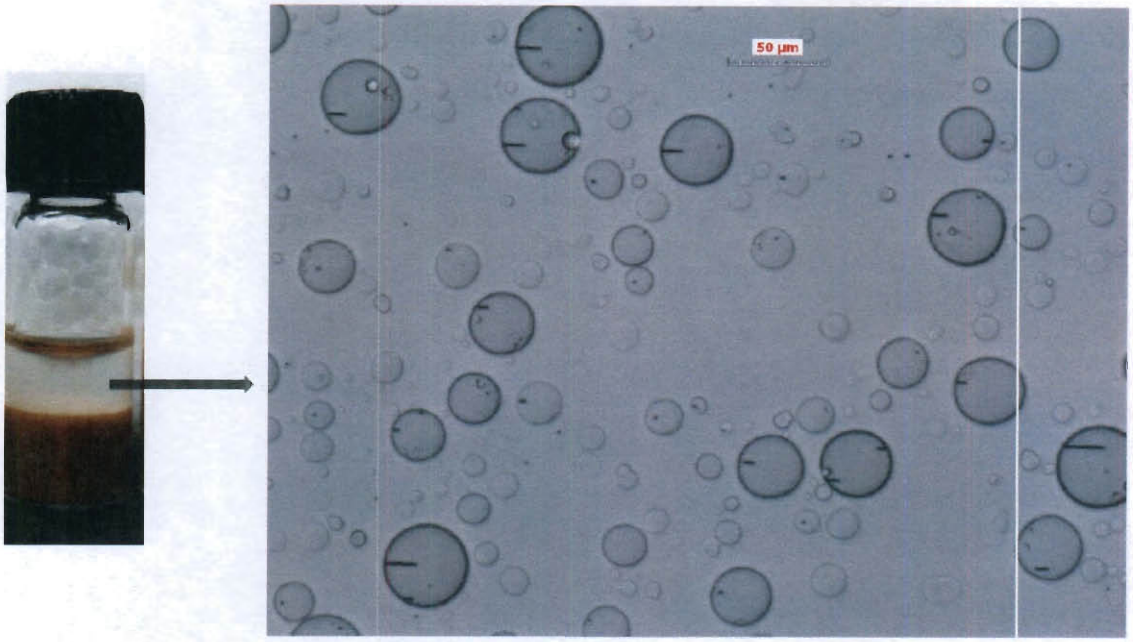

Figure 7.6. The proposed synthesis procedures done in bulk. The aqueous phase has a volume of 0.5mL, particle concentration 0.5wt%, emulsifier Aerosol OT concentration (1mg/g); the oil phase is dodecane. The water droplets with magnetic particles are found in the upper oil-continuous phase. The right-hand-side image is a sample taken out of the upper phase and loaded onto a glass slide.

7.4.2. Microfluidics to control emulsion size

The key to the success of achieving uniform chain length distribution is the creation of uniform water droplets. This is relies on the microfluidic flow-focusing technique. The preliminary device designed (Figure 7.7) is a cross-sectional junction with equal channel widths. Water droplets are successfully generated (inset of Figure 7.7) in oil-continuous phase.

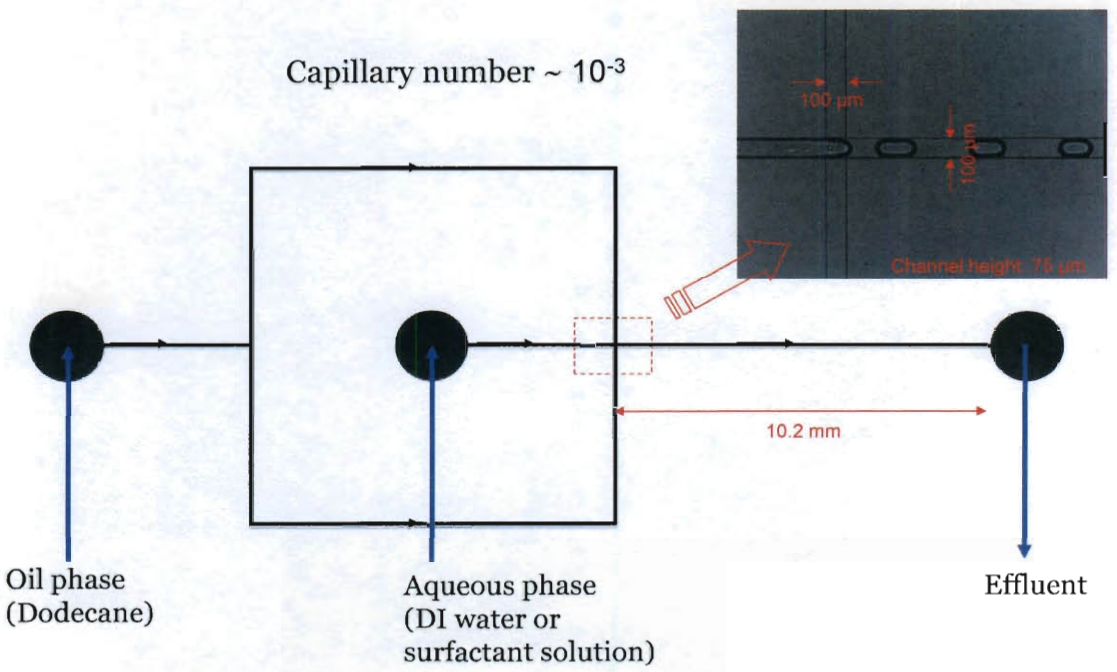

Figure 7.7. The microfluidic flow focusing device design. *Inset*, uniform water droplets generated in oil continuous phase.

7.5. DNA-linked chain as microrheometer

Microrheology is a field that offers the possibility to probe the rheological properties of liquids on a much smaller scale than conventional rheometers[20,21]. Microrheology offers the advantage of studying samples that are much smaller than are necessary in traditional rheology (microliters as opposed to milliliters). This offers a significant edge in biological fields where large samples cannot be prepared (as is the case when high-throughput analysis is desired). Active microrheology, as compared with its passive

counterpart, relies on the manipulation of probes using external forces. Magnetic particles and more recently chains of magnetic particles[22,23] are frequently used in active microrheology due to the ease with which they can be manipulated using a magnetic field. The rotation of single magnetic particles has been utilized by Besseris and Yeates to study Newtonian fluids as well as to characterize the viscoelastic properties of mucus[24]. Wilhelm et al. demonstrated the ability to use chains of unlinked magnetic particles to probe the properties of a micellar Maxwell solution[25], colloidal suspensions[26], and the interior of a cell.

In this section, I propose to study the use of linked chains of magnetic particles to probe the rheological properties of both viscous liquid and viscoelastic liquid. The proposed experimental procedure is, first, disperse linked chains into the liquid to be measured at a very dilute concentration; then, inject the dispersion into a glass flow cell and place the cell onto a microscope stage where the 4 solenoids are centered (same as the setup in Chapter 6); finally, magnetic field is applied and the motion of a selected chain is recorded and analyzed to give rheological properties of the sample fluid. With this technique, the volume required for a measurement is as low as 20μL.

7.5.1. Viscous fluids

I utilize the models discussed in Wilhelm et al.[25] as well as Biswal and Gast[27] to describe the system. In a dilute suspension (no chain-chain interaction) of chains in a viscous fluid, when a chain is rotating synchronously with external rotational magnetic field (constant frequency) at steady state, the magnetic torque and the viscous torque balance

each other, allowing us to equate the two formula and rearrange to obtain the viscosity of the fluid.

$$\eta = \frac{\mu_0 \chi^2 H_0^2 \left(\ln(N/2) + b/N\right)\sin(2\alpha)}{32N\omega} \tag{7.1}$$

For a given chain of length N, rotating synchronously at a frequency of ω in a viscous fluid, once the phase lag angle α (Figure 7.8) is measured, the viscosity η is determined from Equation 7.1. In fact, in the synchronous rotation case, the steady state phase lag angle at each rotational frequency gives an independent measurement of viscosity and thus $\eta(\omega)$ can be obtained.

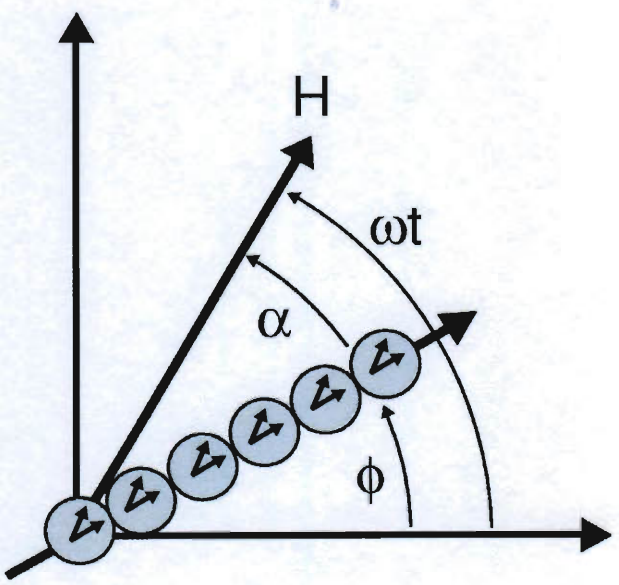

Figure 7.8. Schematic illustrating the geometry of a magnetic particle chain under an externally applied rotational magnetic field.

Here I show some preliminary results (Figure 7.9) of viscosity measurement using this technique of a 60 v/v% solution of glycerol in water, a 1 w/v% solution of polyethylene oxide (PEO) in water, and a suspension of carbon nanotubes (CNTs).

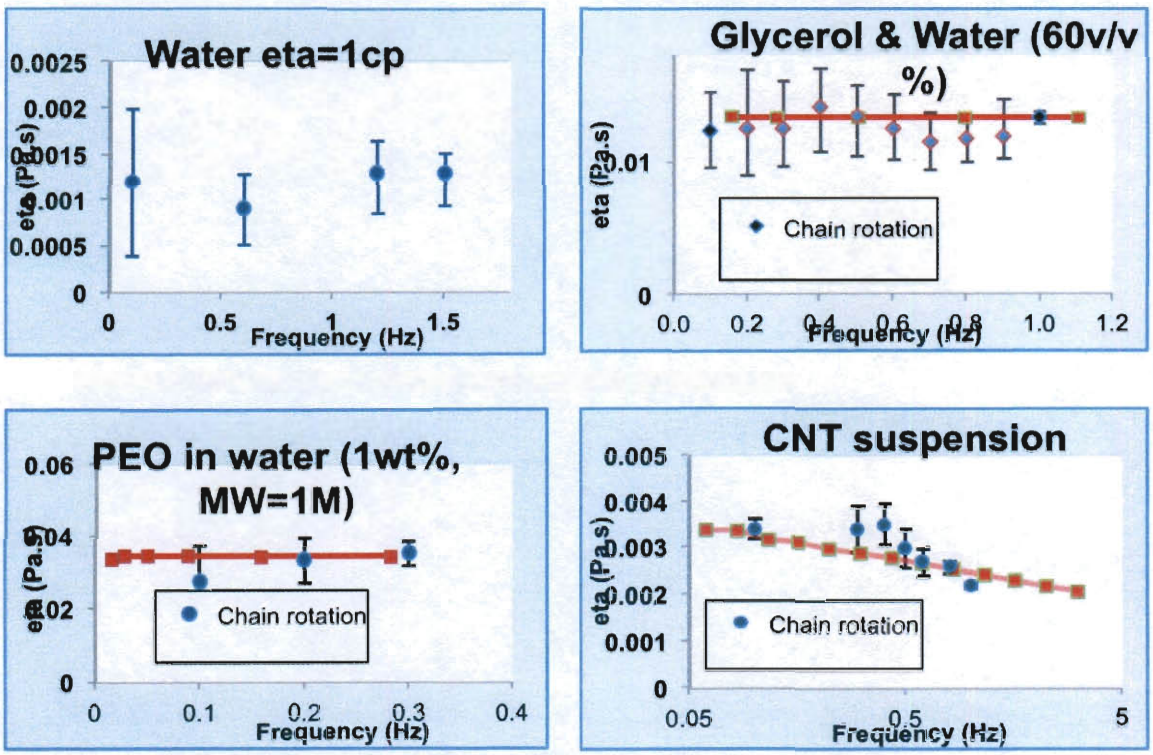

Figure 7.9. Viscosity versus frequency data obtained from both chain rotation and ARES measurements for A) water, B) glycerol (60 v/v%) in water, C) PEO (1 w/v%) in water, and D) CNT suspension

7.5.2. Viscoelastic fluid

When a chain is immersed in a Maxwell fluid, which is characterized by a shear modulus G and a viscosity η, or shear modulus G and relaxation time(s) τ_R, the these properties can be measured by applying a transient magnetic field and observing the chain orientation relaxation. The analytical solution can be obtained for any initial field orientation β_0,

$$\frac{t}{\tau_R} = \ln\frac{\sin[2(\beta_0-\theta_0)]}{\sin[2(\beta_0-\theta)]} + \frac{\kappa_d}{\kappa_m} G \ln\frac{\tan(\beta_0-\theta_0)}{\tan(\beta_0-\theta)} \quad (7.2)$$

where $\theta(t)$ is the angle between the current (at time t) and initial orientation of a chain, and $\beta(t)$ is the angle between the current (at time t) and initial orientation of the magnetic field. Time-dependent phase lag angle can be calculated as $\alpha = \beta(t) - \theta(t)$. The viscosity η governs the chain's long-time relaxation to the new field orientation. The instantaneous angle jump at $t = 0$, $\theta_0 = \frac{\kappa_m}{2\kappa_d G}\sin[2(\beta_0-\theta_0)]$, directly gives the value of G: the larger the jump, the smaller the G.

Typical chain orientation relaxation plots are shown in Figure 7.10. The blue dots are measured chain orientation and the red curve is a two-parameter (one-relaxation-time) Maxwell fit using Equation 7.2.

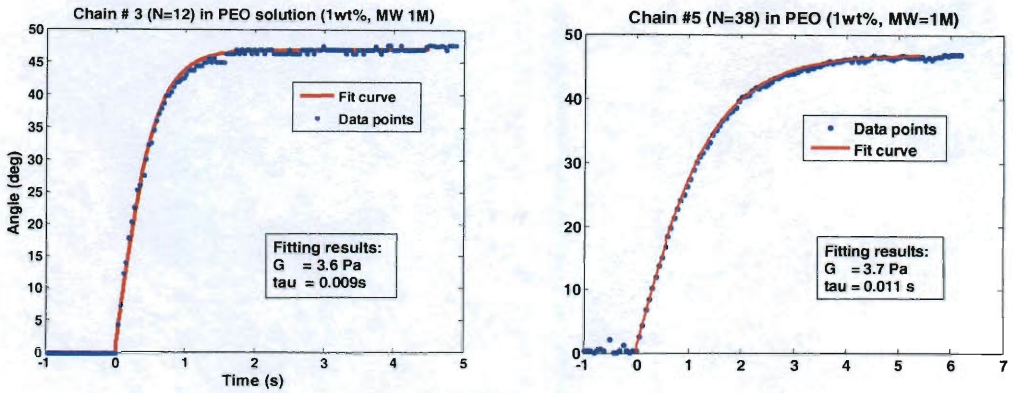

Figure 7.10. Typical chain orientation relaxations toward a new field direction plot and their corresponding two-parameter Maxwell fits. The blue dots are measured chain orientation and the red curve is a two-parameter Maxwell fit using Equation 7.9. Magnetic field orientation is switched at time zero and is kept constant at t>0. The magnetic particle chains are measured to have aspect ratio of 12 (N=12) and 38 (N=38), and they are dispersed in a Polyethylene oxide (PEO) solution (MW=1,000,000, 1wt% in water).

With the above evidence, I believe the linked magnetic colloidal chains are a good candidate for microrheology measurement. Not only can sample volumes be reduced to microliters, but also interesting physics can be uncovered at such length scale that would not be seen in a conventional rheometer.

7.6. Conclusions

In the final chapter of the dissertation, I have discussed both experimental and theoretical future work that will result in: (i) better utilization of the systems and techniques

developed in this thesis to a variety of applications and (ii) better understanding of fundamental diffusion dynamics and two-dimensional phase transition by the help of the model systems described. In addition, I have proposed a new way to synthesize DNA-linked magnetic particle chains with uniform length by using emulsion technique in microfluidic devices. The proposed work in this chapter will reveal further exciting applications of the system of magnetic colloids and their assemblies and elucidate some fundamental aspects of diffusion dynamics and two-dimensional phase transitions.

7.7. Reference

1. Knowles, T. P.; Fitzpatrick, A. W.; Meehan, S.; Mott, H. R.; Vendruscolo, M.; Dobson, C. M.; Welland, M. E., Role of intermolecular forces in defining material properties of protein nanofibrils. *Science* **2007,** 318, (5858), 1900-1903.
2. Knowles, T. P. J.; Smith, J. F.; Craig, A.; Dobson, C. M.; Welland, M. E., Spatial persistence of angular correlations in amyloid fibrils. *Physical Review Letters* **2006,** 96.
3. Pepys, M. B., Pathogenesis, diagnosis and treatment of systemic amyloidosis. *Philosophical Transactions of the Royal Society B-Biological Sciences* **2001,** 356, (1406), 203-210.
4. Frenkel, D.; Smit, B., *Understanding molecular simulation.* Academic Press: San Diego, 2002; Vol. 1.
5. Peng, Y.; Wang, Z.; Alsayed, A. M.; Yodh, A. G.; Han, Y., Melting of Colloidal Crystal Films. *Physical Review Letters* **2010,** 104, (20), 205703.
6. Gast, A. P.; Russel, W. B., Simple ordering in complex fluids - Colloidal particles suspended in solution provide intriguing models for studying phase transitions. *Physics Today* **1998,** 51, (12), 24-30.
7. Naidoo, K. J.; Schnitker, J.; Weeks, J. D., 2-dimensional melting revisited - Molecular dynamics simulations initiated with optical microscopy data. *Molecular Physics* **1993,** 80, (1), 1-24.
8. Strandburg, K. J., TWO-DIMENSIONAL MELTING. *Reviews of Modern Physics* **1988,** 60, (1), 161-207.
9. Bonales, L. J.; Rubio, J. E. F.; Ritacco, H.; Vega, C.; Rubio, R. G.; Ortega, F., Freezing Transition and Interaction Potential in Monolayers of Microparticles at Fluid Interfaces. *Langmuir* **2011,** DOI: 10.1021/la104917e.
10. Zahn, K.; Lenke, R.; Maret, G., Two-stage melting of paramagnetic colloidal crystals in two dimensions. *Physical Review Letters* **1999,** 82, (13), 2721-2724.
11. Zangi, R.; Rice, S. A., Nature of the transition from two- to three-dimensional ordering in a confined colloidal suspension. *Physical Review E* **2000,** 61, (1), 660-670.
12. Lin, B. J.; Chen, L. J., Phase transitions in two-dimensional colloidal particle system observed in Langmuir trough. *Colloids and Surfaces a-Physicochemical and Engineering Aspects* **2006,** 284, 239-245.
13. Brangwynne, C. P.; Koenderink, G. H.; Barry, E.; Dogic, Z.; MacKintosh, F. C.; Weitz, D. A., Bending dynamics of fluctuating biopolymers probed by automated high-resolution filament tracking. *Biophysical Journal* **2007,** 93, (1), 346-359.
14. Fakhri, N.; MacKintosh, F. C.; Lounis, B.; Cognet, L.; Pasquali, M., Brownian Motion of Stiff Filaments in a Crowded Environment. *Science* 330, (6012), 1804-1807.
15. Fakhri, N.; Tsyboulski, D. A.; Cognet, L.; Weisman, R. B.; Pasquali, M., Diameter-dependent bending dynamics of single-walled carbon nanotubes in liquids. *Proceedings of the National Academy of Sciences of the United States of America* **2009,** 106, (34), 14219-14223.
16. Li, D. C.; Banon, S.; Biswal, S. L., Bending dynamics of DNA-linked colloidal particle chains. *Soft Matter* **2010,** 6, (17), 4197-4204.
17. Li, D. C.; Fakhri, N.; Pasquali, M.; Biswal, S. L., Axial thermal rotation of

slender rods. *Physical Review Letters* **2011**, accepted.
18. Biswal, S. L.; Gast, A. P., Micromixing with linked chains of paramagnetic particles. *Analytical Chemistry* **2004,** 76, (21), 6448-6455.
19. Utada, A. S.; Lorenceau, E.; Link, D. R.; Kaplan, P. D.; Stone, H. A.; Weitz, D. A., Monodisperse double emulsions generated from a microcapillary device. *Science* **2005,** 308, (5721), 537-541.
20. Mason, T. G.; Ganesan, K.; vanZanten, J. H.; Wirtz, D.; Kuo, S. C., Particle tracking microrheology of complex fluids. *Physical Review Letters* **1997,** 79, (17), 3282-3285.
21. Gittes, F.; Schnurr, B.; Olmsted, P. D.; MacKintosh, F. C.; Schmidt, C. F., Microscopic viscoelasticity: Shear moduli of soft materials determined from thermal fluctuations. *Physical Review Letters* **1997,** 79, (17), 3286-3289.
22. Dhar, P.; Cao, Y.; Fischer, T. M.; Zasadzinski, J. A., Active Interfacial Shear Microrheology of Aging Protein Films. *Physical Review Letters* 104, (1), 016001.
23. Reynaert, S.; Brooks, C. F.; Moldenaers, P.; Vermant, J.; Fuller, G. G., Analysis of the magnetic rod interfacial stress rheometer. *Journal of Rheology* **2008,** 52, (1), 261-285.
24. Besseris, G. J.; Yeates, D. B., Rotating magnetic particle microrheometry in biopolymer fluid dynamics: Mucus microrheology. *Journal of Chemical Physics* **2007,** 127.
25. Wilhelm, C.; Browaeys, J.; Ponton, A.; Bacri, J. C., Rotational magnetic particles microrheology: The Maxwellian case. *Physical Review E* **2003,** 67, (1).
26. Wilhelm, C.; Elias, F.; Browaeys, J.; Ponton, A.; Bacri, J. C., Local rheological probes for complex fluids: Application to Laponite suspensions. *Physical Review E* **2002,** 66, (2).
27. Biswal, S. L.; Gast, A. P., Rotational dynamics of semiflexible paramagnetic particle chains. *Physical Review E* **2004,** 69, (4), 9.

Appendix A

MATLAB code for Fourier mode analysis

FMA main routine:

```
clc
% This subroutine performs the Fourier mode analysis
% Programmed by Dichuan Li 09/2009
%-------------------------------------------------------------
% % Parameters ------
N = length(P(1,:,1)); % # of particles
a = 1e-6; % diameter of particles in (m)
% Young's Modulus for bending (N*m^2)
kb = 1.38e-23; % Boltzmann constant in (J/K)
T = 300; % temperature 300K
%-------------------------------------------------------------
K = length(P(1,1,:));
cosj = [];
%-------------------------------------------------------------------
% Loop over all frames
display('Calculating angles from data ... ...');
for i = 1:K
   %-----------------------------------------------------
   % theta is the angle
   for j = 1 : N-1
      theta(j,i) = atan( (P(2,j+1,i)-P(2,j,i)) / (P(1,j+1,i)-P(1,j,i)) );
   end
   %-----------------------------------------------------
end
clc
display('Non-linear fitting using Fourier modes ... ...');

beta0 = 0.1*ones(N-1,1);
coefs = [];
x = 1:N-1;
x = x';
for i = 1:K
   y = theta(:,i);
   beta  = nlinfit(x,y,@CosMod,beta0);
   coefs = [coefs beta];
   if mod(i,100) == 0
      eval(['display(''' 'frame # ' num2str(i) ''');']);
   end
```

```
end
for j = 1 : length(coefs(:,1))-1
   [mu sigma] = normfit(coefs(j+1,:));
   yy(j)      = sigma^2;
end
plot(1:length(coefs(:,1))-1,yy,'o'); hold on
%-------------------------------------------------------------------------
% Calculation of the noise floor
L = N; % Contour length of the chain
epsilon = 0.01; % random noise in the unit of microns
for i = 1:length(coefs(:,1))-1
   noise(i) = 4/L*epsilon^2*(1+(N-2)*sin(i*pi/2/(N-1))^2);
end
plot(1:length(coefs(:,1))-1,noise,'k'); hold on
%-------------------------------------------------------------------------
% Calculation of the persistence length Lp
for i = 1:length(coefs(:,1))-2
   Lp(i) = N^2/i^2/pi^2./yy(i);
end
[mu sigma] = normfit(Lp(1:6));


function yhat = CosMod( beta, x )
%UNTITLED1 Summary of this function goes here
%  Detailed explanation goes here
y = 0;
NN = 24;
for i = 1:NN-1
   y = y + beta(i)*cos((i-1)*pi*x/NN);
end
yhat = sqrt(2/NN)*y;
```

Angle distribution:

```
% This subroutine compute the angle distribution
%-----------------------------------------------------------------
% % Parameters ------
N = length(P(1,:,1)); % # of particles
a = 1e-6; % diameter of particles in (m)
% Young's Modulus for bending (N*m^2)
kb = 1.38e-23; % Boltzmann constant in (J/K)
T = 300; % temperature 300K
%-----------------------------------------------------------------
K = length(P(1,1,:));
cosj = [];
%-------------------------------------------------------------------------
% Loop over all frames
for i = 1:K
   % Calculate relative distance
   % R is a 2nd tensor, r(i,j) is the relative distance between i and j
   R = zeros(N);
   for j = 1 : N-1
```

```
      for k = j+1 : N
        R(j,k) = ( (P(1,k,i)-P(1,j,i))^2 + (P(2,k,i)-P(2,j,i))^2 + (P(3,k,i)-P(3,j,i))^2  )^0.5;
      end
    end
    % "u(i)" is the unit direction vector between bead j+1 and j
    for j = 1 : N-1
      u(:,j,i) = ( P(:,j+1,i) - P(:,j,i) ) / R(j,j+1);
    end
    %-------------------------------------------------------------
    % cosj(theta) derived from a*b = |a|*|b|*cos(theta)
    % theta is the angle between the u(j) vector and u(j-1)
    for j = 1 : N-2
      cosj(j,i) = u(1,j,i)*u(1,j+1,i) + u(2,j,i)*u(2,j+1,i) + u(3,j,i)*u(3,j+1,i);
      if u(2,j+1,i) >= u(2,j,i) % convex on X-Z plane
        sinj(j,i) = sin(acos(cosj(j,i)));
      else
        sinj(j,i) = -sin(acos(cosj(j,i)));
      end
    end
    %-------------------------------------------------------------
end
%-------------------------------------------------------------------------
% Absolute values of angles
angle = acos( cosj ) * 180 / pi ;
% Real angles
angle1 = asin(sinj) * 180 / pi ;
% Initial angles
% Initializing the initial angles between arbitrary vectors
% "angle1_init" was previously calculated from "Angle distribution _ New"
% file and is the means (over frames) of angles for each pair of vectors
angle1_init = mean(angle1') ;

for i=1:N-2
angle_adju(i,:) = angle1(i,:) - angle1_init(i);
end
```

Appendix B

MATLAB code for Brownian Dynamics simulation of a single particle chain

Main routine:

```
% N-particle-chain thermal motion
clear
clc
%%%
```

```
for i = 1: N
   x0(1,i) = i + L*(i-1);
   x0(2,i) = 0;
   x0(3,i) = 0.02;
end
P(:,:,1) = x0; % P stores positions of bead at all time steps
pixel = round(pi*(1/2/(N+5)*440)^2);
%-----------------------------------------------------------------
%%%%%%%%%%%%%%%%%%  Main routine  %%%%%%%%%%%%%%%%%%%%%%%%%%%%%
%-----------------------------------------------------------------
x = [];  % x stores the X,Y positons of N particles
i = 1; k =2; x = x0;
while t < Tmax
   %-----------------------
   % Brownian displacement in X and Y-direction
   dR(1:3,:) = normrnd(0,sqrt(2*D*dt),3,N);
   %-----------------------------------------------------------
   % Unconstrained displacement (Eq.15 McCammon et.al. 1978)
   %
   % and reduce all length to microns;
   DF = V_calc_Hydro_Bend_Metric(x,a,L,EI,mg);
   dx_unconstr = DF*dt/kb/T/a + dR/a;
   % Constraint projection_ LINCS (Eq.16 Wang et.al. J.Chem.Phys 2005)
   x = constraint(dx_unconstr,x,L);
   %-----------------------------------------------------------
   t = t + dt;
   %Record positions every other 830 runs;
   i=i+1;
   %if mod(i,20) == 0
   if mod(i,round(1/200/dt)) == 0
      P(:,:,k) = x;
      %scatter(P(1,1:N,k),P(2,1:N,k),pixel,'k','filled'); axis([-2 N+3 -7 7]);
      %M = getframe;
      %pause;
      k = k + 1
   end
   %-------------------------------------
end
% THE END of Brownian Dynamics Code
%-----------------------------------------------------------------
```

Constraints:

```
function xxx = constraint(dx_unconstr,x,L)
%-----------------------------------------------------------------
% This subroutine constrains the bond lengths between adjacent beads with
% LINCS algorithm from B. Hess et al., J. Comp. Chem. 18, 1463 (1997).
% 3D version programmed by Dichuan Li on Nov 20 2009
%-----------------------------------------------------------------
% Parameters ------
N = length(x); % # of particles
%-----------------------------------------------
```

```
% Matrix Conversion
% for original position
X = [];
for i = 1:N
   X(3*i-2) = x(1,i);
   X(3*i-1) = x(2,i);
   X(3*i)   = x(3,i);
end
% For Brownian displacement
dx = [];
for i = 1:N
   dx(3*i-2) = dx_unconstr(1,i);
   dx(3*i-1) = dx_unconstr(2,i);
   dx(3*i)   = dx_unconstr(3,i);
end
%-----------------------------------------------------
% Bij = dgi/drj where gi is the ith constraint equation
% gi=(x(1,i)-x(1,i+1))^2+(x(2,i)-x(2,i+1))^2+(x(3,i)-x(3,i+1))^2 - a^2 = 0
% Bij = dgi/drj =
B = zeros(N-1,3*N);
for i = 1:(N-1)
   for j = 1:3*N
      if (j>=3*i-2)&(j<=3*i)
         B(i,j) = 2*(X(j)-X(j+3));
      elseif (j>=3*i+1)&(j<=3*i+3)
         B(i,j) = -2*(X(j-3)-X(j));
      end
   end
end
%-----------------------------------------------
T = B'*inv(B*B');
I = zeros(3*N);
for i = 1:3*N
   for j = 1:3*N
      if j==i
         I(i,j) = 1;
      end
   end
end
%---------------------------------------
% d is the bond length to be fixed !!
d = 2*(1+L)*ones(N-1,1);
dx_constrX = (X + dx) * (I - T*B) + (T*d)';

xxx = [];
for i = 1:N
   xxx(1,i) = dx_constrX(3*i-2);
   xxx(2,i) = dx_constrX(3*i-1);
   xxx(3,i) = dx_constrX(3*i);
end
```

Force calculations:

```
%%%
```

```
    c(i) = - ( u(1,i)*u(1,i-1) + u(2,i)*u(2,i-1) + u(3,i)*u(3,i-1) );
end
% G is the tridiagonal matrix
G = zeros(N-1,N-1);
G(1,1:2) = [d c(2)];
G(N-1,N-2:N-1) = [c(N-1) d];
for i = 2 : N-2
   G(i,i)   = d;
   G(i,i-1) = c(i);
   G(i,i+1) = c(i+1);
end
G_1 = inv(G);
%-------------------------------------------------------------------------
%%%%%%%%%%%%%%%%%%%%%%%%%%%%%%%%%%%%%%%%%%%%%%%%%%%%%%%%%%%%%%%%%%%%%%%%
%%%%%%%%%%%%%%%%%%%%%%%%%%%%%%%%%%%%%%%%%%%%%%%%%%%%%%%%%%%%%%%%%%%%%%%%
% Calculate Bending forces -- " Fbend " (Allison <Macromo.> 1986, 19, 123)%
%%%%%%%%%%%%%%%%%%%%%%%%%%%%%%%%%%%%%%%%%%%%%%%%%%%%%%%%%%%%%%%%%%%%%%%%
%%%%%%%%%%%%%%%%%%%%%%%%%%%%%%%%%%%%%%%%%%%%%%%%%%%%%%%%%%%%%%%%%%%%%%%%
%-------------------------------------------------------------------------
% Force constant
g = EI/a/a; % Bending force constant (eq4 Allison <Macromo.> 1985, 19, 118)
%-------------------------------------------------------------------------
dleft = []; dright = [];
for i = 2 : N-1
   u_dot(i) = u(:,i)' * u(:,i-1);
end
for k = 2 : N-1
  dleft(:,k) = (g + kb*T/a*G_1(k,k-1) ) * (u(:,k-1) - u_dot(k) * u(:,k) );
end
for k = 1 : N-2
  dright(:,k) = (g + kb*T/a*G_1(k,k+1) ) * (u(:,k+1) - u_dot(k+1) * u(:,k) );
end
% Force terms F := F_bend_met
Fbend(:,1) = - dright(:,1);
Fbend(:,2) = - dleft(:,2) + dright(:,1) - dright(:,2);
for k = 3 : N - 2
  Fbend(:,k) = dleft(:,k-1) - dleft(:,k) + dright(:,k-1) - dright(:,k);
end
Fbend(:,N-1)  = dleft(:,N-2) -  dleft(:,N-1) + dright(:,N-2);
Fbend(:,N)    = dleft(:,N-1);
% THE END of computing bending forces
%-------------------------------------------------------------------------
%%%%%%%%%%%%%%%%%%%%%%%%%%%%%%%%%%%%%%%%%%%%%%%%%%%%%%%%%%%%%%%%%%%%%%%%
%%%%%%%%%%%%%%%%%%%%%%%%%%%%%%%%%%%%%%%%%%%%%%%%%%%%%%%%%%%%%%%%%%%%%%%%
% Calculate Gravitational forces (Dichuan Li <Phys. Rev. E> 2010)
%%%%%%%%%%%%%%%%%%%%%%%%%%%%%%%%%%%%%%%%%%%%%%%%%%%%%%%%%%%%%%%%%%%%%%%%
%%%%%%%%%%%%%%%%%%%%%%%%%%%%%%%%%%%%%%%%%%%%%%%%%%%%%%%%%%%%%%%%%%%%%%%%
%-------------------------------------------------------------------------
Fgrav(1:2,:) = zeros(2,N);
Fgrav(3,:)   = -mg*ones(1,N);
%-------------------------------------------------------------------------
%%%%%%%%%%%%%%%%%%%%%%%%%%%%%%%%%%%%%%%%%%%%%%%%%%%%%%%%%%%%%%%%%%%%%%%%
%%%%%%%%%%%%%%%%%%%%%%%%%%%%%%%%%%%%%%%%%%%%%%%%%%%%%%%%%%%%%%%%%%%%%%%%
% Calculate Repulsive forces from substrate (Dichuan Li <Phys. Rev. E> 2010)
```

```
%%%
```

```
T = 300; % temperature 300K
%-------------------------------------------------------------
K = length(P(1,1,:));
cosj = [];
%-------------------------------------------------------------
% Loop over all frames
for i = 1:K
   % Calculate relative distance
   % R is a 2nd tensor, r(i,j) is the relative distance between i and j
   R = zeros(N);
   for j = 1 : N-1
      for k = j+1 : N
         R(j,k) = ( (P(1,k,i)-P(1,j,i))^2 + (P(2,k,i)-P(2,j,i))^2 + (P(3,k,i)-P(3,j,i))^2  )^0.5;
      end
   end
   % "u(i)" is the unit direction vector between bead j+1 and j
   for j = 1 : N-1
      u(:,j,i) = ( P(:,j+1,i) - P(:,j,i) ) / R(j,j+1);
   end
   %-------------------------------------------------------
   % cosj(theta) derived from a*b = |a|*|b|*cos(theta)
   % theta is the angle between the u(j) vector and u(j-1)
   for j = 1 : N-2
      cosj(j,i) = u(1,j,i)*u(1,j+1,i) + u(2,j,i)*u(2,j+1,i) + u(3,j,i)*u(3,j+1,i);
      if u(2,j+1,i) >= u(2,j,i) % convex on X-Z plane
         sinj(j,i) = sin(acos(cosj(j,i)));
      else
         sinj(j,i) = -sin(acos(cosj(j,i)));
      end
   end
   %-------------------------------------------------------
end
%-------------------------------------------------------------
% Absolute values of angles
angle = acos( cosj ) * 180 / pi ;
% Real angles
angle1 = asin(sinj) * 180 / pi ;
% Initial angles
% Initializing the initial angles between arbitrary vectors
% "angle1_init" was previously calculated from "Angle distribution _ New"
% file and is the means (over frames) of angles for each pair of vectors
angle1_init = mean(angle1') ;

for i=1:N-2
angle_adju(i,:) = angle1(i,:) - angle1_init(i);
end
```

Appendix C

MATLAB code for Brownian Dynamics simulation of 2D spheres in a rotational magnetic field

Main routine:

```
% N-particle-cluster thermal motion
clear
clc
%%%
```

```
%-------------------------------------------------------------------
% Alternating magnetic field parameters
Bx = 6;   % x-direction Magnetic field in Gauss
By = 6;   % y-direction Magnetic field in Gauss
ti = 0.2;  % time to start alternating field
f  = 50;   % Frequency in Hz
%-----------------------------------------------------
% Magnetic dipole moment as a result of field
Chi_x = 8E-10*Bx^3 + 2E-06*Bx^2 - 0.0022*Bx + 0.8666; % dimensionless
Chi_y = 8E-10*By^3 + 2E-06*By^2 - 0.0022*By + 0.8666; % dimensionless
Hx    = Bx/1e4/mu_0; % H field in A/m
Hy    = By/1e4/mu_0; % H field in A/m
Mdp_x = 4/3 * pi * (a/2)^3 * mu_0 .* Chi_x .* Hx; % Magnetic dipole moment
Mdp_y = 4/3 * pi * (a/2)^3 * mu_0 .* Chi_y .* Hy; % Magnetic dipole moment
%%%
```

```
%%%%%%%%%%%%%%%%%%%%%%%%%%%%%%%%%%%%
%-------------------------------------------------------------------
x = [];  % x stores the X,Y positons of N particles
i = 1; k =2; x = x0;
while t < Tmax
   %----------------------
   % Brownian displacement in X and Y-direction
   dR(1:2,:) = normrnd(0,sqrt(2*D*dt),2,N);
   %-------------------------------------------------------------
   % Magnetic field calculation
   if t >= ti
      Mdp = [Mdp_x*cos(f*2*pi*(t-ti)) Mdp_y*sin(f*2*pi*(t-ti))];
   else
      Mdp = [0 0];
   end
   %-------------------------------------------------------------
   % Unconstrained displacement (Eq.15 McCammon et.al. 1978)
   % and reduce all length to microns;
   [DF Fmag u] = V_calc_Hydro_Mag _Nmer(x,a,L,yita,Mdp,z,phi,S,rho_infi);
   Fmagx(k) = Fmag(1,1);
   Fmagy(k) = Fmag(2,1);
   Fmagr(k) = (Fmag(1,1)*u(1,1) + Fmag(2,1)*u(2,1));
   dx_unconstr = DF*dt/kb/T + dR;
   x = x + dx_unconstr;
   %-------------------------------------------------------------
   t = t + dt;
   %Record positions every other 830 runs;
   i=i+1;
   %if mod(i,20) == 0
   if mod(i,round(1/20 1/dt)) == 0
      P(:,:,k) = x*1e6;
      scatter(P(1,1:N,k),P(2,1:N,k),pixel,'k','filled'); axis([-4 8 -5 5]*1.5);
      M(k) = getframe;
      %pause;
      k = k + 1
   end
   %-----------------------------------
end
% THE END of Brownian Dynamics Code
%-------------------------------------------------------------------------
```

Force calculations:

```
%%%%%%%%%%%%%%%%%%%
```

```
% Metric forces added on June 15 2007                                  %
% Non-uniform EI vector added on Nov 25th 2008                         %
% EI as a function of bending angle added on Feb 6th 2009              %
% Magnetic forces and inter-particle potential added on Oct 28th 2009  %
% Mangetic and Potential forces corrected on Nov 15th 2009             %
% Mangetic and Potential forces corrected  to add N-particle pair      %
% interactions on Nov 15th 2009                                        %
%                                                                      %
%%%
```

```
                5*(Mdp(1)*u(1,i,j)+Mdp(2)*u(2,i,j))^2)*u(2,i,j) + ...
                (Mdp(1)*u(1,i,j)+Mdp(2)*u(2,i,j))*Mdp(2) + ...
                (Mdp(1)*u(1,i,j)+Mdp(2)*u(2,i,j))*Mdp(2) );
   end
end
% Opposite forces on jth bead from ith (Newton's 3rd law)
for i = 1 : N-1
   for j = i+1 : N
      Fmagc(:,j,i) = - Fmagc(:,i,j);
   end
end
%---------------------------------------------------------------------
% Sum up all forces exerted on bead i
Fmag = zeros(2,N);
for i = 1 : N
   for j = 1 : N
      Fmag(1,i) = Fmag(1,i) + Fmagc(1,i,j);
      Fmag(2,i) = Fmag(2,i) + Fmagc(2,i,j);
   end
end

% THE END of computing Magnetic forces
%---------------------------------------------------------------------
%%%
```

```
    end
end
%-------------------------------------------------------------------------
% Sum up all forces exerted on bead i
Fpot = zeros(2,N);
for i = 1 : N
    for j = 1 : N
        Fpot(1,i) = Fpot(1,i) + Fpotc(1,i,j);
        Fpot(2,i) = Fpot(2,i) + Fpotc(2,i,j);
    end
end

% THE END of computing potential forces
%-------------------------------------------------------------------------
% Sum of forces
Ftot = Fpot + Fmag;
%F = zeros(2,N);
%-------------------------------------------------------------------------
%%%%%%%%%%%%%%%% End of Forces %%%%%%%%%%%%%%%%%%%%
%-------------------------------------------------------------------------
% Calculate coupling of hydrodynamic interaction --- DTF
V = []; % coupled interaction
DT = []; % Diffusion tensor
for j = 1:N    % compute velocity of the jth bead
    V(1:2,j) = 0;
    for k = 1:N
        %if k==j   % Contribution on the same particle
            V(1:2,j) = V(1:2,j) + [D 0;0 D]*Ftot(1:2,j);
        %else      % Contribution on different particles
        %    rr = x(:,j)*x(:,k)';
        %   V(1:2,j) = V(1:2,j) + kb*T/(8*pi*yita*R(j,k)) * ( (1+2*a^2/R(j,k)^2/3)*[1 0;0 1] + (1-
2*a^2/R(j,k)^2)* rr/R(j,k)^2 )*Ftot(1:2,j);
        %end
    end
end
DF = V;
```

Appendix D

FORTRAN code for Monte Carlo simulation

Main routine:

```
      Implicit double precision (a-h,o-z)
ccccccccccccccccccccccccccccccccccccccccccccccccccccccccccccccccccccccccccc
c
c     This is a 2D Metropolis Monte Carlo Program, NVT Ensemble.
c
c           It can also calculate Pressure and Chemical potential
c
c           Programmed by Dichuan Li in 02/22/2011
c
c     This program is an NVT Ensemble Monte Carlo simulation of the
c     2D paramagnetic colloid system. The pair potential between spheres is
c     electrostatic repulsion (1mM NaCl solution and -50mV Z-potential spheres)
c     and -3-power magnetic attraction with potential well depth Ud.
c
c     This program is written in reduced units. Lengths are scaled with the
c     particle diameter D. Pressure is output reduced by Rho*kT.
c
c     This program calculates the potential energy as well as the
c     pressure.  Fractional numbers of accepted configurations
c     are given as a rolling average and as an average over the entire
c     simulation.  All other averages are rolling averages.
c
ccccccccccccccccccccccccccccccccccccccccccccccccccccccccccccccccccccccccccc
c
c   Dimension coordinate arrays
c
      Dimension x(256), y(256)
          Dimension xtest(1000), ytest(1000)
      Dimension bin_vol(1000), i_g_hist(1000)
c
      tpi = 6.283185308D0
c
      iseed = 1104772519
c
      open(unit=1,file='input_lj.dat',form='formatted',status='old')
      open(unit=6,file='output.dat',form='formatted',status='unknown')
c
c   This routine reads necessary variables
c
      write(6,*)'  Input the no. of LJ atoms '
      read(1,*) natoms
```

```
      write(6,*) natoms
c
      write(6,*)'  Set the pair potential depth (i.e. 3)'
      read(1,*) Ud
      write(6,*) Ud
c
c     If you want to start from an old configuration, then assign that
c     configuration file to unit 2.
c
      write(6,*)'  Input 1 if running from old config or 2 if ',
     1        'running from lattice'
      read(1,*) itest
      write(6,*) itest
c
c     If a final configuration file is used then the density is read when
c     the final configuration is read.  The final configuration density has
c     priority over the guessed density.
c
      write(6,*)'  Set the reduced density'
      read(1,*) rost
      write(6,*) rost
c
      write(6,*)'  Input the no. of steps in the simulation'
      read(1,*) nst
      write(6,*) nst
c
      write(6,*)'  Input the reduced maximum displacement',
     1        ' (in units of D )'
      read(1,*) dp
      write(6,*) dp
c
      write(6,*)'  Input the no. of steps between print'
      read(1,*) nbp
      write(6,*) nbp
c
c     The number of steps between performing Widom particle insertion
c
      write(6,*) '  Input the no. of steps between Widom insertion'
      read(1,*) n_widom
      write(6,*) n_widom

c     The number of steps between recalculating the radial distribution function
c
      write(6,*) '  Input the no. of steps between calculating',
     1        ' the radial distribution function'
      read(1,*) n_radial
      write(6,*) n_radial
c
c     The bin width in units of sigma for the radial distribution function.
c
      write(6,*) '  Input the bin width for the distribution function'
      read(1,*) bin_width
      write(6,*) bin_width
c
c     The number of equilibration steps
c
      write(6,*)'  Input the no. of equilibration steps '
```

```
      read(1,*) n_equilib
      write(6,*) n_equilib
c
      close(unit=1)
c
      if(itest.ne.1)goto 2

c     This routine initializes certain variables that need initialization
c
c     Initialize the no. of accepted configurations (overall and
c     rolling average) to zero
c
 2    nc = 0
      nv = 0
c
c     Ipart = the no. of the particle to be moved.
c
      ipart = 0
c
c     volume of the simulation cell reduced by D^2.
c
      v1 = natoms / rost
c
c     H = half the box length reduced by D.
c
      h = 0.5D0 * ( v1 )**(1.0D0 / 2.0D0)
c
c     These variables are used to create an FCC lattice.
c
      in2 = (natoms)**(1./2.) + 0.1
      unit = 1.01
      shift = 0.0001
c
c     Pressure, Average potential energy, and average density
c
      pr = 0.0D0
      ape = 0.0D0
      ad = 0.0D0
c
c     The cutoff is the spherical cutoff of the potential.  Long range
c     corrections are made below.  Cutoff has units of D.
c
      cutoff = 3.5D0
      if (cutoff.gt.h) cutoff = h
c
c     Potential cutoff in units of half the box length and squared.
c     "chempotlrc" is chemical potential "long range correction"
c
      drcut = cutoff
      drcut2 = drcut * drcut
c
      pkt = 1.0D0
c
c     Initialize radial distribution function variables
c
      recip_bin_width = h / bin_width
      icount = 0
```

```
            entest = 0
            wtest = 0
c
      n_g_hist = recip_bin_width + 1.00001D0
c
      do i = 1, n_g_hist
       r = (i - 1) * bin_width
       bin_vol(i) = tpi * 0.5 * ((r + bin_width)**2 - r**2)  ! area
      end do
c
c
      if(itest.eq.1)goto 5
c
c     This routine sets up initial configuration in BCC lattice
c
c           write(6,*) 'x       y     '
            write(6,*) ' '
      il = 1
      xa = -0.5*h - shift
      do 4 jx = 1, in2
       xa = xa + unit
       ya = -0.5*h - shift
       do 4 jy = 1, in2
        ya = ya + unit
        ixy = jx + jy
c                       if(mod(ixy,2).ne.0)goto 4
        x(il) = xa
        y(il) = ya
        il = il + 1
c                       write(6,*) xa, ya
 4    continue
 5    continue
c
                        write(6,*) 'v1 = ',v1,'    h = ', h

c     This routine calculates the potential energy and virial
c     of the initial configuration.
c
      qpe = 0.0D0
c      qvir = 0.0D0
c
c     loop over all atoms i and m > i
c
      do 6 i = 1, (natoms - 1)
       xi = x(i)
       yi = y(i)
       do 16 m = (i + 1), natoms
        rx = xi - x(m)
        ry = yi - y(m)
c                       write(6,*) rx, ry
c
c     apply minimum image convention.
c
        rx = rx - 2.0D0 *h* (int(rx/h))
        ry = ry - 2.0D0 *h* (int(ry/h))
        rsq = rx * rx + ry * ry
        if(rsq.gt.drcut2)goto 16
```

```
      Attr = Ud*(1.d0 / rsq)**(3.d0/2.d0)
                  Rep =  (1.d0 / rsq)**100
      qpe = Rep - Attr + qpe
c                 write(6,*) qpe
 16   continue
 6    continue
c
c   This routine gives intitial output
c
     write(6,*) ' '
     write(6,*) ' (NVT) Simulation Initialization Complete'
     write(6,*) ' qpe = ',qpe
c
     write(6,*)' '
     write(6,*)' rostar = ',rost
     write(6,*) natoms,'  LJ atoms'
     write(6,*) ' reduced max displacement = ',dp
c
c         Generate Widom insertion positions (200 insertion points)
c
          do  i = 1, 1000
c
                  xtest(i) = 2 * h * (ran(iseed) - .5)
                  ytest(i) = 2 * h * (ran(iseed) - .5)
c
          enddo
c
ccccccccccccccccccccccccccccccccccccccccccccccccccccccccccccccccccccccccccccccc
ccccccccccccccccccccccccccccccccccccccccccccccccccccccccccccccccccccccccccccccc
c
c   This routine is the Monte Carlo simulation routine
c
c    Ipart is the particle which will be moved to a trial location
c
     do 10 nt = 1, nst
c
 12   ipart = ipart + 1
     if(ipart.gt.natoms)ipart=1
     pei = 0.0D0
     pt = 0.0D0
c     vi = 0.0D0
c     vt = 0.0D0
c
c    Save the present postion of particle for faster access in loops
c
     xi = x(ipart)
     yi = y(ipart)
c
c    Move particle a random distance along each axis
c
     xd = dp * (ran(iseed) - .5)
     yd = dp * (ran(iseed) - .5)
     xt = xi + xd
     yt = yi + yd
c
c
c    Apply periodic boundary conditions
```

```
c
      xt = xt - 2.0D0*h * int(xt/h)
      yt = yt - 2.0D0*h * int(yt/h)
c
c     Loop to find the present potential energy of the particle
c
      do 7 m = 1, natoms
       if(m.eq.ipart)goto 7
c
c     Get the distance between the present position and all other
c     particle postions.
c
        rx = xi - x(m)
       ry = yi - y(m)
c
c     Apply minimum image convention.
c
         rx = rx - 2.0D0 *h* (int(rx/h))
         ry = ry - 2.0D0 *h* (int(ry/h))
       rsq = rx*rx + ry*ry
c
c     PEI sums the present potential of particle IPART
c
       if(rsq.gt.drcut2)goto 8
                      Attr = Ud*(1.d0 / rsq)**(3.d0/2.d0)
                      Rep =  (1.d0 / rsq)**100
                      pei = pei + Rep - Attr
c       vi = vi + r6 - 2.0D0 * r12
c
c     Now find the distance between the test particle position and
c     all other particle positions.
c
  8    rx = xt - x(m)
       ry = yt - y(m)
c
c     Apply minimum image convention.
c
         rx = rx - 2.0D0 *h* (int(rx/h))
         ry = ry - 2.0D0 *h* (int(ry/h))
       rsq = rx*rx + ry*ry
c
c     PT sums the potential of the test particle.
c
       if(rsq.gt.drcut2)goto 7
                      Attr = Ud*(1.d0 / rsq)**(3.d0/2.d0)
                      Rep =  (1.d0 / rsq)**100
                      pt = pt + Rep - Attr
c       vt = r6 - 2.0D0 * r12 + vt
c
  7    continue
c
c     Scale the potential energy and virial to the new volume
c
c      vt = 6.0D0 * vt
c      vi = 6.0D0 * vi
c
      de = pt - pei
```

```
      ex = pkt * de
c             write(6,*) ex
c
c     Test exp(-ex) to decide whether to accept or reject the trial config
c
      if(ex.lt.0.0)goto 15
      if(exp(-ex).lt.ran(iseed))goto 9
c
c     New potential energy and virial become old potential and virial.
c
 15   qpe = qpe + pt - pei
c      qvir = qvir + vt - vi
c
c     Assign new particle position.
c
      x(ipart) = xt
      y(ipart) = yt
c
c     Increment the no. of configurations accepted (rolling avg and overall).
c
      nc = nc + 1
      nv = nv + 1
c
c     Whether the new postion was accepted or not increase the number
c     of trials tested
c
 9    continue
      ape = ape + qpe
c      pr = pr - (qvir + vlrc) * 4.0D0 / 3.0D0 / vl
c
ccccccccccccccccccccccccccccccccccccccccccccccccccccccccccccccccccccccccccccccccc
c    Widom particle insertion to calculate the Chemical Potential
c
c    If nt/ no. of steps between Widom particle insertion is an integer,
c    calculate the chemical potential.
c
           if(mod(nt,n_widom).eq.0.and.nt.gt.n_equilib) then
c
           do  i = 1,1000
c
                      x_test = xtest(i)
                      y_test = ytest(i)
c
c     Now find the distance between the test particle position and
c     all other particle positions.
c
                      entest = 0.0D0
c
                      do  m = 1 , natoms
c
                                 rx = x_test - x(m)
                                 ry = y_test - y(m)
c
c     Apply minimum image convention.
c
                                 rx = rx - 2.0D0 *h* (int(rx/h))
                                 ry = ry - 2.0D0 *h* (int(ry/h))
```

```
                        rsq = rx*rx + ry*ry
c
c    PT sums the potential of the test particle.
c
                        if(rsq.lt.drcut2) then
c
                                Attr      = Ud*(1.d0 / rsq)**(3.d0/2.d0)
                                Rep               = (1.d0 / rsq)**50
                                entest  = entest + Rep - Attr
c
                        endif
c
                end do
c
c       entest is the additional energy due to insertion
c       wtest  is the sum of all the Boltzmann factors
c
                wtest  = wtest + dexp(-pkt*entest)
c
                count_widom = count_widom + 1
c
        end do
c
        end if
c
ccccccccccccccccccccccccccccccccccccccccccccccccccccccccccccccccccccccccccccccc
c
c   If nt/ no. of steps between calculating the radial distribution
c   function is an integer, calculate the radial distribution function.
c
    if(mod(nt,n_radial).eq.0.and.nt.gt.n_equilib) then
     call radial(x, y,h, recip_bin_width, i_g_hist, natoms)
     icount = icount + 1
    end if
c
c    If nt/ no. of steps between print is integer then print averages
c    and cumulative values
c
    if(mod(nt,nbp).ne.0)goto 10
c
c       Print out the average chemical potential
ccccccccccc
c
        if(icount.ne.0) then
c
                if(wtest.gt.0) chempot = -dlog(wtest/count_widom)
c
                write(6,*) ' '
                write(6,*) 'Chemical potential =  ', chempot
                write(6,*) ' '
c
        endif
c
ccccccccccccccccccccccccccccccccccccccccccccccccccccccccccccccccccccccccccccccc
ccccc   Calculate Radial Distribution Function and Pressure    cccccccc
ccccccccccccccccccccccccccccccccccccccccccccccccccccccccccccccccccccccccccccccc
c
```

```
            ape = 1.0D0 * (ape / nbp ) / natoms
      pr = pr / nbp + natoms / vl
            pressure = rost
c
      if(icount.ne.0) then
c       write(6,*) ' '
       write(6,*) '          r/sigma                g(r) '
       do i = 1, n_g_hist/1.6
        r = (i - 1) * bin_width + 0.5D0 * bin_width
        g = float(i_g_hist(i)) / (rost * bin_vol(i) * float(natoms)
     1       * float(icount)) * 2.D0
        if(g.gt.-0.5D0) write(6,*) r, g
c
c           Calculate pressure (numerical integration)
ccccccccccccccccccccccccccccccc
                                  if (r.gt.1.02d0) then
                              pressure = pressure - (rost**2) /3 * 3*r*Ud*(1/r)**4 * g * 3.1416d0 * r * bin_width
                                  endif
ccccccccccccccccccccccccccccccccc
       end do
c       write(6,*) ' '
      end if
      ape = 0.0D0
      nv = 0
      pr = 0.0D0
c
ccccccccccccccccccccccccccccccccccccccccccccccccccccccccccccccccccccccccc
c           Print out the reduced pressure
ccccccccccccccccccccccccccccccccccccccccccccccccccccccccccccccccccccccccc
c
            if(icount.ne.0) then
c
                        write(6,*) ' '
                        write(6,*) 'pressure =  ', pressure
                        write(6,*) ' '
c
            endif
c
ccccccccccccc
c
c     If time to quit then quit
c
 10   continue


                        DO pp = 1, 256
                        write(6,*) x(pp), y(pp)
                        Enddo
c
ccccccccccccccccccccccccccccccccccccccccccccccccccccccccccccccccccccccccc
ccccccccccccccccccccccccccccccccccccccccccccccccccccccccccccccccccccccccc
c
      close(unit=6)
c
      stop
      end
```

Radial distribution function:

```
      subroutine radial(x, y, h, recip_bin_width, i_g_hist, natoms)
c
ccccccccccccccccccccccccccccccccccccccccccccccccccccccccccccccccccccccccc
c
c     This subroutine calculates Radial distribution function in 2D.
c
ccccccccccccccccccccccccccccccccccccccccccccccccccccccccccccccccccccccccc
      implicit double precision (a-h,o-z)
      Dimension x(256), y(256)
      Dimension i_g_hist(1000)
c
c     loop over all atoms i and m > i
c
      do 6 i = 1, (natoms - 1)
c
        xi = x(i)
        yi = y(i)
c
        do 16 m = (i + 1), natoms
c
          rx = xi - x(m)
          ry = yi - y(m)
c
c     apply minimum image convention.
c
          rx = rx - 2.0D0 *h* (int(rx/h))
          ry = ry - 2.0D0 *h* (int(ry/h))
          rsq = rx * rx + ry * ry
c
          if (rsq.lt.h**2) then
c
            r = sqrt(rsq)
            i_bin = int(r * recip_bin_width/h) + 1
            i_g_hist(i_bin) = i_g_hist(i_bin) + 1
c
          end if
 16     continue
 6    continue

      return
      end
```

Random number generator:

```
C
C
C     FUNCTION RAN     (ISEED)
CxxxxxFUNCTION GGUBFS  (ISEED)
C
```

```
C------------------LIBRARY 1-------------------------------------
C
C  FUNCTION         - BASIC UNIFORM (0,1) PSEUDO-RANDOM NUMBER
C                   GENERATOR
C  USAGE            - RAN(ISEED)
CxxxUSAGE           - GGUBFS(ISEED)
C  PARAMETERS   ISEED - INPUT. AN INTEGER VALUE IN THE EXCLUSIVE
C                   RANGE (1,2147483647). ISEED IS REPLACED BY
C                   A NEW ISEED TO BE USED IN SUBSEQUENT CALLS.
C  PRECISION        - DOUBLE
C  LANGUAGE         - FORTRAN
C---------------------------------------------------------------------
C  LATEST REVISION    - JANUARY 28,1974
C
CxxxxxFUNCTION GGUBFS(ISEED)
      DOUBLE PRECISION FUNCTION RAN(ISEED)
C
      DOUBLE PRECISION  Z,D2P31M,D2PN31
C                       D2P31M = (2**31) - 1
C                       D2PN31 = 1 / (2**31)
      DATA D2P31M/2147483647.D0/,D2PN31/0.46566128730773925 8D-9/
      Z = DBLE(ISEED)
      Z = DMOD(16807.D0*Z,D2P31M)
C     GGUBFS = Z * D2PN31
      RAN    = Z * D2PN31
      ISEED = IDINT(Z)
      RETURN
      END
```

Input parameter:

256	# of spheres
6.0	Reduced pair potential depth (kT)
2	1 if running from an old configuration or 2 if from a lattice
0.92	Density of the fluid reduced with D^2 (D is the diameter of beads)
10500000	# of steps in the simulation
0.04	Maximum displacement _ Step length in units of atom diameter D
500000	# of steps between printing averages
100	# of steps between performing Widom particle insertion
100	# of steps between calculating the radial histogram
0.04	Bin width for the radial distribution histogram
10000000	# of equilibration steps (radial hist. is calc. only after equil.)

Appendix E

MATLAB code for Radial Distribution Function and Bond-orientation correlation function calculation

Radial Distribution Function:

```
clc
clear

d = 10.7;  % average diameter of a 1 um bead in PIXELS
j=1; % index
P = []; % position matrix that stores all beads' positions in all frames
for a = 1 : 3000

      str = strcat('"F:\1.21\1hr 0.375%\N',int2str(a),'.tif"');
      eval(['F = imread(' str ');']);
      Fd = double(F(:,:,1));
%       Fd(220:400,275:end) = 50;       %this is to screen out a random particle not part of the chain of
interest

      % Choosing the Region of Interest
      %FF = Fd(150:350,40:200);
      %imagesc (real(fftshift(fft2(Fd)))); caxis([0 1e6]);axis([500 900 350 680]);
      FF = Fd;
      b  = bpass(FF,3,40);          % 40 for 2.8 um, 8 for 1 um
      bb = mat2gray(b);
      pk = pkfnd(bb,0.5,20);         % 20 for 2.8 um, 7 for 1 um
      cnt = cntrd(bb,pk,27,0);       % 27 for 2.8 um, 9 for 1 um
      %P(:,:,j) = cnt';


dr = 0.1;         % Step size in unit of microns
X  = 5;           % Range of g(r) in particle diameter
D  = 3.1;         % D is the diameter of a sphere in microns
d  = 10.7;        % Pixel to micron ratio
r  = D:dr:X*D;     % Distance variable
%---------------------------------------
% Functions ------
g  = zeros(1,length(r));   % Positional pair correlation function
g6 = [];                % Directional pair correlation function
```

```
M  = length(cnt);          % Total number of spheres
%-------------------------------------
i = 1;  % Reference sphere number
n = 0;  % Reference sphere count
while i<=M
   % Defining the ROI of reference spheres
   while cnt(i,1)>50+10.8*D*d & cnt(i,2)>50+10.8*D*d & cnt(i,1)<1392-(50+10.8*D*d) &
cnt(i,2)<1040-(50+10.8*D*d)
      N = 1; % N is the number of spheres withn a certain range (minus itself)
      j = 1; % Comparing sphere number
      while j <= M
         while cnt(i,1)-cnt(j,1) <= (10*D+dr)*d
            % Distance between ith and jth sphere
            R = sqrt( (cnt(i,1)-cnt(j,1))^2 + (cnt(i,2)-cnt(j,2))^2 )/d;
            if R <= X*D & R~=0  % Excluding itself
               % Obtaining all the distances within the 10D circle
               Rx(N) = R;
               N = N + 1;
            end
            if cnt(j,1)-cnt(i,1) > (10*D+dr)*d
               break;
            end
            j = j + 1;
         end
         j = j + 1;
      end
      g_Now = hist(Rx,r)./r;    % Histogram of Rx using r bin-series
      g  = g + g_Now;        % Adding to the total g(r)
      Rx = [];               % Clear Rx vector
      i  = i + 1;            % Moving to the next reference sphere
      n  = n + 1;            % Adding to the total reference sphere count
   end

   i=i+1;
end

QQ(a,:)=g;

plot(r,g,'o-');
      j = j+1
      a
end
```

Bond-orientation correlation function:

```
clear
clc
F=imread('E:\Research\Projects\Porject # 14 2D Field-induced Colloidal Crystal\1.19\New
Folder\1_3hrs.tif');

Fd = double(F(:,:,1));
```

```
FF = Fd;
b  = bpass(FF,3,40);          % 40 for 2.8 um, 8 for 1 um
bb = mat2gray(b);
pk = pkfnd(bb,0.5,20);        % 20 for 2.8 um, 7 for 1 um
cnt = cntrd(bb,pk,27,0);      % 27 for 2.8 um, 9 for 1 um
%
% Pair Correlation Function (Position and Orientation)
%
%%%
```

```
        II = I(2:7); % Getting rid of the 1st trivial self (reference)
        for jj = 1:6
           theta = atan( (cnt(II(jj),2)-cnt(i,2)) / (cnt(II(jj),1)-cnt(i,1)) );
           if (cnt(II(jj),2)-cnt(i,2))/d > 0 & (cnt(II(jj),1)-cnt(i,1))/d < 0
              theta = theta + pi;
           elseif (cnt(II(jj),2)-cnt(i,2))/d < 0 & (cnt(II(jj),1)-cnt(i,1))/d < 0
              theta = theta + pi;
           elseif (cnt(II(jj),2)-cnt(i,2))/d < 0 & (cnt(II(jj),1)-cnt(i,1))/d > 0
              theta = theta + 2*pi;
           end
           Angle_Ref(jj) = theta;
        end
        % Aligning the angles in ascending order
        % !!!!!!!!!!! THIS is to compute the CONGUGATE of the psi
        psi_ref = sum(exp(-6i*Angle_Ref))/6;
        % END of Reference particle
        %-------------------------------------------------------------
        % Start of comparing particles
        %
        j = 1; % Comparing sphere number
        while j <= M
           while j <= M & (cnt(i,1)-cnt(j,1) <= (10*D+dr)*d)
              % Distance between ith and jth sphere
              R = sqrt( (cnt(i,1)-cnt(j,1))^2 + (cnt(i,2)-cnt(j,2))^2 )/d;
              if R > r & R <= r+dr  % Distance within the [r r+dr] range
                 % Perform local bond-angle calculation for comparing sphere
                 for ii = 1:M
                    RR(ii) = sqrt( (cnt(j,1)-cnt(ii,1))^2 + (cnt(j,2)-cnt(ii,2))^2 )/d;
                 end
                 % Sort RR in a ascending manner to find 6 nearest neighbours
                 [Y, I] = sort(RR);
                 II = I(2:7); % Getting rid of the 1st trivial self (reference)
                 for jj = 1:6
                    theta = atan( (cnt(II(jj),2)-cnt(j,2)) / (cnt(II(jj),1)-cnt(j,1)) );
                    if (cnt(II(jj),2)-cnt(j,2))/d > 0 & (cnt(II(jj),1)-cnt(j,1))/d < 0
                       theta = theta + pi;
                    elseif (cnt(II(jj),2)-cnt(j,2))/d < 0 & (cnt(II(jj),1)-cnt(j,1))/d < 0
                       theta = theta + pi;
                    elseif (cnt(II(jj),2)-cnt(j,2))/d < 0 & (cnt(II(jj),1)-cnt(j,1))/d > 0
                       theta = theta + 2*pi;
                    end
                    Angle_Comp(jj) = theta;
                 end
                 % Aligning the angles in ascending order
                 psi_comp = sum(exp(6i*Angle_Comp))/6;
                 %-------------------------------------------------
                 % Calculate bond-orientation correlation
                 g6_Now = g6_Now + abs(psi_ref * psi_comp);
                 % Start counting the particles within the [r r+dr] range
                 N = N + 1;
        %       elseif R <= r | R > r+dr
        %          break;
              end
              j = j + 1;   % Moving to the next comparing sphere
```

```
            end
            j = j + 1;   % Moving to the next comparing sphere
        end
        i = i + 1;       % Moving to the next reference sphere
    end
    i = i + 1;   % Moving to the next reference sphere
end
% Computing g6(r)
if N ~= 0
    g6(k) = g6_Now/N;
elseif N == 0
    g6(k) = 0;
end
g(k) = N;
k = k + 1;    % Distance r index
N = 0;        % Pair count returns to zero

end

r = D:dr:X*D;     % Distance variable

%figure;
plot(r,(g6)); hold on
```